LINKING SURFACE EVOLUTION WITH MANTLE DYNAMIC PROCESSES USING ADJOINT MODELS WITH DATA ASSIMILATION

Thesis by

Lijun Liu

In Partial Fulfillment of the Requirements

for the degree of

Doctor of Philosophy

California Institute of Technology

Pasadena, California

2010

(Defended May 25, 2010)

ACKNOWLEDGEMENTS

First, I want to express my sincere gratitude to my advisor, Professor Michael Gurnis, for his patient guidance during the past five years. I thank Mike for his warm encouragement when I get frustrated on research, his careful and thorough suggestions on my scientific writing, and his incisive visions and prudent cautions on my thesis work. I cherish the days that I have learned so much from Mike and the convenience he provides for me to work on exciting projects using world-class computing facilities. I am grateful for all his help and all the rewarding collaborations we have developed.

I would like to thank several knowledgeable faculty members from whom I've learned a lot. Especially, I want to thank Professor Don Helmberger for all his kind help and stimulating discussions with me, which almost makes me a seismologist. I also want to thank Professors Joann Stock, Jennifer Jackson and Jason Saleeby for their generous help with my research. A special thanks goes to my academic advisor, Nadia Lapusta, who helped me a lot during the trying times. I also want to thank Hiroo Kanamori and Don Anderson, for their warm-hearted directions on spontaneous questions I came up with. I very much enjoy the academic atmosphere at the Seismological Laboratory. Meanwhile, I am also very thankful to our friendly and helpful Seismo Lab staff; without you these years would have been much more boring.

My thanks also go to the current and previous graduate students in the Seismo Lab. I'm grateful to Dr. Eh Tan and Dr. Eunseo Choi, who assisted me through the initial stage of geodynamic research with their experience and knowledge. I thank Dr. Ying Tan and Dr. Daoyuan Sun, who helped me extensively for seismological research. I also thank my fellow graduate students Sonja Spasojevic for earlier collaborations, and Dan Bower for carrying on interesting discussions. I have really enjoyed the times chatting and socializing with Shengji, Zhongwen, Dongzhou, and many other students, and I thank you all for your friendship.

Finally, my sincere thanks go to my beloved wife, Yun, and our families back in China. First, I am deeply thankful to my parents for raising me up and sending me to college,

which had been a big burden for a family with little income like mine. I want to sincerely thank my wife for her caring for me during the past years, which makes my life and work a lot easier. I am so lucky to have you with me while staying so far away from our families. I also want to express my thanks to my parents in law for their understanding and encouragement. Without all your enduring and absolute support, I would have accomplished nothing.

ABSTRACT

Quantifying the relationship between subsolidus mantle convection and surface evolution is a fundamental goal of geophysics. Toward this goal progress has been slow due to incomplete knowledge of the earth's internal structure and properties. While seismic tomography reveals details on internal 3D structure of the present mantle, evolution of the subsolidus mantle during the geological past remains elusive. This thesis attempts to solve the time inversion of mantle convection using the adjoint method based on present-day seismic images and geological and geophysical observations dictating the past evolution of solid earth.

The adjoint method, widely used in meteorological and oceanographic predictions, can be applied to mantle convection for the recovery of unknown initial conditions through the assimilation of present-day mantle seismic structure. We propose that an optimal first guess to the initial condition can be obtained through a simple backward integration (SBI) of the governing equations thus lessening the computational expense. By incorporating time-dependent surface dynamic topography in addition to present-day mantle structure, the adjoint method is improved so as to constrain uncertain mantle dynamic properties and initial condition simultaneously. The theory is derived from the governing equations of mantle convection and validated by synthetic experiments for a single- and two-layer viscosity mantle within regionally bounded spherical shells. For both cases, we show that the theory can constrain mantle properties with errors arising through the adjoint recovery of the initial condition. For the two-layer model, there is a trade-off between the temperature scaling and lower mantle viscosity.

By assimilating seismic structure and plate motions in the inverse mantle convection model, we reconstruct Farallon plate subduction back to 100 Ma. We put constraints on basic mantle properties, including both the depth dependence of mantle viscosity and slab buoyancy, by predicting proxies of dynamic topography evident in the stratigraphy of the North American Cretaceous western interior seaway. Models that fit stratigraphy well require the Farallon slab to have been flat lying in the Late Cretaceous, consistent with

geological reconstructions. The models predict an extensive zone of shallow-dipping subduction extending beyond the flat-lying slab farther east and north, while the limited region of subducting flat slab resembles an oceanic plateau. In order to test the hypothesis of oceanic plateau subduction and its relationship to the Laramide orogeny, we compare the inverse convection model with plate reconstructions. Two prominent seismic anomalies on the Farallon plate recovered from inverse models coincide with paleogeographically-restored positions of conjugates to the Shatsky and Hess plateaus when they subducted beneath North America. The distributed shortening of the Laramide orogeny closely tracked the passage of the Shatsky conjugate beneath North America, while the effects of Hess conjugate subduction were restricted to the northern Mexico foreland belt. We find that Laramide uplifts were consequences of the removal, rather than the emplacement, of the Shatsky conjugate, and we predict that these subducted plateaus should be detectable by the USArray seismic experiment.

The inverse convection models predict a continuous vertical motion history of western U.S., which is further validated by constraints on the vertical motion of the Colorado Plateau since the Cretaceous. With the arrival of the flat-lying Farallon slab, dynamic subsidence swept from west to east over the western U.S., peaking at 86 Ma within the Colorado Plateau. This eastward migrating dynamic subsidence is consistent with a recently compiled backstripping study that shows a long-wavelength residual subsidence shifting to the east, coincident with the passage of the flat slab beneath North America in our inverse model. Two stages of uplift followed the removal of the Farallon slab below the Colorado Plateau: one in the latest Cretaceous, and the other in the Eocene, with a cumulative uplift of ~1.2 km; the former represents the Laramide uplift which also marks the initial uplift of the entire western U.S. Both the descent of the slab and buoyant upwellings raised the Colorado Plateau to its current elevation during the Oligocene. A locally thick lithosphere enhances coupling to the upper mantle so that the Colorado Plateau has a higher topography with sharp edges. Our models also predict that the plateau tilted downward to the northeast before the Oligocene, caused by northeast-trending subduction of the Farallon slab, and that this northeast tilting diminished and reversed to the southwest during the Miocene in response to buoyant upwellings.

Overall, this thesis shows that the adjoint models with data assimilation are useful in linking surface evolution to deep mantle processes both over North America and areas beyond. While more research is clearly needed to construct a more earth-like model, this thesis presents an important advance in data-oriented geodynamic models.

CONTENTS

LIST OF FIGURES

LIST OF TABLES

Chapter 1
Introduction

One of the ultimate goals of geophysics is to understand subsolidus mantle convection and its relationship with surface observables, both geophysical and geological. Steady progress has been made as we increase our ability to image the earth's internal structures. Development of seismic tomography has provided significant insights into mantle convection. From global seismic tomography, we see not only large-scale low-velocity anomalies rising from the CMB and high-velocity belts correlated with ancient subduction zones [*Su et al.*, 1994; Li and Romanowicz, 1996; Masters *et al*., 2000], but also structures like subducted oceanic slabs extending into the lower mantle [Grand *et al*., 1997; Van der Hilst *et al*., 1997; Ritsema *et al*., 2004; Li *et al*., 2008]. Deep-rooted columnar low seismic velocity structures, associated with surface hot spots, may have been detected and could be indicative of active mantle plumes [Montelli *et al*., 2004, Zhao, 2004; Nolet et al., 2007]. Closer to the surface, regional tomography has imaged active subduction zones showing high seismic velocity slabs overlain by low velocity mantle wedges [Zhao *et al*., 1997; Huang and Zhao, 2006; Sigloch *et al*., 2008; Roth *et al*., 2008]. Although very informative, tomographic images only provide a snapshot of mantle convection, the final instant of an evolving system.

In order to constrain the time dependence of mantle convection, other geophysical observations beyond seismic imaging and gravity that extend into the time domain are needed. An important constraint comes from the velocity of plates and their time dependence that can be predicted in global flow models [Lithgow-Bertelloni and Richards,

1998]. Another possibility comes from surface topography (through stratigraphy and relative sea level) that has been used as a constraint on time-dependent models of mantle convection [Gurnis, 1993; DiCaprio *et al.*, 2009], some with assimilated plate motions [Gurnis *et al.*, 1998]. Furthermore, predicting the present-day mantle seismic structures through forward models also helps to constrain past geologic events [Bunge and Grand, 2000] and explain uncertain mantle anomalies [McNamara and Zhong, 2005].

However, previous models of mantle convection have all faced the difficulty of incorporating reasonable initial conditions. For example, Bunge *et al*. [1998] assumed a quasi steady-state mantle structure achieved by imposing the Cretaceous plate motion for a relatively long time before allowing time-dependent plate kinematics to start. This assumption is potentially problematic since plate motions change continuously. Gurnis *et al*. [1998] used an initial condition at 140 Ma in a model of the Australian region based on the earlier geological evolution. These initial conditions cannot reproduce the exact structures of present-day mantle.

On the other hand, Steinberger and O'Connell [2000] and Conrad and Gurnis [2003] utilized a simple backward integration of the convection equations to predict past mantle structure by advecting the current mantle structures back in time, while neglecting thermal diffusion. This method, however, limits its application, because neglecting thermal diffusion will lead to the accumulation of artifacts at thermal boundaries with time [Ismail-Zadeh *et al.*, 2004]. Inferring the initial condition of a diffusive process through a simple reversal of time is problematic because it leads to exponentially growing numerical errors, which is called an ill-posed problem.

A promising approach to recovering initial conditions is through the use of an adjoint method widely adopted in meteorology and oceanography [Talagrand and Courtier, 1987] and recently introduced into mantle convection [Bunge *et al*. 2003; Ismail-Zadeh *et al*., 2004]. The method constrains the initial condition by minimizing the mismatch of a prediction to observation iteratively in a least-square sense. Through synthetic experiments, Bunge *et al*. [2003] and Ismail-Zadeh *et al.* [2004] separately demonstrated that the initial condition could be effectively recovered with iterative solver schemes. However, the application to geophysical problems remained limited, because earlier tests all assumed that the initial condition is the only unknown in the system, which is obviously not true. In fact, both the rheology and effective Rayleigh number of the mantle, two key parameters governing the vigor of convection, are still uncertain, and this prohibits a unique recovery of the past mantle structure since the solution strongly depends on these mantle properties. On the other hand, the computational expense of earlier adjoint algorithms is high, especially for large- 3D models.

In this thesis, I will summarize our work on improving the adjoint method by expanding the category of data constraints for assimilation and applying the method with real data. In Chapter 2, we describe the theoretical basis of the adjoint method in mantle convection and its implementation in computational software. By bringing in time-dependent observations, i.e., surface dynamic topography, the adjoint method can be used to constrain uncertain mantle dynamic properties, while simultaneously recovering the unknown initial conditions of mantle, as we show in Chapter 3. While in Chapter 4, with the improved adjoint inversion technique, we perform the first inversions of mantle convection

based on data (including seismic tomography, plate motions, and stratigraphy as proxy for dynamic topography). The model was tailored for recovering the Farallon plate subduction back to the Late Cretaceous. In Chapter 5, by combining the adjoint models with plate reconstructions and structural features, we argue that the mechanism causing flattening of the Farallon slab was subduction of two oceanic plateaus, whose passage beneath North America had led the formation of the enigmatic Laramide orogenic event. This chapter also discusses the vertical motion evolution of the western and eastern U.S. accompanying the Farallon subduction, and implication of the inverse model on quantifying evolution of the western interior basins. In Chapter 6, I first provide a broader discussion on subduction evolution during the past beyond North America based on the adjoint model we have developed, followed by a summary of limitations of the current inverse models and some possible future improvements.

Chapter 2

Adjoint Method in Mantle Convection[1]

2.1 Theoretical Basis of the Adjoint Method

The adjoint method for data assimilation is a gradient-based inversion, which is particularly useful for inverting nonlinear dynamic systems. Derivation of the adjoint method for an evolving system is based on perturbation theory, where a mismatch in the model output against observation is attributed to an error in the model input, with their relation approximated as a first order derivative (gradient) of the least-squared mismatch with respect to the input. To formulate the concept mathematically, consider an initial value problem in which all the governing equations and boundary conditions are perfectly known and numerical errors are negligible. Any mismatch in the prediction should be attributed to errors in the initial condition (i.e., model input). This relation can be simply expressed as $dJ = (\partial J / \partial \vec{a}) d\vec{a}$, where J is a scalar cost function, which defines the mismatch of prediction from data and $\vec{a}$ is the initial variable that potentially carries error. If an explicit form of the expression $\partial J / \partial \vec{a}$ can be obtained, then the perturbation (i.e., error) $d\vec{a}$ associated with the initial condition can be retrieved.

---

[1] This chapter is based on: 1) Liu L. and M. Gurnis (2008), *Simultaneous Inversion of Mantle Properties and Initial Conditions Using an Adjoint of Mantle Convection*, J. of Geophy. Res., 113, B08405, doi:10.1029/2008JB005594. 2) Liu, L. and M. Gurnis (2010), *Adjoint method and its application in mantle convection*, Earth Science Frontiers (Chinese with English abstract), in press.

Specifically, we define the cost function J as a function of temperature T

$$J = \iint_{t,V} (T_p - T_d)^2 \, dvdt \tag{1}$$

where T_p is the predicted temperature, T_d is the actual temperature (with the subscript d denoting data), t is time, and V is volume. In mantle convection, T_d is available only at the present day t_1, so effectively J is a delta function in the time domain with a nonzero value at t_1.

The governing equations for mantle convection, assuming an incompressible and Newtonian fluid, are

$$\nabla \cdot \vec{u} = 0 \tag{2}$$

$$\nabla P + \nabla \cdot (\eta \nabla \vec{u}) = \rho_m \alpha \Delta T \vec{g} \tag{3}$$

$$\frac{\partial T}{\partial t} + \vec{u} \cdot \nabla T = \kappa \nabla^2 T \tag{4}$$

where $\vec{u}$ is velocity, P dynamic pressure, η dynamic viscosity, ρ_m ambient mantle density, α coefficient of thermal expansion, ΔT temperature anomaly, $\vec{g}$ gravitational acceleration, T temperature, and κ thermal diffusivity.

If we assume $T(t_0)$ is the only variable that brings error into our prediction, our goal, in order to retrieve this quantity, is to obtain the expression $\partial J / \partial T(t_0)$, where t_0 refers to the initial time. This expression can be obtained through a constraint condition of the energy equation by introducing the adjoint variable λ (a Lagrangian multiplier) that forms a Lagrangian function L

$$L = J + \iint_{t,V} \lambda (\frac{\partial T}{\partial t} + \vec{u} \cdot \nabla T - \kappa \nabla^2 T) dvdt \tag{5}$$

A perturbation in L corresponds to perturbations in J and T. Subsequently, we will use δ to denote the perturbed quantities.

$$\delta L = \delta J + \iint_{t,V} \lambda(\frac{\partial \delta T}{\partial t} + \vec{u} \cdot \nabla \delta T - \kappa \nabla^2 \delta T) dv dt \qquad (5')$$

In principle, the velocity u should also contribute to this perturbation since it depends on T (see Eq. 3 and Bunge *et al*. [2003]), but we choose to neglect the velocity dependence in Eq. (5'). This is because, first, a full differentiation of Eq. (5) leads to a coupled system of the adjoint and forward models that is numerically changing to implement [Bunge *et al*., 2003]; second, inaccuracy from omission of the u dependence in Eq. (5') is diminished by the variational approach to the single temperature-adjoint solution through iterative schemes we will describe. By applying integration by parts over time and space to Eq. (5') with prescribed boundary conditions, we obtain

$$\delta L = \delta J + \int_V (\lambda \delta T) dv \Big|_{t_0}^{t_1} - \iint_{t,V} \delta T(\frac{\partial \lambda}{\partial t} + \vec{u} \cdot \nabla \lambda + \kappa \nabla^2 \lambda) dv dt \qquad (5'')$$

When $\delta L \to 0$, all terms associated with δT should vanish (λ is nonzero only at t_0 and t_1). Therefore, for any instant of time between t_0 and t_1, we have

$$\frac{\delta J}{\delta T} = \iint_{t,V} (\frac{\partial \lambda}{\partial t} + \vec{u} \cdot \nabla \lambda + \kappa \nabla^2 \lambda) dv dt \qquad (6)$$

This is called the adjoint equation or adjoint operator.

In practice, $\delta J / \delta T$ is nonzero only at the final time (t_1) in a mantle convection model when the mismatch between prediction and data is made. In effect, the term $\delta J / \delta T$ represents the residual temperature field at the final time. Therefore, the adjoint energy

equation (Eq. 6) is the same as the forward energy equation (Eq. 4) except for the diffusion term that has an opposite sign. This difference also means Eq. (6) is numerically unstable in describing a forward-time evolution, but ideal for representing a backward-time process. If we consider *t* as always being forward in time while substituting Eq. (1), then the differential form of Eq. (6) becomes

$$\frac{\partial \lambda}{\partial(-t)} - \vec{u}\cdot\nabla\lambda - \kappa\nabla^2\lambda - 2(T_p - T_d)_{t_1} = 0 \qquad (6')$$

where $2(T_p - T_d)_{t_1}$ is a forcing term at t_1. So, with $T_p - T_d$ describing the residual field at the final instant of time (which also provides a state for the system to start with), Eq. (6') represents a backward-in-time advection-diffusion process.

It can be seen that with Eq. (6), Eq. (5") can be reduced to

$$\delta L = \int_V (\lambda \delta T) dv \Big|_{t_0}^{t_1} \qquad (7)$$

Alternatively,

$$\frac{\partial L}{\partial T(t_0)} = -\int_V \lambda(t_0) dv \qquad (7')$$

Eq. (7') indicates that the gradient of the Lagrangian function *L* with respect to the initial temperature can be explicitly expressed as the adjoint quantity at the initial time. Since the Lagrantian function is an augmented (constrained) cost function, as can be seen from Eq. (5) where the zero valued constraint (Eq. 4) is prescribed at both t_0 and t_1, we can conclude that the same gradient relation as shown in Eq. (7') also holds for the cost function *J*.

$$\frac{\partial J}{\partial T(t_0)} = -\int_V \lambda(t_0) dv \qquad (7'')$$

This equation eventually allows for the following numerical algorithm to be reached.

For more references, this adjoint of the energy equation has been derived for meteorological [Sun *et al.*, 1991; Sirkes and Tziperman, 1997] and mantle convection problems [Bunge *et al.*, 2003; Ismail-Zadeh *et al.*, 2004].

In order to reverse a nonlinear process like mantle convection, iterative solvers are inevitable. We interleaved the backward adjoint calculation with a forward solution of the energy and momentum equations within an iterative procedure similar to that proposed by Bunge *et al.* [2003].

Our convention for subscript refers to time (0 for initial; 1 for present) while those for superscripts refer to the number of iterations. The number of iterations is determined by the accuracy to which we desire our prediction to satisfy data. Specifically these are described in the steps followed:

(i) Solve the forward problem with all three governing equations (Eq. 2 to 4) with initial condition T_0^n ($0 \le n \le N$, where *n* is the iteration number) and predict T_1^n . The first initial condition T_0^0 is potentially arbitrary. Store the velocity field for all time steps.

(ii) Compute the mismatch J^n and its gradient $\partial J^n / \partial T_1^n$; solve the adjoint energy equation (Eq. 7) with the velocity stored in (i) from t_1 to t_0 and obtain λ_0^n .

(iii) Update the initial field: $T_0^{n+1} = T_0^n - \alpha(n) \cdot \lambda_0^n$, where $\alpha(n)$ is a damping factor (defined as in Ismail-Zadeh *et al*. [2004] except that we took a simple form assuming $\alpha(n)$ only depends on *n*), with n_0 an adjustable integer

$$\alpha(n) = 1/(n + n_0) \tag{8}$$

In general, the coefficient α can also be a constant with values no more than 0.5, in order to reduce overshoots.

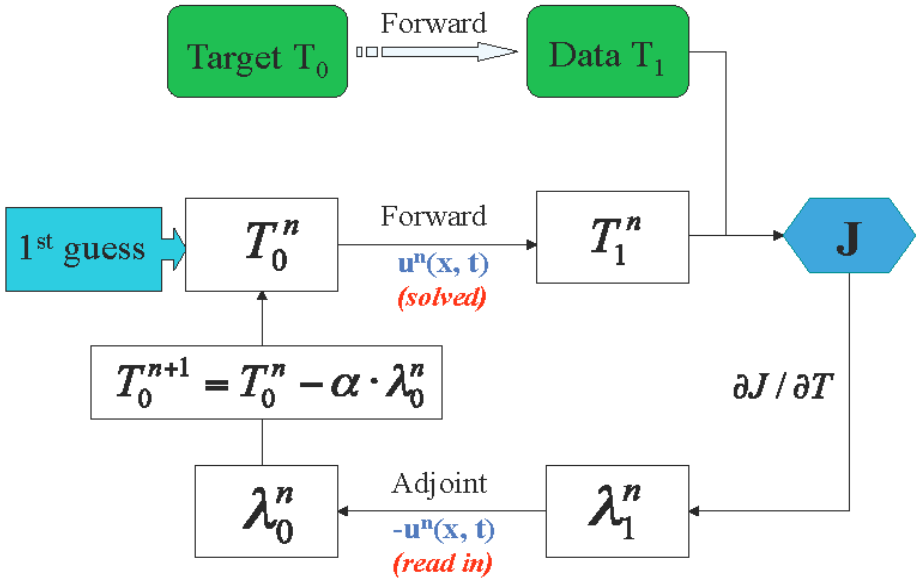

Figure 1 Illustration of the forward- adjoint iterative solver. T_0 and T_1 represent the reference initial and final states, respectively. u^n is velocity for the ^{n}th iteration, which is solved during the forward run and read in from storage during the adjoint run.

Figure 1 illustrates the whole workflow of this iterative solver for a synthetic test. We assume that the true mantle temperature in both the past and present are known, which we call reference states. This past mantle state is the solution (target) we seek by applying

the adjoint method, and the present state is the function we try to match with the forward predictions. The reference states are generated by a forward run that solves the normal convection equations (Eqs. 2, 3, 4). The forward and adjoint iterations follow the procedures described above. Iterations stop upon convergence or when the mismatch is small enough.

2.2 Numerical Implementation of the Adjoint Method

2.2.1 Solving 1D Linear Problems

Before we apply the adjoint method to more complex problems, we first design a very simple example: to invert a 1D kinematic thermal-diffusion problem, through which we illustrate the workings of the adjoint method. This simulation is carried out with a code based on the finite-element method (FEM) written in the programming language Matlab.

Imagine the reference initial condition is a thermal upwelling, e.g., a mantle plume, situated in the lower mantle sometime in the geological past (Fig. 2A), which is also the target solution we seek by inverting the present-day "observed" structure of this upwelling. For simplicity, only the forward energy equation (Eq. 4) and its adjoint operator (Eq. 7) are solved, with a prescribed velocity field. Without having to solve the advection term in Eq. (4), this is essentially a linear problem.

As Fig. 2B illustrates, the first guess of the initial condition has little correlation with the reference, so does the first prediction. This creates the largest mismatch between prediction and observation (i.e., residual temperature) among all iterations (Fig. 2B and C). The first correction to the initial condition, generated by advecting this large residual back to the initial time, is also the largest among all iterations. The initial condition, after five updates, becomes much closer to the reference while the mismatch decreases. After 15 iterations, the solution and target converge with a small mismatch. The convergence process is also reflected through a global root-mean-squared (RMS) residual (Fig. 2 C) for the initial and final states that decay exponentially with iterations.

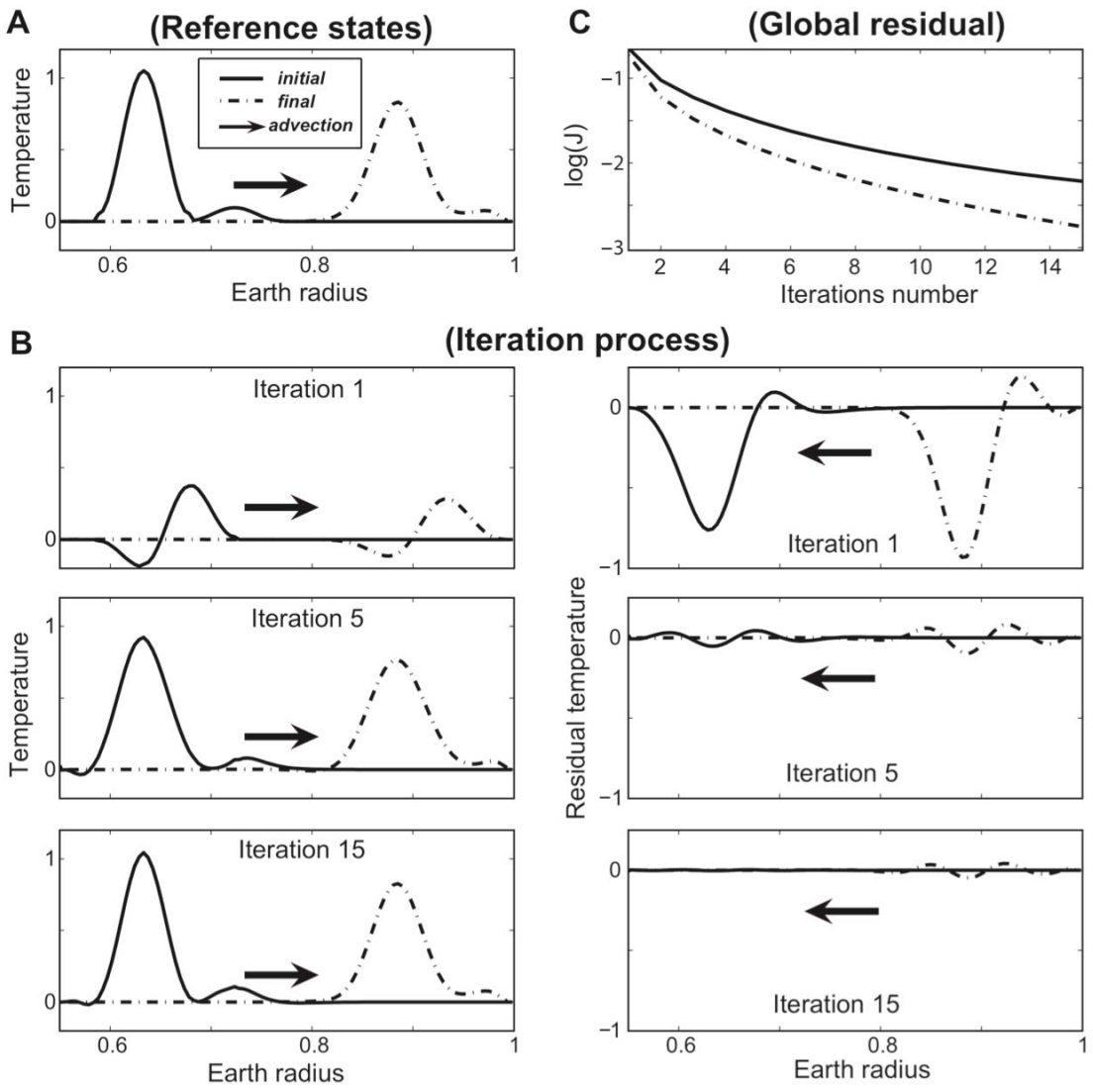

Figure 2 Adjoint inversion of a 1D linear advection-diffusion process. A. Reference initial (solid) and final (dashed) states, the bold arrow indicates the direction of the prescribed velocity. Both axes are dimensionless. B. The iterative procedure solving the initial condition. Left column shows the forward runs, while the right shows the adjoint runs. Three different iterations are shown. C. Global root-mean-squared residuals from both the initial and final states, as a function of iterations. Note the vertical axis is on a log scale.

Additional tests with different first guesses show that the solution is independent of prior information about the true initial condition. This indicates the adjoint method convergences to the true solution unconditionally for this linear inverse problem, consistent with inversion theory [Tarantola, 2005].

2.2.2 Solving 3D Nonlinear Problems

For spherical problems, we have implemented the adjoint algorithm into software using the finite element and designed specifically for mantle convection, *CitcomS* [Zhong *et al*., 2000; Tan, *et al*., 2006]. The version of *CitcomS* used here solves the equations within a spherical geometry and scales well on large parallel computers. Our changes were made to *CitcomS* version 2.1.0 obtained from the Computational Infrastructure for Geodynamics (https://geodynamics.org).

Upon implementation of the adjoint method within *CitcomS*, we hope to obtain a good solution to the initial condition while reducing the computational cost as well. Two sets of numerical experiments are designed that used the forward-adjoint looping to estimate initial conditions. The first set has a uniform viscosity (η=1), a constant ambient mantle temperature, and a Rayleigh number of 1.0×10^8. The second set of experiments has a layered viscosity, a top thermal boundary layer, and a higher Rayleigh number.

The model domain is: colatitude $\theta \in [1.27, 1.87]$, longitude $\varphi \in [0.0, 0.6]$ (both in radians), and radius (normalized by outer radius of the earth) $r \in [0.55, 1]$. Boundary conditions for the forward model are: $\vec{n} \cdot \vec{u} = 0$ and $\vec{n} \cdot \nabla \vec{u}_{tg} = 0$ on all boundaries, where $\vec{n}$

is the outer normal vector, $\vec{u}$ the velocity vector, and $\vec{u}_{tg}$ the tangential velocity; the surface and core-mantle boundary (CMB) are isothermal, while the sidewalls have zero heat flux, $\vec{n} \cdot \nabla T = 0$. The adjoint model has zero adjoint temperature on the surface and CMB, and zero adjoint heat flux on the sidewalls. The Rayleigh number is

$$Ra = \frac{\rho_m g \alpha R_o^3 \Delta T}{\eta_o \kappa} \tag{9}$$

where ΔT is the temperature drop from CMB to surface. Time is non-dimensionalized, with the actual time t related to the model time t' by

$$t = t' R_o^2 / \kappa \tag{10}$$

All symbols with their dimensional values are listed in Table 1. Hereafter, all physical quantities are normalized with their dimensional values, if not noted separately.

2.2.2.1. Models within a single layer

In the first set (Set I) of experiments, the reference states include an initial condition (Fig. 3A) that has a spherical hot anomaly in the lower part of mantle (with a maximum temperature increase of ΔT = 0.3 at the center and a Gaussian temperature profile across the center). The final condition was produced by running the model forward for 9 Myr (Fig. 3B). These two reference states are the targets we attempted to predict with the adjoint method. All models are computed on a 33×33×33 grid. We assumed n_0 = 1 in Eq. (8), for the forward-adjoint looping.

Table 1: Summary of Model Parameters

Parameter	Symbol	Value
Radius of the earth	R_o	6371 km
Gravitational acceleration	g	9.81 $m\ s$
Reference mantle density	ρ_m	3300 $kg\ m^{-3}$
Reference viscosity	η_o	10^{21} Pas
Coefficient of thermal expansion	κ	$10^{-6}\ m^2\ s^{-1}$
Thermal expansity	α	3x10
Super-adiabatic temperature drop from CMB to surface	ΔT	393˚C (Set I); 1965˚C (Set II)

All iterations were started with different first guesses to the target initial condition (each of these guesses constituted different cases, A1–A6, with "A" denoting adjoint method). Either we assumed a uniform temperature, a temperature that was a function of the actual initial condition, or generated an estimate through a simple backward integration of the governing equations (hereafter, we refer to this state of the system the SBI). The SBI was obtained by integrating the governing equations from t_1 to t_0 while reversing the sign of gravity from the forward calculation. The initial guesses were arranged in order of how close they are to the target initial condition (Table 2). Specifically, Case A1 had a nearly isothermal condition with a tiny perturbation. Case A2 had an anomaly with the same center as the target, but with a smaller volume (1/8×) and hence buoyancy. Cases A3 had the same shape and buoyancy compared to the target, but the center was shifted upward by 500 km.

Case A4 also had the same shape and buoyancy as the target but its center was shifted horizontally by 400 km. Case A5 had the same center but the anomaly had a larger volume (2.4×) and hence buoyancy. Case A6 used the SBI first guess to obtain the first guess.

Table 2: Description of the thermal anomaly structures in the reference initial state and various first guesses

	Geometry	**Center** (θ, φ, r)	**Diameter**[¶] (Dimensionless)	**Magnitude** (ΔT)
Reference	Sphere	(1.57, 0.3, 0.7)	0.3	0.3
Case A1	Sphere	(1.57, 0.3, 0.7)	0.3	0.001
Case A2	Sphere	(1.57, 0.3, 0.7)	0.15	0.5
Case A3	Sphere	(1.57, 0.3, 0.78)	0.3	0.3
Case A4	Sphere	(1.57, 0.39, 0.7)	0.3	0.3
Case A5	Sphere	(1.57, 0.3, 0.7)	0.4	0.3
Case A6	SBI[§]	--	--	--

Note: SBI[§] means simple backward integration, i.e., reverse the sign of gravity and run the forward model from the present-day mantle structure for the same amount of time.

[¶]: Diameter of the spherical anomaly, normalized by R_o, radius of the earth.

For comparison, we ran all cases for 50 iterations while tracking the recovered initial conditions. These retrieved initial conditions were noticeably different, and the recoveries in

Case A4 to A6 (Fig. 3F–H) were better than those in A1 to A3 (Fig. 3C–E). Case A6 gave the best recovery (Fig. 3H). The root-mean-squared (RMS) residuals between the recovered initial conditions and the target initial (Fig. 4A), and those between the predicted and target final (Fig. 4B) decreased with the number of iterations. The terminal (at $n = 50$) residuals for both the initial and final states (Fig. 4A, B), decreased from Case A1 to A6 as the first guess more closely reflected the target initial condition. The SBI first guess (A6), especially, started the first iteration with residuals far smaller than the others and the residuals with the final state remained small in comparison to the other cases (Fig. 4A, B). The rate of convergence was also dependent on the initial guess: the closer the first guess to the target initial condition, the faster the convergence (Fig. 4A, B). The case based on an SBI first guess was one of the fastest converging cases and required the least number of iterations to converge. If the final solution is achieved when the slope of the residual between predicted and target final decreases to below a specified small value, then solving for the initial condition with the SBI first guess is almost an order of magnitude faster than the others. The convergence of Case A1, with the nearly isothermal initial condition, is far smaller than A6 using the SBI first guess and much of this difference arises from the organization of the forward-adjoint looping. For Case A1, the adjoint temperature at t_1 is nearly the negative of the final temperature, in other words, almost possessing the same buoyancy used in the strict reverse calculation (SBI first guess). However, when the adjoint temperature in A1 is advected from t1 to t0, the stored velocity field from the forward calculation is used, but this velocity field is quite different from the actual. The SBI first

guess overcomes this limitation by using the velocity field from the actual backward calculation.

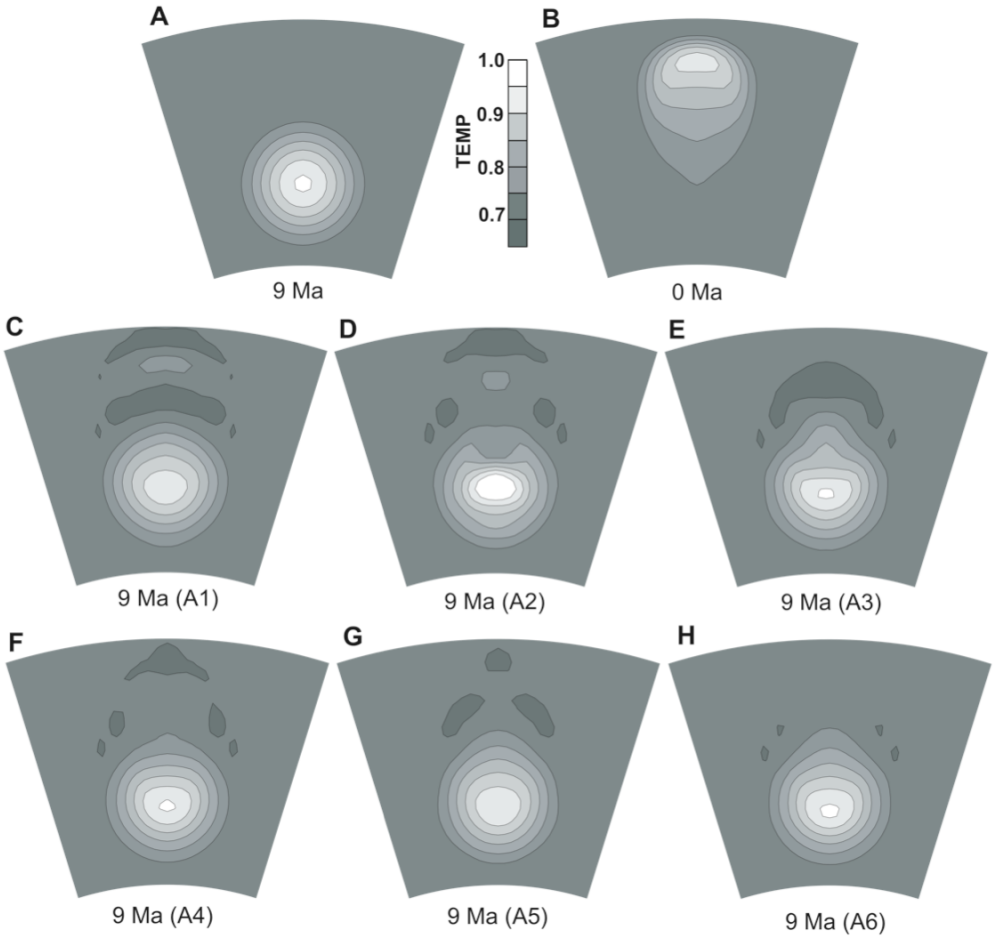

Figure 3 Three-dimensional forward-adjoint models (with a 33×33×33 mesh) for a mantle with a single-layer viscosity and uniform background temperature. Shown is temperature for vertical cross-sections along lines of latitude through center of the domain. Reference thermal states at 9 Ma (A) and present (B). (C to H) Retrieved initial states at 9 Ma using six different initial guesses (Case A1−A6, Table 2). For all cases, 50 forward-adjoint iterations were used.

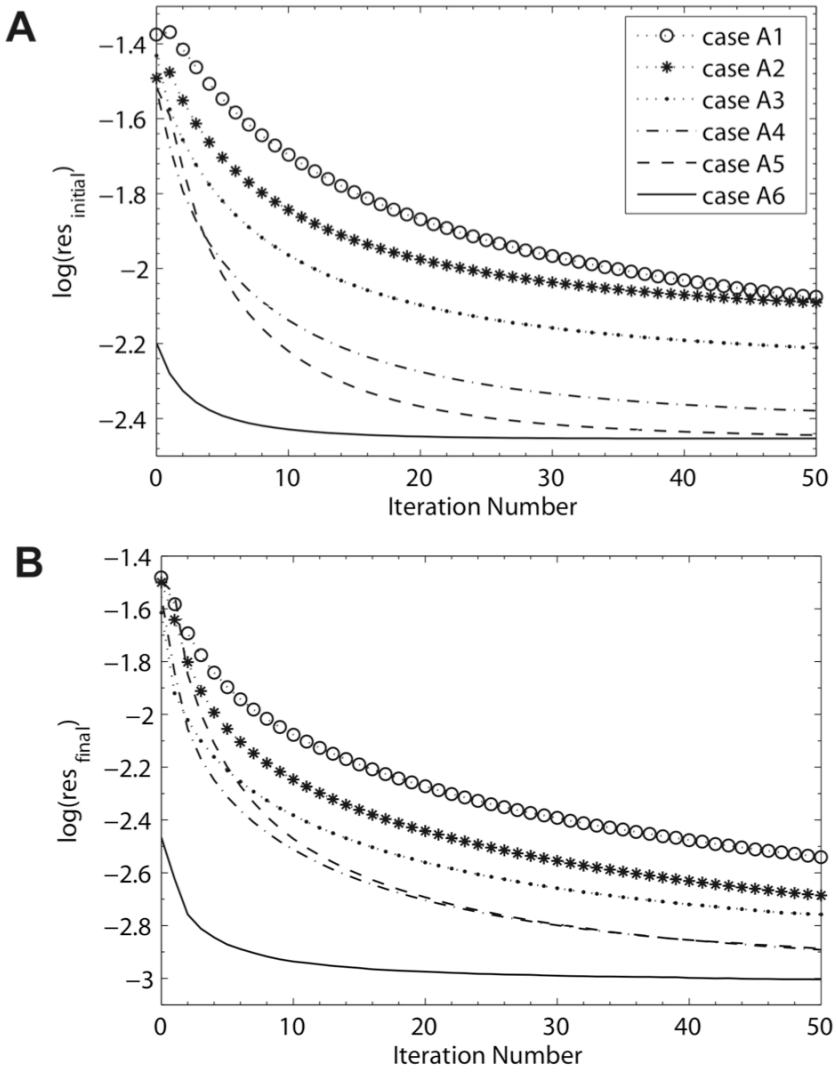

Figure 4 Convergence of the models shown in Fig. 3. (A) Root-mean-squared (RMS) residuals of recovered initial conditions with respect to the reference initial versus iteration. (B) RMS residuals of the predicted final conditions with respect to the reference final versus iteration.

Since the solutions are dependent on the first guess, finding the optimal one is important to decrease the computational cost while obtaining a reasonable solution. Because the SBI first guess gives the best solution to the initial condition, both in terms of the terminal residual and the rate of convergence, we consider this to be a useful means to

obtain an optimal first guess. Another advantage of obtaining the first guess via the SBI is that it requires no *a priori* information of the solution. Algorithmically, it is also easy to obtain.

2.2.2.2. Models with thermal boundary layers and depth- and temperature-dependent viscosities

The second set (Set II) of experiments is geophysically more realistic with a top thermal boundary layer (TBL) representing the lithosphere and a four-layer mantle with temperature-dependent viscosity. The TBL has an error function temperature profile typical of 40 Ma oceanic lithosphere. The viscosities for lithosphere, asthenosphere, transition zone, and the lower mantle, without temperature-dependence, are 10, 1, 10, and 40, respectively. The temperature dependence of viscosity is

$$\eta_T = \eta_o \times \exp(\frac{1}{T + 0.3} - 1) \tag{11}$$

where η_T is temperature-dependent viscosity and η_o is the depth-dependent prefactor. This results in an order of magnitude decrease in viscosity from T=0 to 1. Compared to Set I, we used a higher Rayleigh number at 5.0×10^8.

The target initial condition has the same thermal anomaly as that in model Set I, only that it has a TBL on top (Fig. 5A). The target final condition (Fig. 5B) is 52 Myr after the anomaly had risen through the asthenosphere and eroded the lithosphere. We named six different cases as AL1 to AL6 (L denoting lithosphere). The first guesses in Case AL1 to AL5 had the same anomaly structures as described in Table 2, and they all had the same

TBL as in the target initial. Case A6 is with the SBI first guess. Comparatively, these first guesses in AL1–AL5 had more information on the target initial than those in A1–A5, because we assumed the correct TBL in these guess. On the other hand, Case AL6 (using the SBI first guess) had less information on the initial condition because the TBL had to be entirely recovered with the forward-adjoint looping. All models were realized with a 49×49×49 mesh with an under resolved lithosphere spanned with just two mesh points.

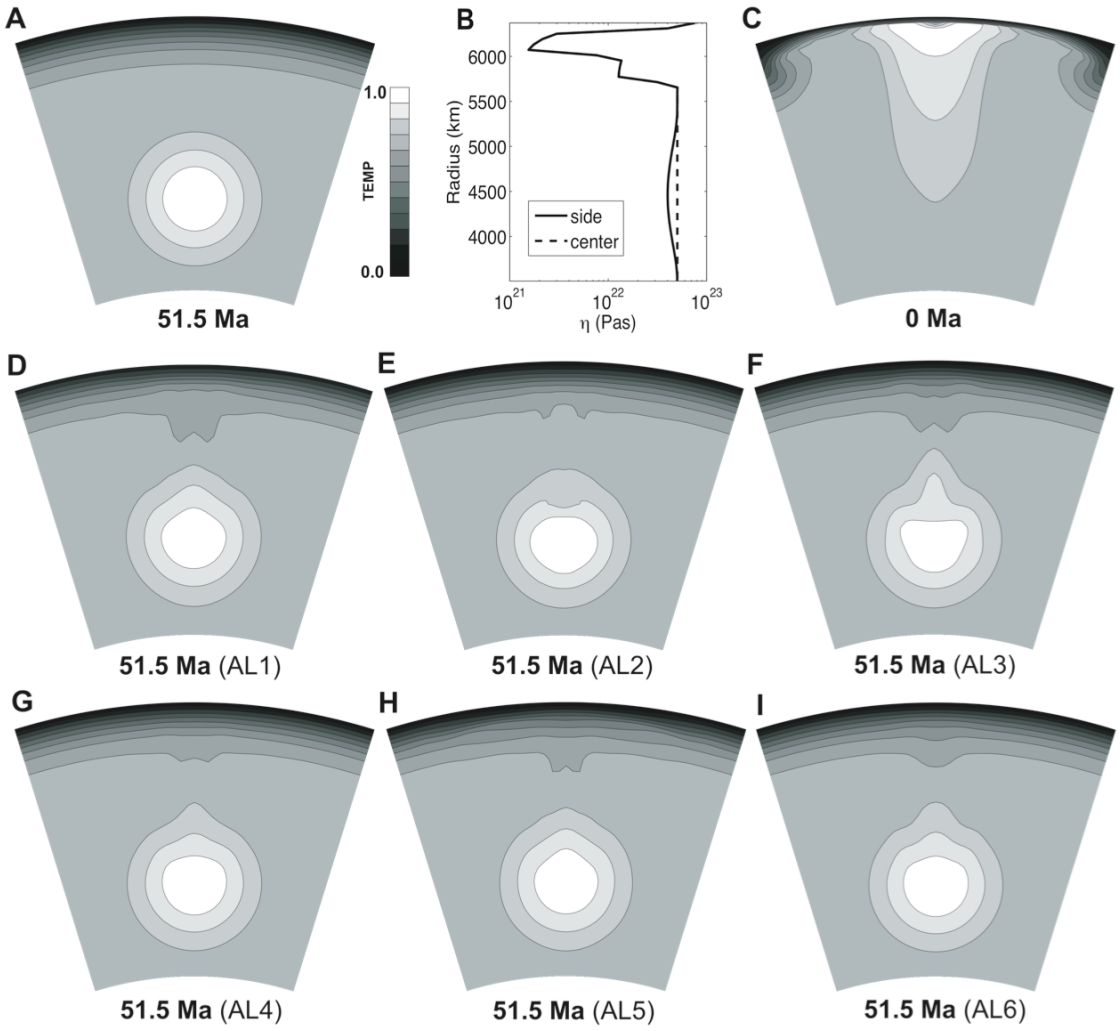

Figure 5 Three-dimension forward-adjoint models (with a 49×49×49 mesh) for a model with a radially stratified viscosity and a top thermal boundary layer. Shown is temperature through vertical cross-sections. Reference states at 51.5 Ma (A) and present (C). (B) Radial viscosity profiles in the reference initial condition. (D to I) Retrieved initial states from six different initial guesses (AL1–AL6) after 50 iterations.

Since these models are more complex, and thus more nonlinear, than models in Set I, a smaller damping factors α with $n_o = 2$ is adopted, in order to avoid overcorrection in the iterative process. We integrated the forward and adjoint equations for 50 iterations to obtain the solutions (Fig. 5C–H). Since the temperature field includes a TBL and a lower mantle anomaly, a small residual would entail recovering both well. The comparison of recoveries in these cases is not as obvious as that of only a rising Stokes sphere (Set I). Case AL5 with the closest initial guess also accumulated substantial errors through the nonlinear interaction between the rising spherical anomaly and the thermal erosion of the lithosphere. Case AL4 and AL6 both gave good recoveries with the smallest residuals between recovered and target initial condition (Fig. 6A), and AL6 among all cases had smallest residual between predict and target final condition (Fig. 6B). The SBI first guess (AL6) also led to fastest convergence, and most of the residuals were reduced within the first 10 iterations. From both the residuals and rate of convergence, we concluded that the SBI still gives the best initial guess even in such a complex model.

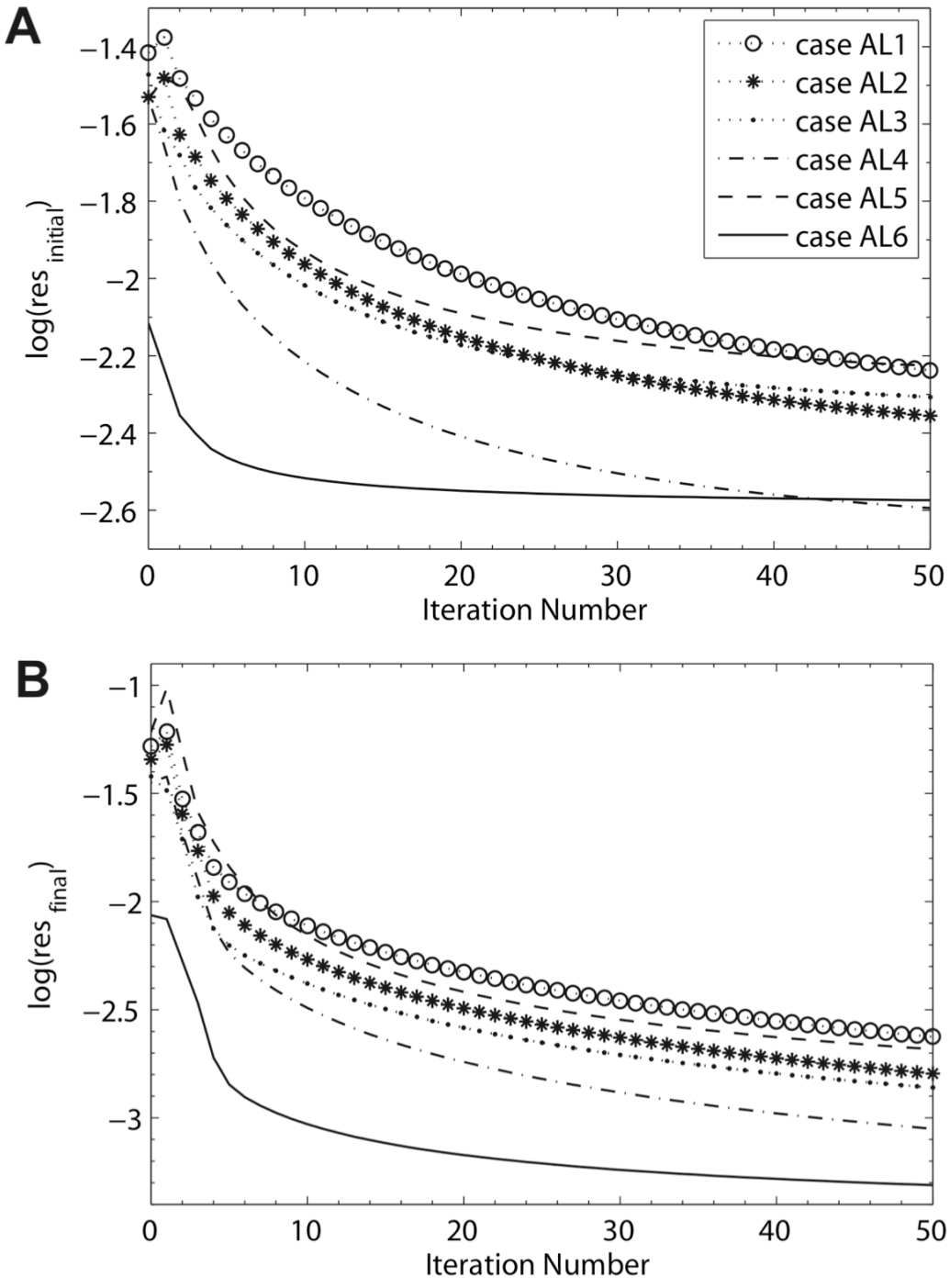

Figure 6 Same as Fig. 4 except for the models shown in Fig. 5.

Other experiments showed that by increasing n_o, hence decreasing α, we could decrease the terminal residuals of the initial condition in AL1 to AL5 upon convergence, some of which (AL4 and AL5) could be even smaller than in AL6, indicating a better recovery, but the terminal residual of the final condition in AL6 was always the smallest. However, for these tests, we had to increase the number of iterations to obtain the same amount of reduction of residuals; in other words, we reduced the rate of convergence substantially in A1 to A5, while A6 always had the fastest convergence and smallest residuals during most of the iterations. This indicates that the SBI first guess always produces good solutions with the least computational cost

2.2.3 Discussion

Inferring initial conditions with adjoint methods for mantle convection seems inherently ambiguous compared to atmospheric circulation problems where direct constraints on initial conditions from measurements in the system interior are used. Using a technique similar to that in Bunge *et al*. [2003], we first inferred initial conditions via the looping between forward and adjoint calculations to minimize the difference between a prediction and the final state of the mantle (a state that can be determined from seismic tomography). An optimal convergence requires some constraint on the initial condition. Starting the first forward calculation with an isothermal mantle was less efficient than with an initial guess obtained by the simple backward integration (SBI) of the convection equations that starts with present-day structure. Even when a Stokes sphere interacts with

and distorts a thermal boundary layer, where diffusion is important, the SBI first guess continues to provide a good estimate for the initial condition.

The adjoint method is an iterative gradient method that solves for a linearized problem. For the final solution to reach the global minimum in the residual space, the trial solution in the first iteration must be close to the true solution. Since the SBI initial guess makes use of present-day mantle information, this inverse of mantle convection approximates the true solution to first order. Therefore, the SBI initial guess guarantees a good solution with the adjoint method, as long as the model has not been run so long that diffusion at boundary layers dominates the problem. However, the approximation of initial conditions based on SBI will face difficulty when the anomalies reach a thermal boundary layer (TBL) and gradually diffuse away, which means an SBI estimate will not provide the same amount of buoyancy force. This is the natural limit for the adjoint method [Ismail-Zadeh *et al*., 2004].

The SBI initial guess is close to optimal for most mantle convection problems because advection dominates thermal diffusion with typical Peclet numbers ~10^3. To best approximate the true solution, an initial guess must capture its total buoyancy and geometry that we demonstrated with several numerical experiments in which either the buoyancy was underestimated or the initial location was incorrect. In these cases, the trial solutions all have large initial errors that must be iteratively removed with forward-adjoint looping. An idealized case with the correct initial location and buoyancy that is close to the actual initial condition recovers the initial condition nearly as well as with the SBI first guess. Since the SBI first guess involves the solution of the three conservation equations (Eq. 2–4), we

obtain a condition that has almost the same total buoyancy as that in the true solution and with its geometry defined through the coupled solution of flow and advection; this initial guess will, of course, lead to a good solution.

Seismology has revealed that the mantle has both low and high velocity regions that putatively represent a complex combination of thermal and chemical anomalies [Masters *et al*., 2000; Ishii and Tromp, 1999; Ni *et al*., 2002]. In these real cases where mantle anomalies have irregular geometry and amplitude, arbitrary initial guesses can hardly capture the true solution in the first place, and the SBI initial guess will be especially beneficial in retrieving a reasonable representation of the true initial condition.

However, it is worthwhile to point out that the tests performed in this chapter all assume that mantle properties, including the viscosity distribution, constitutive relation, and mantle density anomalies are perfectly known. In other words, these are idealized situations, which do not exist in the earth. For geophysical problems, many other unknowns need to be solved. Besides the dynamic properties like mantle viscosity and density anomaly, chemical composition and its temporal variation are other questions requiring solution. The numerical experiments shown in this chapter all treat mantle density anomalies as being thermal in origin, and possible chemical heterogeneities are not considered. In the upcoming chapters, I will try to address several of these issues.

Chapter 3
Constraining Dynamic Properties of Mantle[2]

3.1 Need for Assimilation of Time-Dependent Data in Real Problems

Unlike atmospheric or oceanographic problems where many parameters within the interior of the flow can be measured and calibrated *in situ*, dynamic parameters for the mantle convection problem are obtained indirectly. A good example of such a parameter is the depth dependence of mantle viscosity, unfortunately a parameter that remains uncertain [Walcott, 1973; Hager and Clayton, 1989; Steinberger and O'Connell, 2000; Mitrovica and Forte, 2004]. This of course is problematic for the adjoint problem described in Chapter 1, because what viscosity should be used for the recovery of initial conditions? Another critical parameter for recovery is the magnitude of the temperature (density) within the anomalies. Clearly, important constraints can be placed on this problem from seismic tomography, but high-pressure, high-temperature laboratory experiments have not achieved the ability to uniquely map seismic into thermal anomalies. Thus, even for simple convection models, we should consider these basic model parameters to have uncertainty when the adjoint method is used to infer initial conditions.

As discussed in Chapter 1, a quantitative description of the time dependence of mantle flow requires time-dependent constraints. Here I will explore the surface dynamic

[2] This chapter is based on: 1) Liu L. and M. Gurnis (2008), *Simultaneous Inversion of Mantle Properties and Initial Conditions Using an Adjoint of Mantle Convection*, J. of Geophy. Res., 113, B08405, doi:10.1029/2008JB005594.

topography, a different type of observation from plate motions used in earlier studies [Lithgow-Bertelloni and Richards, 1998]. With the adjoint method implemented in *CitcomS*, we can compute the prior history of thermal anomalies for a given viscosity model and present-day mantle thermal structure. From the restored history, we then predict dynamic topography that can be constrained through stratigraphic constraints, such as tectonic subsidence from boreholes [Heller *et al.*, 1982; Pang and Nummedal, 1995], paleo shorelines [Bond, 1979; Sandiford, 2007; DiCaprio *et al.*, 2009], and sediment isopachs [Cross and Pilger, 1978]. Given these additional observational constraints, there is the opportunity to place limits on mantle viscosity and temperatures.

3.2 Dynamic Topography Constrains Uncertain Mantle Properties

For this study, we designed two sets of synthetic experiments, one for a simple one-layer mantle with uniform viscosity, and the other for a two-layer mantle viscosity structure.

3.2.1 One-Layer Mantle

First let us consider a mantle with a uniform viscosity throughout. On the top surface of the convection model, dynamic topography, *h*, is defined from

$$\sigma_{r,r} = \rho_m g h \tag{12}$$

where $\sigma_{r,r}$ is the total normal stress in the radial direction and ρ_m is the density contrast across the top surface (implicitly assuming that air overlies the solid mantle). At any instant of time, normal stress $\sigma_{r,r}$ is proportional to the temperature scaling ΔT (see Eq. 3). For an inverse problem where we use the present-day seismic tomography to interpret mantle temperature structure, ΔT is the temperature magnitude obtained by mapping seismic velocity variations to thermal anomalies. Together with Eq. (12), we relate dynamic topography with a temperature scaling via a time-dependent coefficient ζ with units, *m/K*. The quantity ζ describes the response of surface dynamic topography with a scaled temperature distribution and mantle rheology structure.

$$h(t) = \zeta(t)\Delta T \tag{13}$$

The rate of change of dynamic topography $\dot{h}$, however, is related to the absolute viscosity of the mantle when the geometry of the thermal anomaly remains fixed [Gurnis *et al*., 2000]. Specifically, in the energy equation (Eq. 4), the rate of change of the temperature anomaly

ΔT is proportional to the product of ΔT and mantle flow speed $\vec{u}$ (i.e., $\Delta \dot{T} \propto \vec{u} \cdot \Delta T$). In a Stokes fluid, $\vec{u}$ is proportional to ΔT and inversely proportional to mantle viscosity η. Considering Eq. (13), we obtain

$$\dot{h}(t) = \frac{\xi'(t)}{\eta} \Delta T^2 \tag{14}$$

For an inverse problem where ΔT and η are unknowns, and *h(t)* and $\dot{h}(t)$ are data constraints, we simplify the problem by rewriting Eq. (14) with Eq. (13)

$$\dot{h}(t) = \frac{\xi(t)}{\eta} h_1^2 \tag{15}$$

where $h_1=h(t_1)$, with t_1 representing present-day time; ξ (or ξ') is a kernel that describes the response of the rate of change of surface dynamic topography assuming a specific mantle viscosity; ξ has units of *Pa/m*. Instantaneously, when the temperature and viscosity structures remained unchanged, Eq. (15) was validated numerically for systems with temperature- and depth-dependent viscosities [Gurnis *et al.*, 2000].

Because *h(t)* and $\dot{h}(t)$ are potentially two independent constraints, and Eq. (13) and (15) each has an independent unknown, ΔT and η, respectively, the independent unknowns might be recoverable. By using h_1 instead of *h(t)* on the right-hand side of Eq. (14), we attempt to partially decouple this two-variable, two-constraint system. Essentially, we use the magnitude of topography *h(t)* to constrain ΔT (Eq. 13), and use its rate of change $\dot{h}(t)$ to constrain η (Eq. 15).

The left-hand sides of equations (13) and (15) are time dependent. On the right-hand-side of the equations, the time dependence has been collapsed into the two kernels, ζ and ξ,

which are evaluated numerically. At any moment of time, ζ and ξ can be found from the solution of Eq. (2) – (4) and are dependent on the viscosity and temperature distribution. Evaluation of ξ requires two successive solutions of Eq. (2) – (4) so that $\dot{h}(t)$ can be found.

Assuming the "structure" of the present-day temperature field is the same as the structure obtained from seismic tomography, we now show how Eq. (13) and Eq. (15) can be incorporated within an iterative scheme to solve for the unknowns ΔT and η based on observed and predicted *h(t)* and $\dot{h}(t)$. Define *j* to be the index of a loop used to refine temperature and viscosity, while *i* remains the index over time as it was in the forward-adjoint looping (Sec. 3). At any given time *i* in loop *j*, the numerical values of the two kernels ζ and ξ are computed as $\zeta_{ij} = h_i / \Delta T^j$, $\xi_{ij} = \dot{h}_i \cdot \eta^j / (h_1)^2$, respectively. Here we treat two kernels as implicit Green's functions. ΔT and η are updated by a method that is similar to back-projection used in seismic topography [Rowlinson and Sambridge, 2003], the difference being the use of implicit coefficients (ζ and ξ) in this case.

$$\Delta T^{j+1} = \Delta T^j + \frac{\gamma_1}{n} \sum_{i=1}^{n} \zeta_{ij} [h_{di} - h_i] \tag{16}$$

$$\eta^{j+1} = \eta^j + \frac{\gamma_2}{m} \sum_{i=1}^{m} \xi_{ij} \left[\frac{h_{d1}{}^2}{\dot{h}_{di}} - \frac{h_1{}^2}{\dot{h}_i} \right] \tag{17}$$

where *m* and *n* are the numbers of sample points within the time series and are potentially different because of the different number of constraints on topography and its rate of change; subscript *d* refers to data (observational constraints); γ_1 and γ_2 are two damping factors with values < = 0.5.

This iteration is at a higher level than that of forward-adjoint looping and we refer to it as the outer iteration. Essentially, seismic tomography at the present day is used to constrain the geometry or depth distribution but not the precise amplitude of mantle temperature anomalies, and the forward-adjoint looping is used to find that geometry during earlier times. The outer looping is used to refine both the scaling between seismic velocity variations and temperatures (or density) and the viscosity distribution. The whole procedure is divided into two parts:

(i) Inner loop: While ΔT and η (without varying temperature dependence) remain constant, perform an adjoint calculation to recover the initial condition with the SBI first guess, and predict the dynamic topography during the final iteration.

(ii) Outer loop: Update ΔT and η via (16) and (17) through the mismatch of the predicted and target dynamic topography and its rate of change.

The whole procedure is terminated upon convergence of the two model parameters.

In a synthetic experiment, a cold spherical anomaly sinks from top to bottom of the mantle within a 3D spherical region; the system has initial (Fig. 7A) and final reference states (Fig. 7B). On the top surface, topography is sampled directly above the center of the anomaly.

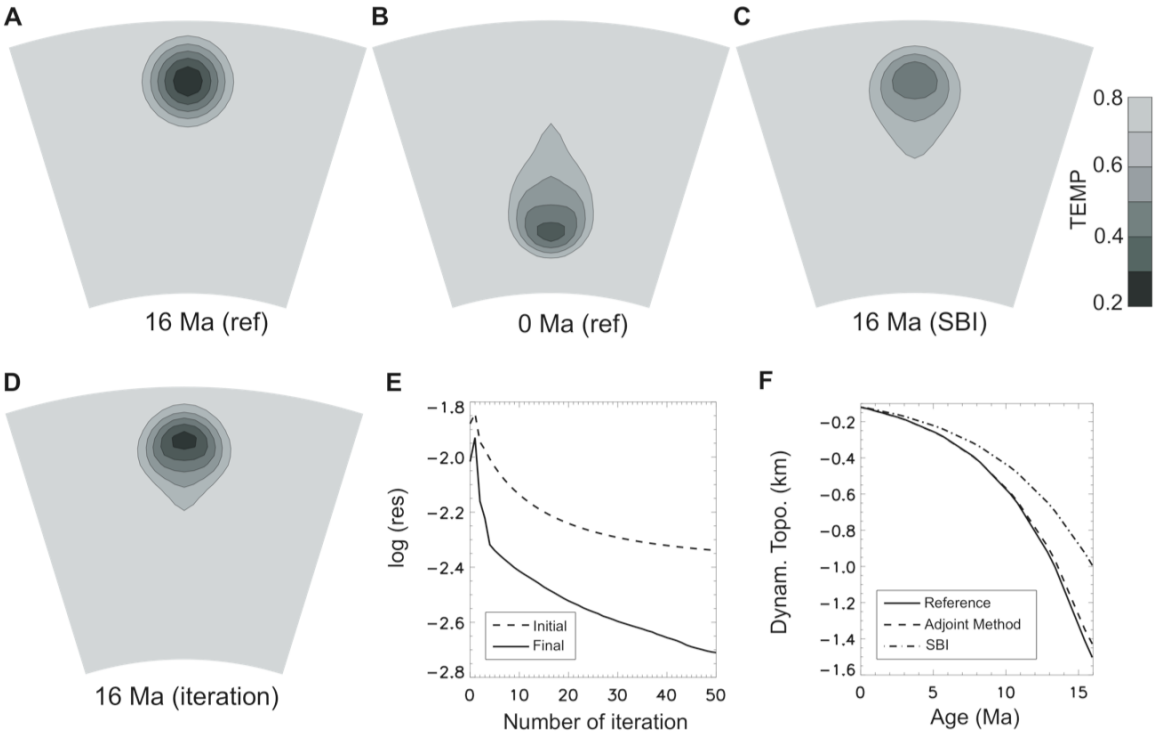

Figure 7 3D models with a single viscosity layer (modeled with a 33×33×33 mesh). Reference thermal states at 16 Ma (A) and the present (B). (C) First guessed initial condition with a simple backward integration (SBI). (D) Recovered initial condition with the adjoint method after 50 iterations. (E) RMS residuals for the initial and final states based on the adjoint method. (F) The predicted dynamic topography histories based on an SBI first guess and the adjoint method, compared against the reference dynamic topography. All calculations assume a known viscosity structure.

To illustrate the effect of forward-adjoint iteration on dynamic topography, we ran the inner loop described above assuming that the temperature scaling and the absolute value of viscosity are known. The SBI initial guess (Fig. 7C) is more diffused in comparison to the finally recovered initial condition after 50 iterations (Fig. 7D). The adjoint method reduces the RMS residuals for the initial and final states by about a factor of 3 and 5, respectively

(Fig. 7E). Consequently, the associated dynamic topography curves from t_0 to t_1 are also notably different (Fig. 7F). The curve from the SBI case deviates from the reference much more than the one from the recovered solution, with a maximum deviation in magnitude by 35% vs. 5% of the reference value at 16 Ma. Although the SBI is a good method to find the best first guess for the forward-adjoint looping, the experiment demonstrates that the simple backward advection of the anomaly (SBI) does not perfectly predict the evolution of dynamic topography.

We then started the outer loop with two initial models (Cases AH1 and AH2) in which the temperature scaling ΔT and mantle viscosity η had "guessed values" that were different from the reference ones. The initially guessed parameters of Case AH1 (Fig. 8A, B at loop 1) were such that its effective Rayleigh number was equal to the actual *Ra* for the reference state while Case AH2 (Fig. 8E, F at loop 1) had an effective Rayleigh number four times smaller. In both cases, we applied the two-level looping algorithm. The inner loop was applied so that the iteration always started with the SBI first guess, and the number of forward-adjoint iterations increased as the index of the outer loop increased. We applied this simplification because the first recovered initial condition was not well known before the constraints on *h(t)* and $\dot{h}(t)$ were applied. Due to the initially under-estimated temperature scaling ΔT in both AH1 and AH2, the first predicted temporal dynamic topography curves had small magnitudes and slopes. By applying the outer loop upon the predicted and reference dynamic topography (Fig. 8C, G), we updated model parameters ΔT and η. The difference in magnitudes of topography *h(t)* forced ΔT to increase in both cases where AH2 increased faster due to a larger difference. Differences in slope $\dot{h}(t)$ normalized by present-

day magnitude of topography h_1 updated the viscosity. The apparently smaller slope in AH1 was actually larger than that of the reference when normalized by h_1, and hence forced the viscosity to increase. The initial smaller slope for dynamic topography in AH2 forced the viscosity to decrease, and the smaller magnitude forced temperature to increase, overshooting the reference temperature. The overshot was corrected as the viscosity also approached the true value. As a result, for both Case AH1 and AH2, the temporal (Fig. 8C, G) and spatial (Fig. 8D, H) distribution of dynamic topography converged to the target curves as the two incorrectly guessed model parameters converged to the reference values after a finite number of loops (Fig. 8A, B and E, F). Most of the model corrections occurred within the first 10 outer loops.

As discussed in Chapter 1, due to the artificially defined initial condition and low resolution of meshing, the recovered initial condition by the adjoint method is not exact, even with the same model that generates the reference states (Fig. 7D). This effect shows up in the recovered model parameters as a deviation of viscosity from the reference value by about −2% and that of the temperature scaling by about 1%. However, the final solutions in both Case AH1 and AH2 are almost identical, indicating the two-level algorithm can both recover initial conditions and unknown material properties.

Under highly controlled set of circumstances, this test shows that the history of the dynamic topography is a valuable constraint on mantle viscosity and magnitude of present day mantle thermal structures. We will then explore the limitations of this conclusion under more realistic conditions.

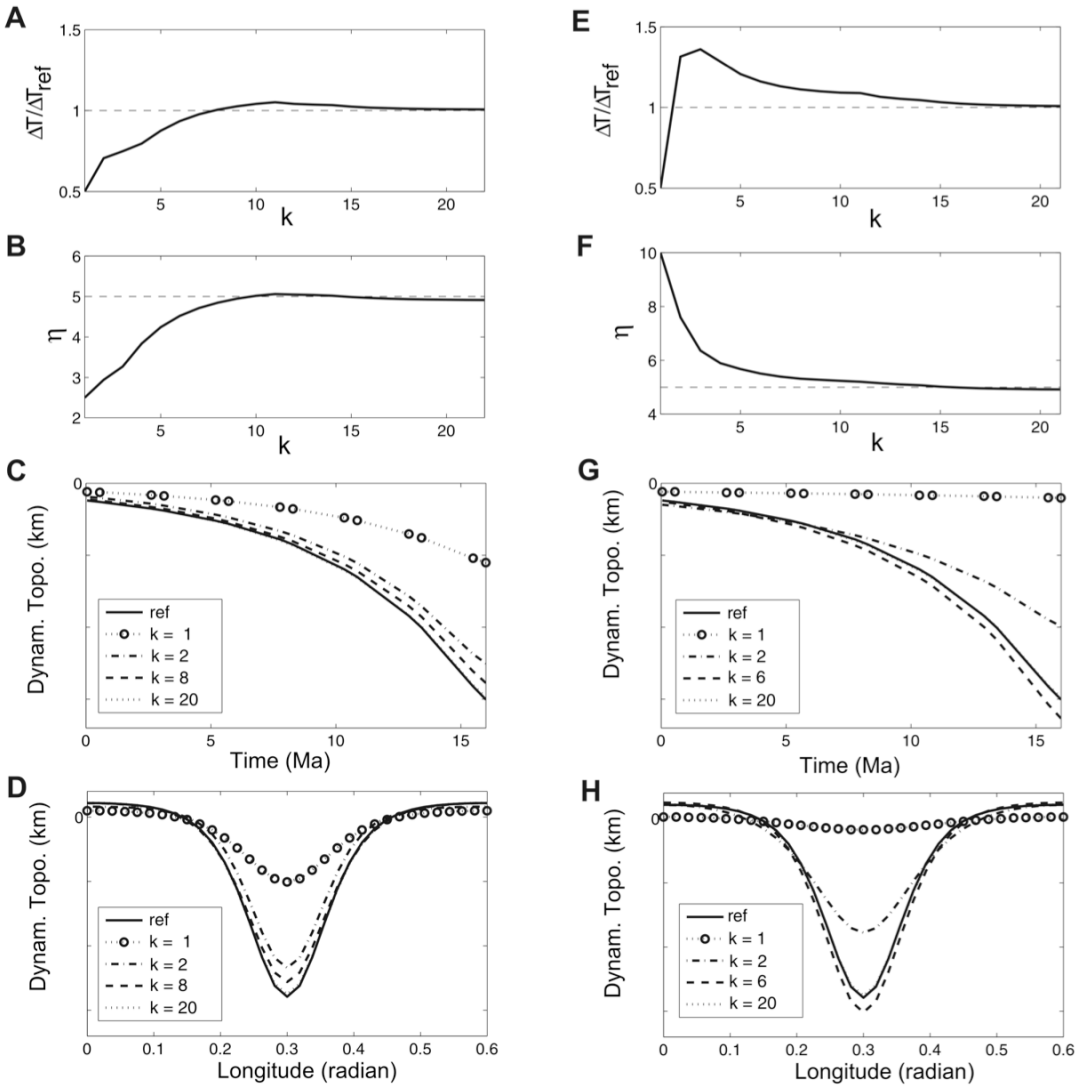

Figure 8 Recovery of model parameters using dynamic topography for models with a single layer. The starting model has either the same effective Rayleigh number (A−D, Case AH1) or a Rayleigh number four times smaller (E−H, Case AH2) than the reference value. All results plotted with respect to the outer loop index (*k*) and are computed from the last iteration of the inner (forward-adjoint) looping. Shown from top to bottom are the temperature scaling (A, E), viscosity (B, F), temporal evolution of dynamic topography recorded at one point on the surface (C, G), and latitudinal profile of dynamic topography across the center of the surface at 16 Ma (D, H).

3.2.2 Two-Layer Mantle

We now consider the geophysically more relevant possibility of a layered mantle viscosity [Hager, 1984; Mitrovica and Forte, 1997]. We used a two-layer mantle and attempted to recover three variables: ΔT (present-day temperature anomaly), η_{um} (upper mantle viscosity), and η_{lm} (lower mantle viscosity). Given this potentially underdetermined problem, we determine what we might hope to recover.

For a thermal anomaly within the upper mantle, the upper mantle viscosity controls the flow velocity, $\vec{u}$, and the evolving dynamic topography. Assuming that the density anomaly has not yet entered the lower mantle the system has only two variables, ΔT and η_{um}, just like the isoviscous mantle discussed above. This assumption is not entirely true since the *h* does depend on the ratio of upper to lower mantle viscosity [Richards and Hager, 1984; Hager, 1984]. Approximately, we still have the linear relation between *h(t)* and ΔT, Eq. (13), and the following relation for $\dot{h}(t)$, which is similar to Eq. (14)

$$\dot{h}(t) \approx \frac{\xi'(t)}{\eta_{um}} \Delta T^2 \tag{18}$$

For a density anomaly within the lower mantle, the flow speed $\vec{u}$ is approximately inversely proportional to η_{lm}, and the surface normal stress that defines *h(t)* is proportional to η_{um}. So Eq. (13) becomes

$$h(t) = \zeta(t) R_\eta \Delta T \tag{19}$$

where $R_\eta = \eta_{um} / \eta_{lm}$, is the ratio of upper to lower mantle viscosity. Consider a static situation in which we neglect time dependence, Eq. (19) is nonlinear due to the fact that $\zeta =$

$\zeta(R_\eta)$, while Eq. (13) is linear since ζ is not a function of ΔT. This implies the inverse problem for a two-layer viscosity mantle is more nonlinear than for a single layer mantle. The relation $\Delta\dot{T} \propto \vec{u} \cdot \Delta T$, together with Eq. (19), leads to the expression

$$\dot{h}(t) = \frac{\xi(t)}{\eta_{um}} h_1^{\,2} \tag{20}$$

where h_1 is dynamic topography at the present day. Again, we use h_1 instead of *h(t)* on the right-hand side of Eq. (20) to avoid the sharing of data constraints. In fact, Eq. (18) and (20) are equivalent: replace ΔT with h_1 in Eq. (18) and Eq. (20) is obtained. This shows that the rate of change of dynamic topography should be a good constraint on the upper mantle viscosity.

Rearranging and discretizing Eq. (20) lead to

$$\eta_{um}^{j+1} = \eta_{um}^{j} + \frac{\gamma_3}{m} \sum_{i=1}^{m} v_i \xi_{ij} \left[\frac{h_{D1}^{\,2}}{\dot{h}_{Di}} - \frac{h_1^{\,2}}{\dot{h}_i} \right] \tag{21}$$

For the other two variables, ΔT and η_{lm}, we have constraint equations (13) and (19). Ideally, we could use Eq. (13) to constrain ΔT by assimilating topographic data associated with density anomalies crossing the upper mantle through Eq. (16). Equation (19) could be used to constrain η_{lm} by topographic data with lower mantle anomalies iteratively

$$\eta_{lm}^{j+1} = \eta_{lm}^{j} + \frac{\gamma_4}{l} \sum_{i=1}^{l} w_i \frac{\Delta T^{j+1} \eta_{um}^{j+1}}{\varsigma_{ij}} \left[\frac{1}{h_{Di}} - \frac{1}{h_i} \right] \tag{22}$$

In Eq. (21) and (22), *m* and *l* are the numbers of sample points within the time series; γ_3 and γ_4 are two damping factors with values < = 0.5; two kernels $\varsigma_{ij} = R_\eta^j \Delta T^j / h_i$ and

$\xi_{ij} = \dot{h}_i \cdot \eta^j / (h_1)^2$; v_i and w_i are weighting functions that change with time. We assumed that v_i (w_i) decreases (increases) linearly from $i = 1$ to l.

However, because a thermal anomaly will move faster in the upper mantle than in the lower mantle, a topographic history would be more heavily weighted in time for the lower mantle, where ΔT largely trades off with η_{lm} when using the dynamic topography (see Eq. 19). In other words, temperature anomaly and lower mantle viscosity are coupled for most of the topographic record.

Therefore, in order to simultaneously invert for all three variables, we should avoid the trade-off between temperature scaling and lower mantle viscosity. We designed a three-level iterative scheme which solves for all three parameters while minimizing potential trade-offs between them:

(i) Inner level: While ΔT , η_{um} and η_{lm} remain fixed, perform forward-adjoint looping to recover the initial condition.

(ii) Middle level: While ΔT remains fixed, update η_{um} and η_{lm} via Eq. (21) and (22) through the mismatch of the predicted and target dynamic topography and its rate of change.

(iii) Outer level: Update ΔT according to Eq. (16).

The whole procedure is terminated upon convergence of the three model parameters.

For an explicit example, we consider a 2D model that simulates a subduction scenario, where a fragment of a cold slab sinks from the upper mantle into the low mantle over a period of 36 Myr (Fig. 9A, B). The dynamic topography is recorded at the surface at some point on the “overriding” plate. We assume that the top surface is fixed; if the plates are moving then the observational record of topography is in the plate frame [Gurnis *et al.*,

1998] and using the mismatch between observed and predicted quantities will be more involved than what the experiment given below suggests.

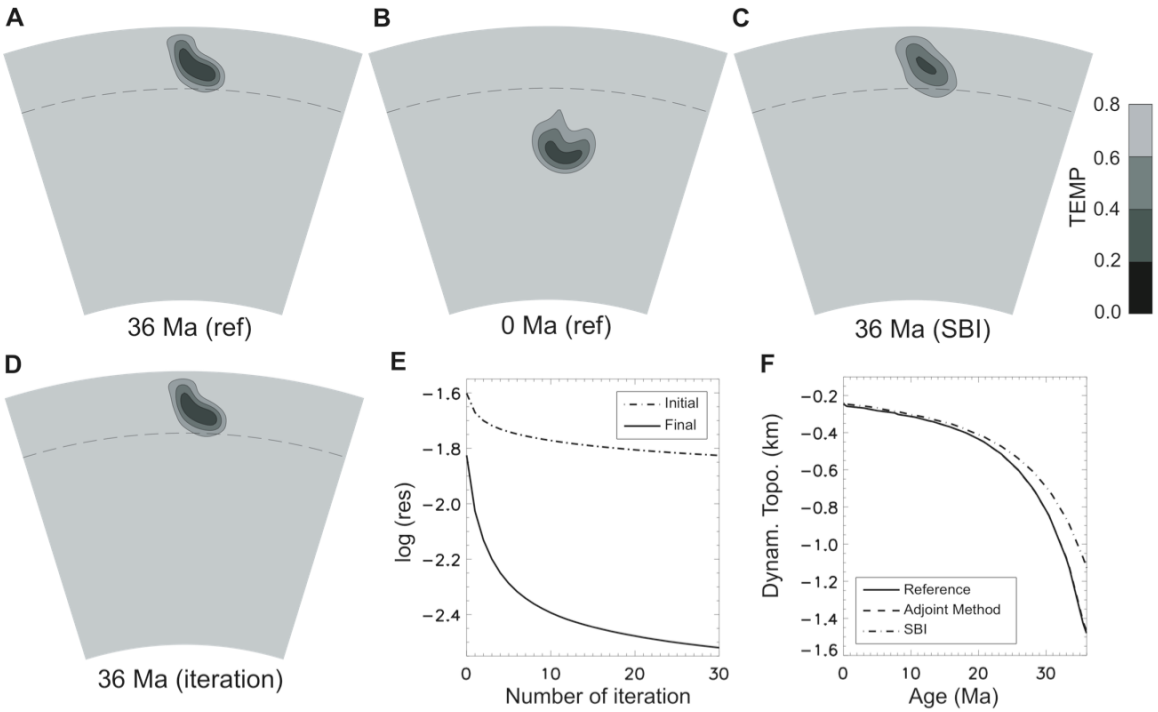

Figure 9 Same as Fig. 7 except for 2D models (on a 129×129 mesh) with a two-layer viscosity. The dashed lines (A–D) indicate the upper and lower mantle interface.

To avoid numerical artifacts, we generated the initial condition by first defining a smooth slab on the surface and then allowing the slab to sink to the position shown in Fig. 7a. A fine resolution mesh with a 129×129 grid is used, to mimic the trench-normal cross-section. We compared the SBI first guess (Fig. 9C) and the recovered solution (Fig. 9D) through the same model that generates the reference states, with residual curves shown in Fig. 9E. The SBI first guess is visually diffused while the recovered solution is nearly

identical to the reference initial state. Moreover, the dynamic topography associated with the SBI estimate deviates from the reference by about 20% at 36 Ma while that with the recovered solution is less than 1%. This indicates that the recovered initial condition with simple forward-adjoint looping is almost perfect if the viscosity and temperature scaling are known *a priori*.

Since the inner level involving the forward-adjoint looping has been described in Section 2.2.1, we focus our discussion on the middle and outer levels. For the middle level, we show several cases with different ΔT values, where upper and lower mantle viscosities are recovered from several initial guesses.

In a set of experiments, we chose ΔT at its reference value but incorrectly guessed both viscosities. We tried two starting viscosity models, AH3 and AH4, that were both guessed to be isoviscous with (η_{um}, η_{lm}) = (5, 5) and (20, 20), respectively, while the target had a layered viscosity, (η_{um}, η_{lm}) = (1, 10) (Fig. 10A, C). Because the initial upper/lower mantle viscosity ratio was overestimated in both models, Eq. (19) implies that the present-day dynamic topography should be overpredicted, as verified as loop 1 in Fig. 10B, D. Since η_{lm} was controlled by the magnitude of topography during the later part of its evolution, the over predicted magnitude of *h* caused η_{lm} to increase (Fig. 10A, C). Since the upper mantle viscosity η_{um} was over-estimated in both AH3 and AH4, the rate of the change of topography was small during the early stages of evolution (Fig. 10B, D). This difference forced η_{um} to decrease quickly in both cases. Changes in both η_{um} and η_{lm} likewise reduced their ratio. As a result, in AH3, both viscosities changed monotonically (Fig. 10A), while in

AH4, η_{lm} first overshot the target (Fig. 10C). This overshoot happened because η_{lm} was forced to increase at the beginning due to an initially overpredicted *h*, but as η_{um} decreased the viscosity ratio went below the reference, *h* became underpredicted, which led to the final decrease of η_{lm}. As the viscosities converged, the topographic evolution conformed to the target in both cases after a finite number of loops (Fig. 10B, D). We conclude that the solution is potentially robust as it does not depend on the initial models. Additional experiments demonstrate that solution errors of both upper and lower mantle viscosities are within 1%.

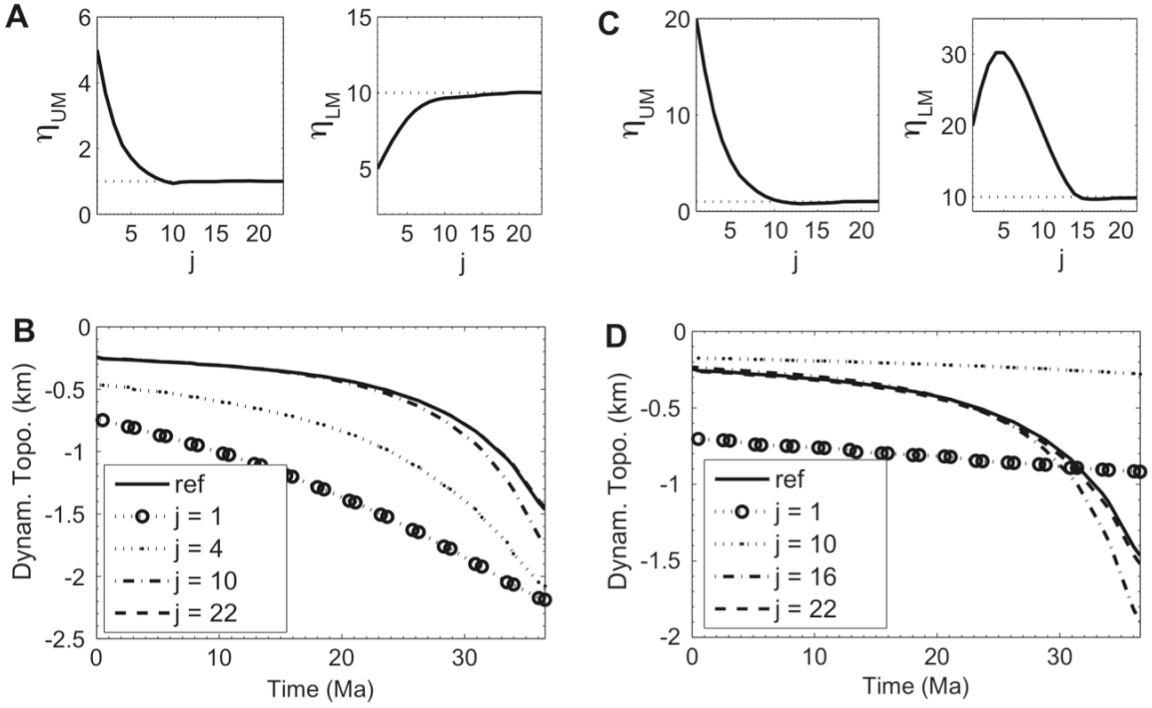

Figure 10 A two-level looping for recovery of both viscosities and initial condition, with temperature scaling at its reference value. Evolution of upper and lower mantle viscosities with respect to middle loop index (*j*) for Case AH3 (A) and AH4 (C), with dotted lines indicating the

reference values. (B, D) Convergence of temporal dynamic topography recorded at one point for Case AH3 and AH4, respectively.

With another set of experiments with all target values as those just described (AH3 and AH4), we incorrectly guessed ΔT so that it was either smaller (AH5) or larger (AH6) than the true value by 50%. AH5 started with an initially isoviscous state, (η_{um}, η_{lm}) = (5, 5) (see Fig. 11A, loop 1); and AH6 started with a higher viscosity, (η_{um}, η_{lm}) = (20, 20) (see Fig. 11C, loop 1). The initial models were chosen such that their effective Rayleigh numbers were not too far from the target values. Parameter recovery in these two cases was similar to what we observed above. Although the viscosity ratio R_η was the same in both AH5 and AH6, the present-day dynamic topographies were different in loop 1, in proportion to the different temperature scaling ΔT (Eq. 19). Consequently, lower mantle viscosities η_{lm} evolved very differently when the temperature was incorrectly guessed. In both Case AH5 and AH6, converged solutions for both viscosities and dynamic topography were obtained. However, although the recovered upper mantle viscosities were always close, there was a tradeoff between lower mantle viscosity and the temperature scaling, as expected from Eq. (19). With more tests on different initial viscosity models, we found that the solutions were robust in that the converged viscosities oscillated around some mean values by no more than 5%. Deviations of the topographic evolutions from the target are instructive (Fig. 11B, D): Due to the tradeoff between ΔT and η_{lm}, the later portion of the predicted curve (closer to present day) always matched the reference curve; however the early portion of the curves were never well predicted since ΔT did not trade off with η_{um}.

Specifically, the earliest portion of the curve was flatter than the reference when ΔT was smaller, and steeper when ΔT larger.

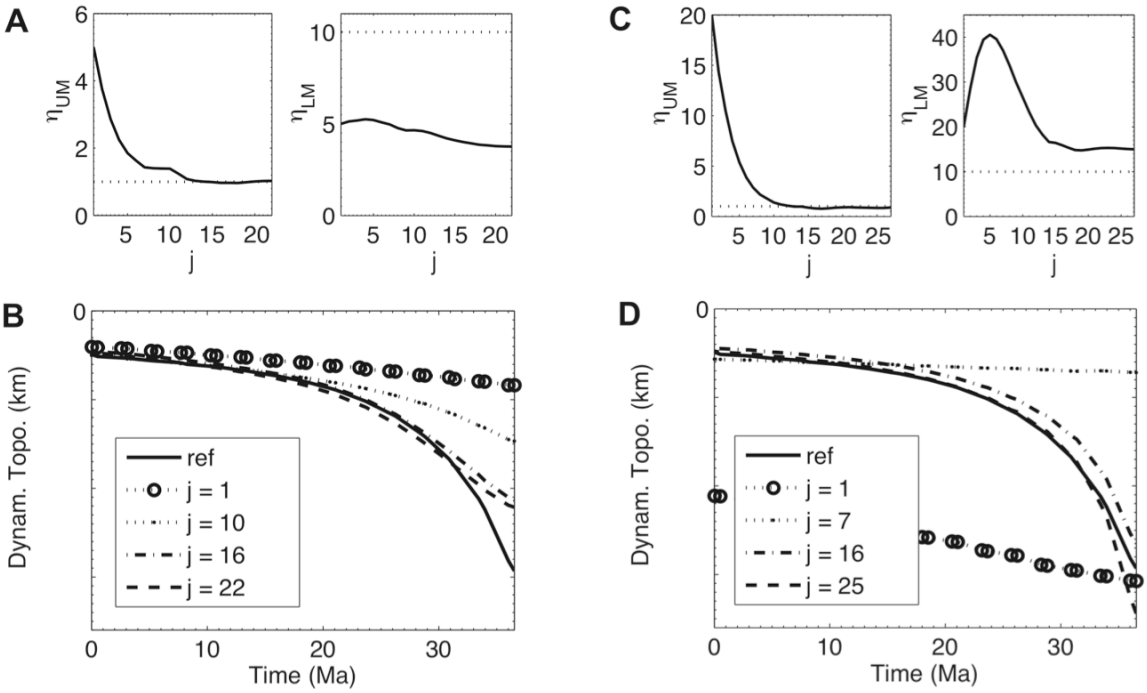

Figure 11 Same as Figure 10, except that the temperature scaling is either smaller (A, B, Case AH5) or larger (C, D, Case AH6) than the reference value by 50%.

This deviation in topographies during the early part of evolution is the basis of an outer level iteration for the update of ΔT. When ΔT is incorrect, lower mantle viscosity trades off with temperature, upper mantle viscosity does not; in theory, dynamic topography can never be predicted exactly if ΔT is incorrect. Eq. (13) and (18) imply that different ΔT, lead to different early topographic evolutions. In practice, we used the very simple relation described by Eq. (13) to update ΔT, constrained from the deviation described above. The iterative relation is given by Eq. (16), where *n* is the number of data points within the time period when this deviation occurred. Instead of using the absolute magnitude of dynamic

topography, we used the amount of change of topography from the initial time to the n^{th} point. Essentially, we use the difference in the slope at the initial stage of subduction.

As an example, we used the values of ΔT in AH5 and AH6 as two starting guesses for the temperature scaling, and then applied an additional outer loop (calling these new cases, AHT1 and AHT2). The procedure for the outer loop is described above. Note that with different values of ΔT, the converged dynamic topography had different slopes at initial times. We calculated the mismatch between the predicted and reference dynamic topography over the early part of topographic evolution and applied Eq. (16) to update ΔT. Consequently, the deviated topographic curves in both AHT1 (Fig. 12A) and AHT2 (Fig. 12E) moved toward the reference as the number of outer loops increased. Convergence of ΔT's were shown in Fig. 12B and F with respect to outer loop, where the symbol size was proportional to the residual between predicted and reference dynamic topography. Both the evolution of topography and that of ΔT indicated a correct convergence. To show the interior process of this three-level looping scheme, we picked some value of ΔT during the evolution as an example. For this ΔT, we plotted the updating mantle viscosities, i.e., the middle level loop (Fig. 12C, G). When the two viscosities converged, the corresponding RMS residuals between predicted and target mantle thermal structure at the initial and final (present-day) time also converged (the innermost loop, Fig. 12D, H). These experiments illustrate well that when ΔT is incorrect, recovered η_{lm} is also incorrect; recovered mantle initial conditions based on these model parameters are far from the reference initial since the RMS residuals remain large (compare Fig. 12D, H with Fig. 9E). By fitting the slope of the topography (Fig. 12A, E), ΔT was constrained to converge. The recovered temperature

scaling in both cases approximated its target value within 1%. How closely the final solution fits the reference values will be affected by the discretization of data and the form of weighting functions in Eq. (16), (20), and (21). In the final solution, all recovered model parameters have errors less than 1%, where the lower mantle viscosity linearly trades off with temperature scaling.

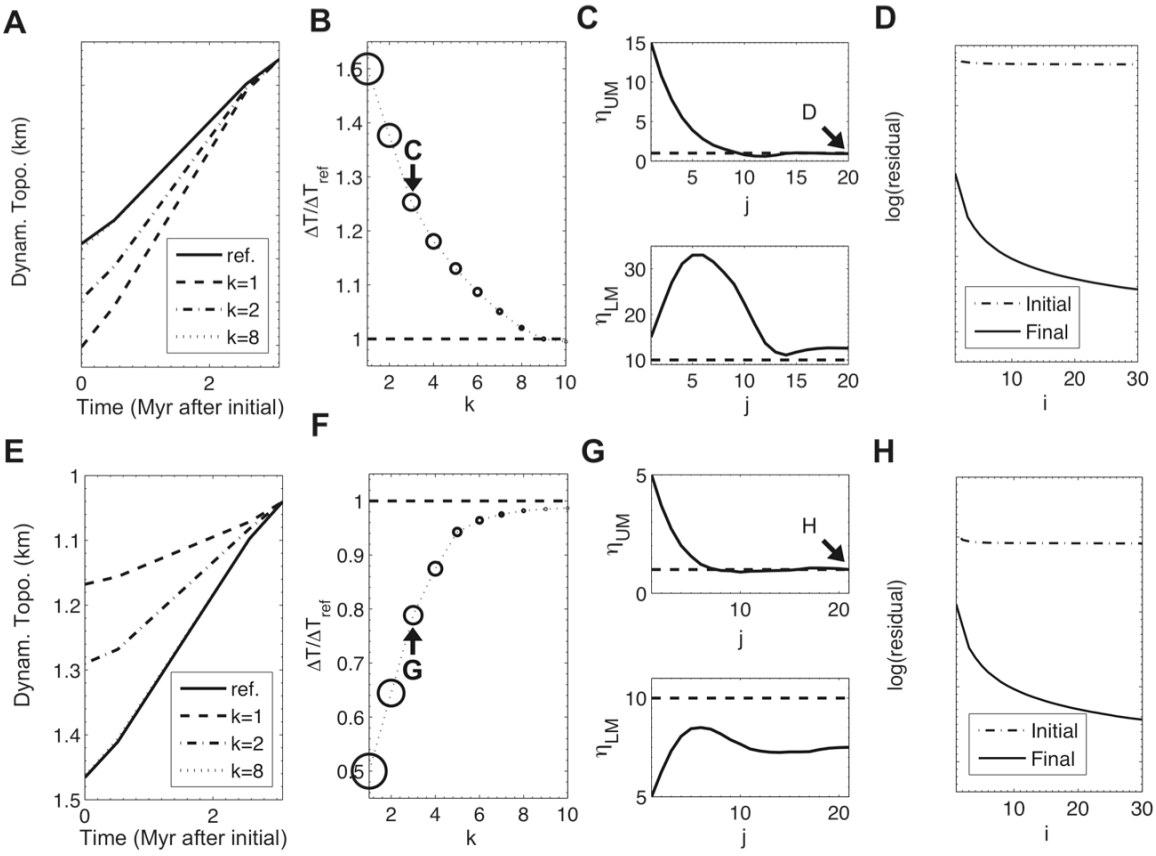

Figure 12 The three-level looping algorithm shown for Case AHT1 (A–D) and AHT2 (E–H), with *i*, *j* and *k* denoting the index of inner, middle, and outer loops, respectively. Shown are evolution of topography at the earliest time (A, E) and temperature scaling (B, F) with respect to outer loop, convergence of upper and lower mantle viscosities versus middle loop, and RMS residuals for both initial and final states of temperature fields for chosen temperature scaling and viscosities. In B and

F, the size (area) of the open circles correspond to the mismatch between magnitudes of predicted and reference dynamic topography in A and E, respectively. All dashed lines indicate the target values.

In summary, our experiments show that, given a temporal record of surface dynamic topography and the present-day mantle seismic tomography showing the geometry of anomalies, this three-level looping scheme allows the recovery of all three mantle dynamic parameters, including upper mantle viscosity, lower mantle viscosity, and the magnitude of the temperature anomaly scaled from seismic perturbations.

3.2.3 Discussion

Combined with dynamic topography observations, the application of the adjoint method can be expanded so that not only can past mantle structures be recovered but also constraints placed on mantle properties. Based on the governing equations, we developed multi-level iteration schemes that constrain both mantle thermal anomalies (the scaling between seismic velocity and temperature or density) and absolute values of upper and lower mantle viscosities. With synthetic experiments, we show that our algorithm is stable and robust. It is worthwhile to note that although this algorithm allows all three model parameters to vary while the final solution remains unique (the uniqueness depends on the recovering power of the adjoint method). In practice, however, we should take advantage of *a priori* knowledge of these quantities, which will reduce the calculation time substantially. This will be essential for large 3D models, which are always computationally expensive.

Synthetic experiments are ideal, and realistic modeling is limited by other factors, including the availability and quality of data. Dynamic topography can be spatially and temporally incomplete, but a complete record is not required for convergence. For example, the dynamic topography constraints on Australian vertical motion since the Cretcaeous are limited to specific intervals of time [Gurnis *et al*., 1998; DiCaprio *et al*., 2009]. Rate of change of dynamic topography associated with upper mantle thermal structures is especially useful and requires better data coverage both in time and in space. Given these features, our method may work well when applied to realistic modeling problems, for example, reconstructing the subduction history of the Farallon plate underneath North America, using the stratigraphic record on the continent of North America and tomographic images under the continent. Errors associated with recovered dynamic topography from stratigraphy will propagate into the solution of lower mantle viscosity and temperature scaling, mainly due to the fact that these two quantities strongly trade off.

The physical significance of this study is two-fold. First, it is a new way to calculate mantle viscosities, which is almost perfect in synthetic tests as discussed in this paper. This method has an equally good recovery of both upper and lower mantle viscosity, not like glacial rebound models sampling mostly the upper mantle. Furthermore, our method puts constraints on the absolute viscosities of the mantle, while previous geoid studies constrain the upper-lower mantle viscosity ratio only. Second, when using real data including seismic tomography, the constraint on the temperature to seismic velocity scaling by this method can be important for understanding the relation between seismic velocities and temperature and pressure under mantle conditions. As discussed later in the recovery of past Farallon subduction processes, we can put constraints on the flat slab subduction mechanism by

tracking an initial buoyant oceanic plateau whose extra buoyancy has slowed the sinking of the slab, causing flattening, and that the relation of the plateau composition and seismic properties can be further measured via extensive seismic ray tracing and waveform fitting.

The inherent power of our inverse method is that a single density anomaly rises (sinks) through the whole mantle and at each depth samples the viscosity through the rate at which dynamic topography changes. Inherent in this idea is that the magnitude of the density anomaly remains fixed. Of course, the assumption of a constant density difference at each depth is unlikely to be true for mantle convection because the mantle is compressible and different materials will compress at different rates as they ascend (descend) through the mantle (e.g., Tan and Gurnis [2007]). Another complexity is the possible temporal variation of mantle viscosity structures before and after certain geophysical processes, say subduction, as is not included in our model either. To further constrain these complexities, the adjoint model should be expanded to allow for assimilation of more independent data constraints, as is one of the future goals this kind of model should move into.

The recovery of initial conditions, two viscosities, and the temperature scaling, from only dynamic topography and the shape of the present day temperature structure (i.e., "seismic tomography") appears to be underdetermined. However, for the synthetic experiments this is not the case. The reason is that we have a set of dynamic topography values: One value of dynamic topography places some constraints on the temperature scaling while two dynamic topographies early in the evolution constrain the shallow viscosity (for example), while two dynamic topographies later in the evolution constrain the deeper viscosity. Together, the set of data leads to the recovery of the viscosities, temperature scaling, and initial condition. In reality, however, the problem might be

underdetermined because the number of unique dynamic topography values will be limited and the mantle presumably has a more complex viscosity structure than simulated by a two-layer model. On the other hand, we also realize that for the synthetic experiments carried out earlier, only one single record of the dynamic topography is used. But in reality, many more geographic sites with extracted dynamic subsidence signals are available, although they may not span the whole time sequence; there are other types of constraints besides signals from isolated points, for example, the distribution, wavelength, and magnitude of subsidence will provide extra constraints.

Another issue for problems tailored to the observational record is plate motions, which are an important constraint on mantle flow [e.g., Hager and O'Connell, 1979]. When dynamic topography is used in the inverse procedure, plate motions complicate the problem since the stratigraphic record moves with respect to the rising and sinking mantle anomalies [Gurnis *et al.*, 1998]. Therefore, a transfer function between the two reference frames is needed. In solving the real geophysical problem, say the Farallon subduction, a software package dealing with the transformation of reference frames has been developed, and the moving plates no longer represent a barrier for the inversion.

We want to emphasize that the use of tomography-based adjoint methods is not the only way to infer the internal state of mantle at earlier times and we realize that there are two other means to arrive at such "initial conditions". In plate-motion constrained mantle flow models, mantle structures can be estimated by a "forward approach" in which a flow model is started earlier in time and then integrated forward to the time of interest [Bunge *et al.*, 1998; Bunge *et al.*, 2002]. Initial conditions can also be inferred via a tectonic approach

based on generating the internal state at a previous time from some combination of surface observations (such as proxies for the configuration of plates, the position of subduction, or hot-spot volcanism). For example, based on the orientation of Mesozoic subduction, Gurnis *et al*. [1998] developed an initial condition at 130 Ma and then forward simulated convection beneath Australia. Bunge and Grand [2000] used the geological arguments that the Farallon slab was flat lying at ~80 Ma and then forward modeled flow beneath North America. These methods complement the inverse models and have different sources of errors. The forward and inverse approaches shared two sources of error: subduction parameterization and radial viscosity structure. However, forward models were sensitive to uncertainties in the plate reconstruction further back in time while inverse models were sensitive to error in reconstructions from the time of interest to the present. We suspect that uncertainty (e.g., the range of structural models permissible at any given time) can be better estimated by comparing the results from these three different methods of generating paleo mantle structures. Consequently, we believe that the adjoint and inverse methods we have developed here should be used in conjunction with the forward and tectonic approaches. Together, these methods will allow a new generation of global and dynamic models to be developed that have well constrained initial conditions.

Chapter 4

Reconstructing the Farallon Plate Subduction beneath North America back to the Late Cretaceous[3]

4.1 Tectonics and Geology Background

Western North America (NAM) has a unique tectonic and geologic history. Since at least Cretaceous time, the westernmost margin of NAM has been a continuous convergent boundary where the Farallon plate subducted and recycled into the mantle. Accompanying the Farallon subduction, terrain accretion and orogeny along the west coast of NAM sustained throughout the Mesozoic and Cenozoic time, with a particularly significant event during the Late Cretaceous to early Tertiary, the Laramide orogeny, reaching as far inland as 1500 km [Burchfiel *et al*., 1992; DeCelles, 2004]. On the other hand, from the middle to the end of the Cretaceous Period, about half area of North America (from the west coast to the middle of the continent) was inundated by shallow seas, forming large thicknesses of marine sediments deposited over a distance of 10^3 km [Bond, 1976; Cross and Pilger, 1978; Liu and

---

[3] This chapter is based on: 1) Liu, L., S. Spasojević & M. Gurnis (2008), *Reconstructing Farallon Plate Subduction Beneath North America back to the Late Cretaceous, Science*, 322, 934–938. 2) Spasojević, S., L. Liu & M. Gurnis (2009), *Adjoint Convection Models of North America Incorporating Tomographic, Plate motion and Stratigraphic Constraints, Geochem., Geophy., Geosys.* 10, Q05W02. ***Author contribution:*** L. Liu developed the adjoint method and ran all the inverse models; S. Spasojević collected the stratigraphic constraints from literature; M. Gurnis supervised the whole workflow.

Nummedal, 2004; Liu *et al.*, 2005]. Formation of both the Laramide Orogeny and Cretaceous western interior seaway (WIS) has remained enigmatic, and this chapter will focus on the latter.

Earlier studies suggest that the observed Cretaceous flooding of NAM (45% by area) would have required a 310 m sea-level rise, resulting in the accumulation of approximately 700 meters of sediments [Bond, 1976]. Since nearly half of the area of NAM Cretaceous marine sediments is significantly thicker than 700 m, Bond [1976] argued that eustasy could not have been the only process that had operated. Cross and Pilger [1978] attributed the excessive sediment thickness and subsidence to subcrustal loading induced by a shallowly subducted plate. Liu *et al.* [2005] determined that regional subsidence of the western interior consists of a short-wavelength flexural loading component that changed on a time scale of a few million years, and a long-wavelength dynamic subsidence component that changed over a time scale of tens of million years. Liu and Nummedal [2004] determined that the wavelength of a dynamic subsidence component was on the order of 1500 km.

At present, the marine sedimentary rocks with Cretaceous ages lie at an elevation of approximately 1 km, but since the long-term variation of global sea level is less than 300 meters [Miller *et al.*, 2005; Haq and Al-Qahtani, 2005], NAM must have subsided and then uplifted over a large length scale. Several numerical models have attempted to explain these inferred vertical motions as dynamic topography induced by negatively buoyant subducting slabs [Mitrovica *et al.*, 1989; Burgess *et al.*, 1997; Lithgow-Bertelloni and Gurnis, 1997]. Mitrovica *et al.* [1989] attributed the WIS to shallow subduction of the Farallon plate that could create a ~1,400 km wide region of dynamic subsidence. Specifically, using 2D

isoviscous forward models, subsidence and subsequent uplift was attributed to changes in the dip angle of the Farallon plate. Burgess *et al.* [1997] expanded on this concept with three-dimensional, variable-viscosity models that attempted to match stratigraphic sequence boundaries. These models shared the common attributes of fixing the dynamics to the frame of reference of the overriding (NAM) plate, and fits to the stratigraphic constraints were obtained by changing the subduction depth and dip to obtain best fits to either continental tilt [Mitrovica *et al.*, 1989] or sediment thickness and sequence boundaries [Burgess *et al.*, 1997]. Lithgow-Bertelloni and Gurnis [1997] used a parameterized global mantle flow model with the slabs falling vertically at a constant rate, in which NAM subsided and then uplifted as it moved to the west over the Farallon slab. However, the predicted subsidence and uplift by the models were about 20 Myr earlier compared to the inferred timings [Lithgow-Bertelloni and Gurnis, 1997].

4.2 Data Constraints and Model Setup

In Chapter 3, we designed an iterative scheme that allows the adjoint method to assimilate time-dependent data, e.g. surface dynamic topography, as extra constraints besides present-day mantle structures, which not only recovers the unknown initial condition, but calibrates uncertain mantle dynamic properties that strongly affect mantle convection. For simplicity, this wider-adaptive adjoint scheme only solves for the adjoint of the energy equation rather than those of all three governing equations of mantle (Eqs. 2–4). In this chapter, we apply the adjoint theory to recover the Farallon plate subduction based on actual constraints, including seismic tompography which outlines the present-day mantle structure, plate motions that prescribe the surface velocity boundary condition of the model, and stratigraphy that acts as proxies of surface dynamic topography. The reason for choosing North America is the availability of all the data constraints necessary for the inverse model.

As the starting point of the inversion, the present-day mantle structure, dominated by Farallon subduction, is best represented by seismic tomography. Medium-resolution seismic tomography models obtained by fitting S or P travel time anomalies [Grand *et al.*, 1997; Van der Hilst *et al.*, 1997; Ren *et al.*, 2007; Li *et al.*, 2008] resolve the Farallon slab at mid-mantle depths as a high seismic velocity anomaly beneath eastern NAM. Given the uncertainties in the detailed structure of the slab and differences between S and P wave sensitivities, these models agree moderately well on the spatial distribution, wavelength, and magnitude of the seismic anomaly (Fig. 13). The present-day Farallon slab largely strikes north-south along the U.S. east coast from Central America to the Arctic. In map view, it

has a width of 500–1,000 km while extending from 800 to 2,000 km in depth, with a typical S wave anomaly of about 1%. In this study, we use an updated version of a global shear wave tomography [Grand, 2002]. The reason we didn't use the higher-resolution regional tomography results generated from the ongoing USArray is that these models came out very recently, as is after this part of the research was finished.

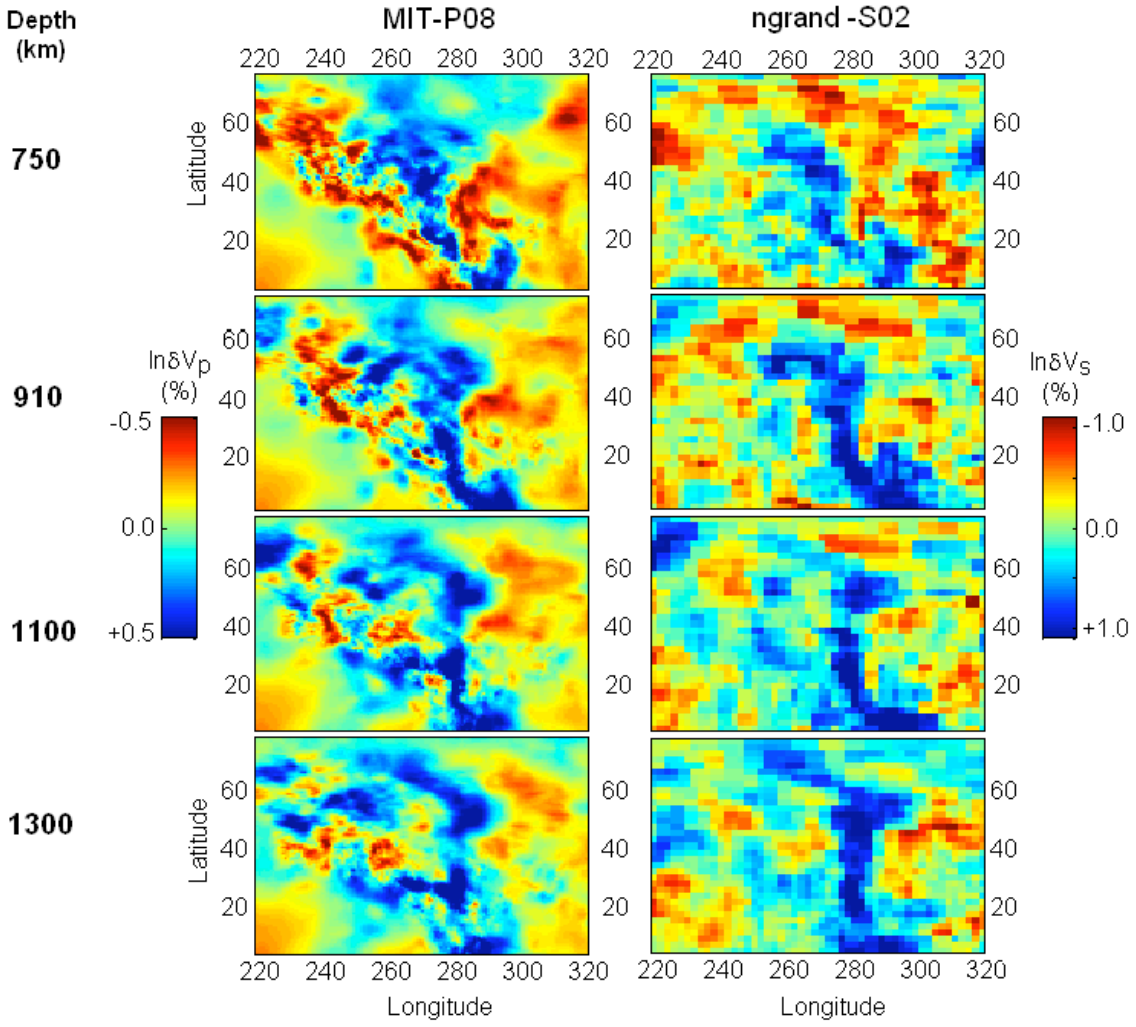

Figure 13 Comparison of the Farallon slab remnants revealed by both a P wave [MIT-P08, from Li *et al.*, 2008] (left) and an S wave tomography [ngrand, from Grand, 2002] (right). Seismic structures are shown at four different depths in the lower mantle under North America, where the Farallon

remnant slabs with largely Late Cretaceous ages are detected. Different color scales are used for the two models. Note the similarity of the two models, especially those of the Farallon remnants (high seismic velocity anomalies).

We use GPlates reconstructions of global plate motions at 1 Ma intervals, in which the plate margins continuously evolve with self-consistent velocities between plates and plate margins [Gurnis *et al.*, 2010]. The rotation of Muller et al. [2008a] is used, implemented in a moving hot-spot reference frame. At 100 Ma, the western margin of NAM is continuously converging from north to south. This persists to 31 Ma, when the Farallon-Pacific ridge intersects the Farallon-NAM trench [Atwater and Stock, 1998], and offshore faults form first followed by formation of the San Andreas Fault in California. The transform segment enlarges at the expense of the convergent margin [Atwater and Stock, 1998] and the Juan de Fuca plate to the north and the Cocos plate to the south continuously shrink. In the south of our region, the Caribbean reconstruction closely follows that of Pindell *et al.* [2006]. From 100 to 80 Ma, North and South America are separated by a spreading center, while the Caribbean region grows by the eastward motion of the Farallon plate between North and South America. At 60 Ma, a new trench and island arc initiates to subsequently become the western margin of southern Mexico and Central America [Pindell *et al.*, 2006].

To constrain the time dependence of the inverse dynamic model, we use paleo shorelines [Smith *et al.*, 1994; Bond, 1978], borehole tectonic subsidence curves [Pang and Nummedal, 1995; Liu *et al.*, 2005] and a set of Late Cretaceous isopachs [Cook and Bally, 1975] associated with the Cretaceous WIS (Fig. 14). The seaway started developing in the

early Cretaceous time by southward transgression from the Arctic and northward transgression from the Gulf of Mexico [Sloss, 1988]. By the Late Cretaceous time the WIS developed into a large epicontinental sea stretching from the Gulf of Mexico to the Arctic, and having an east-west extent of thousands of kilometers [Smith *et al*., 1994]. Using the boundary between preserved marine and nonmarine sedimentary rocks, Smith *et al.* [1994] defined eight paleoshorelines from Late Cretaceous to present (at 95, 85, 70, 60, 45, 30, 20, 12 Ma). During the Late Cretaceous time, the western edge of the seaway was located close to the Sevier belt [Sloss, 1988; Liu *et al*., 2005], while the eastern shoreline migrated slightly eastward from 95 Ma to 70 Ma [Smith *et al*., 1994]. The retreat of the seaway commenced at the end of Late Cretaceous, and the inland sea withdrew completely by the early Cenozoic time [Smith *et al*., 1994].

After collecting all the data constraints, we assimilate plate motions and seismic tomography in the adjoint convection model to predict stratigraphy, in order to better understand the relation of Farallon plate subduction and vertical motions of the continent. The closed plate polygons describing plate motions allows us to represent the mantle and moving plates with separate reference frames and to better link vertical motions to the stratigraphic record on a plate, as demonstrated for the evolution of Australia [Gurnis *et al*., 1998].

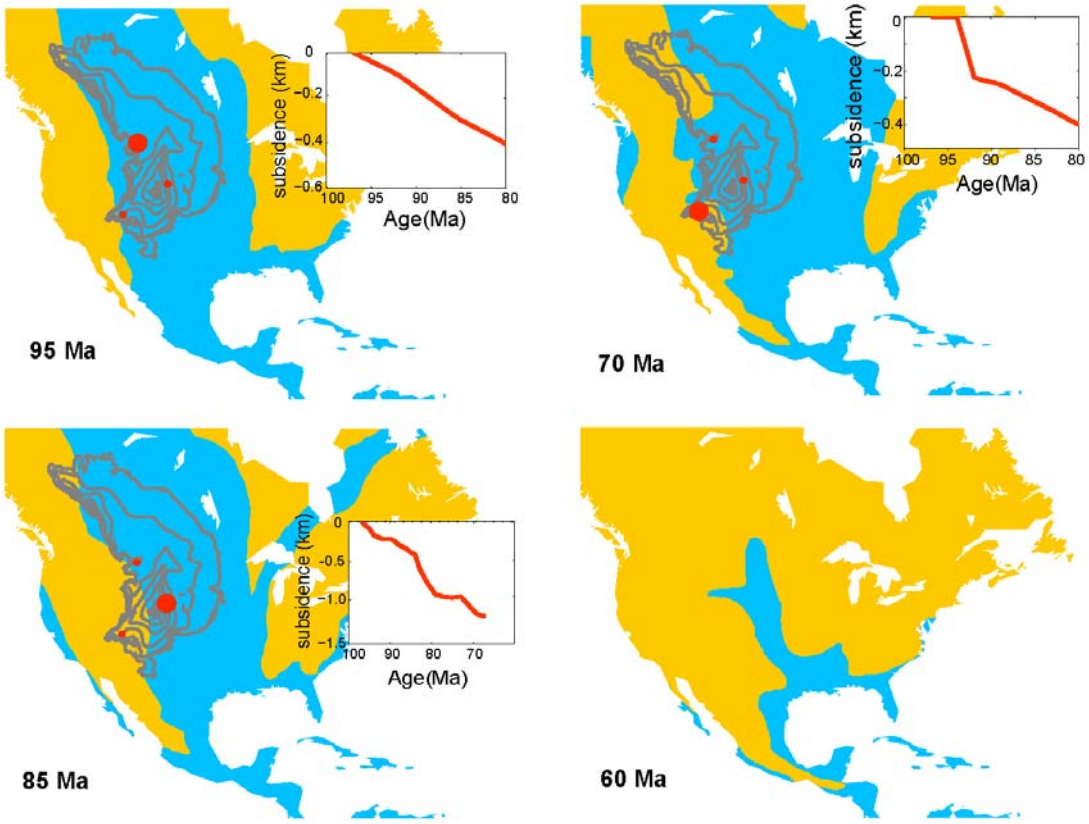

Figure 14 Time-dependent stratigraphic constraints over North America used in the inverse model. Blue areas represent the marine inundations from the Late Cretaceous to early Tertiary. Gray contours show cumulative sediment thickness during the Late Cretaceous. Inset red curves are backstripped tectonic subsidence rates inferred from borehole stratigraphy data, with the corresponding borehole site highlighted with a big red dot (a total of three boreholes are shown). See text for the source of reference.

For simplicity, we model the Farallon subduction by solving equations of a thermal convection system (Eqs. 2–4). This assumption is potentially problematic, as chemical compositions of the subducting oceanic crust and ambient mantle are different. However, since we are looking for a simple representation of the effective density anomalies for both

thermal and chemical structures, we decided to use the term “effective temperature anomaly”. Our detailed motivation is as follows. First, below the resolution of the seismic tomography inversion [Grand, 2002], there is a trade-off between seismic anomaly and grid spacing. The absolute seismic velocity anomaly is not uniquely known and the inferred temperature or density cannot be uniquely known. Consequently, our effective temperature anomalies are underestimates of the actual temperature anomalies (assuming that seismic anomalies are thermal in origin, see below). However, because the sinking rate of structures in the mantle and their influence on dynamic topography in the adjoint models are mostly sensitive to net buoyancy, the seismic ambiguity does not adversely influence our inversion scheme. Second, it has now become clear that in addition to thermal effects there is substantial chemical heterogeneity in the mantle [Ni *et al.*, 2002; Ishii and Tromp, 2004; Trampert *et al.*, 2004] and the mapping between seismic anomaly and temperature and density is likely to be both depth- and geography-dependent. In the adjoint models, the dynamic topography and its rate of change are sensitive to density anomalies, which could have both thermal and compositional contributions. However, since the quantity that we are inferring is diffusive, we have decided to refer to it as “effective temperature”. Third, both mineral physics and other geodynamic studies suggest that the mapping from seismic shear anomalies to density anomalies do not vary much within the depth range where the present-day Farallon remnants are detected [Karato and Karki, 2001]. Since density variation is what drives mantle flow in our model, this effective temperature is a simple expression of buoyancy while assuming a thermal expansion coefficient that is independent of depth.

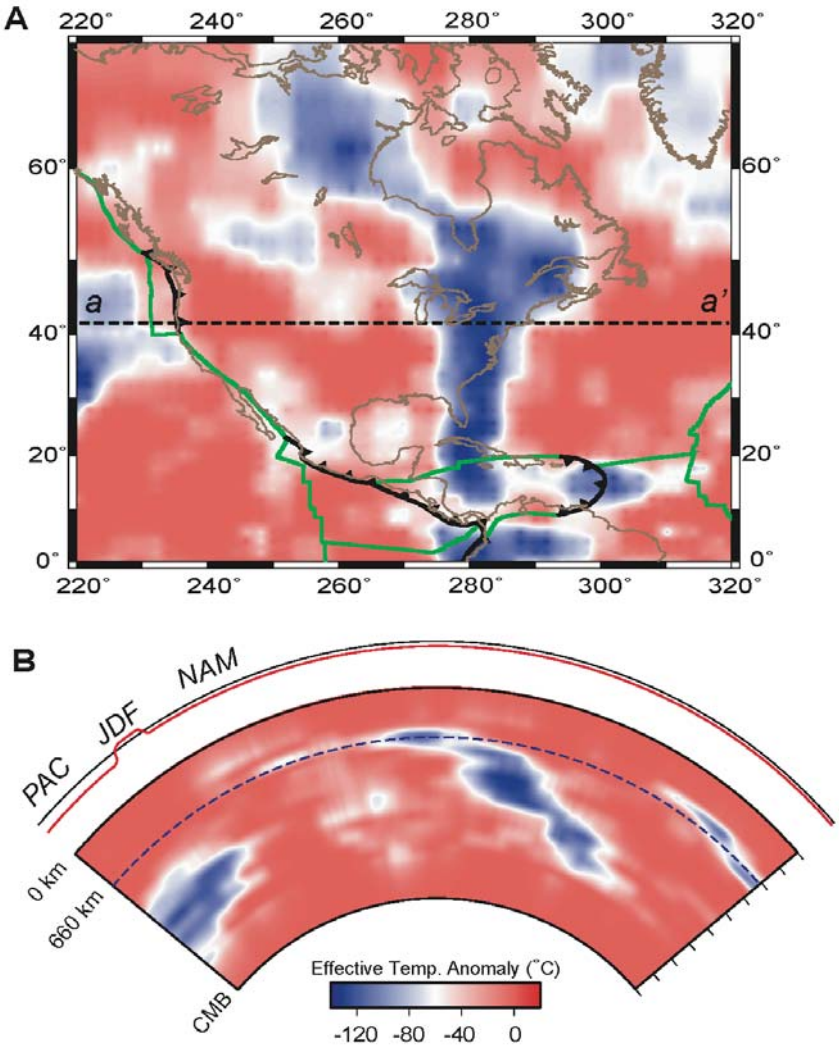

Figure 15 Position and geometry of the present Farallon remnant slabs. A. Map view colors are for 1300 km depth. Green lines represent spreading centers or transform faults, black toothed lines subduction zones, and dark brown lines coastlines. B. Vertical cross-section through the Farallon slabs along 41 °N shown as profile a-a' in A. Red line on top indicates the imposed plate motion, with east being positive. PAC - Pacific. JDF - Juan de Fuca, NAM - North America.

The present-day mantle density (buoyancy) field is first estimated from seismic tomography. The shear wave tomography result from Grand [2002] is converted to effective

temperature anomalies with a scaling factor of 2×10^3 ºC/km/s (Fig. 15). The upper 250 km of the seismic signal associated with the North American craton is removed since it is likely neutrally buoyant [e.g., Goes and van der Lee, 2002]. We also remove structures below 2400 km depth where there is a clear gap in the tomographic image. For the rest, we assume a constant seismic to temperature scaling that we will further constrain by fitting the model predictions to stratigraphic data. All values for the physical quantities used in the model are described in Table 3.

Table 3 Parameters for Models with Data Assimilation

Parameter	Symbol	Value
Thickness of the mantle	D	2891 km
Gravitational acceleration	g	9.81 $m\ s^{-2}$
Reference mantle density	ρ_m	3300 $kg\ m^{-3}$
Reference viscosity	η_o	10^{21} Pas
Thermal diffusivity	K	$10^{-6}\ m^2\ s^{-1}$
Coefficient of thermal expansion	α	3×10^{-5}
Super-adiabatic temperature drop from CMB to surface	T_0	400˚C

We first designed a regional model that covers a domain twice as wide (east-west) as the NAM plate, allowing the plate to move since 100 Ma with all observations remaining >1000 km from the vertical boundaries. The reflecting side boundaries caused a lower

mantle return flow restricting the horizontal motion and resulting in the Farallon slab positioned farther to the west in the Late Cretaceous compared to the global model. In order to avoid such artifacts associated with the imposed vertical boundaries, we decide that only global models are suitable for this and similar studies.

Our global model uses 12 caps with 129×129 nodes in each cap (approximately 40 km resolution in map view) and 65 grid points in the radial direction. We assume a free-slip and isothermal core-mantle boundary and an isothermal surface. A Rayleigh number (based on thickness of the mantle) of 9.4×10^{6} is used. We parameterize the model with a three-layer viscosity structure, which includes a lithosphere above 100 km with constant 5×10^{22} Pa s viscosity, the upper and lower mantle separated at 670 km depth with varying viscosities to be constrained. We also adopt a temperature dependent rheology, in which laterally viscosity increases exponentially by one order of magnitude for a temperature drop of 200 ^{o}C.

4.3 Constraining Uncertain Mantle Properties

In practice, the inversion for the initial condition given a set of mantle properties is following the algorithm described in Chapter 2, where a first guess based on a simple backward integration is used in order to reduce computational costs. However, constraining of mantle properties including viscosities and slab density anomalies is different from the multi-looping iterative scheme described in Chapter 3, because the actual constraints from the stratigraphic records associated with the WIS allow for a more efficient solution process, as we will detail later.

As discussed earlier, a simple backward integration (SBI) of the present-day mantle temperature anomalies provides a first order estimate for the initial condition of mantle convection. Starting with the 3D structure of Farallon remnant slabs in the lower mantle (Fig. 15), we make an SBI run by reversing the sign of gravity and the sense of plate motions imposed at the surface, so that North America (NAM) moves to the east backward in time and the Farallon slabs move upward toward the surface instead of sinking deeper into the mantle. As can be seen from Figure 16, when the Farallon slab rises into the upper mantle, it deflects eastward rather than westward, and this leads to a geophysically unreasonable subduction geometry where the top part of the slab extrudes far beneath North America instead of connecting to the Farallon plate to the west of the trench. This problem cannot be overcome either by varying the radial viscosity structure or by performing additional forward-adjoint iterations. Such a model is also inconsistent with the temporal sequence of subsidence and uplift of the western interior [Mitrovica *et al.*, 1989; Burgess *et al.*, 1997]. Essentially, the present Farallon seismic anomaly is too far to the east to be

simply connected to the Farallon-North American boundary in the Mesozoic, a result implicit in forward models [Bunge and Grand, 2000].

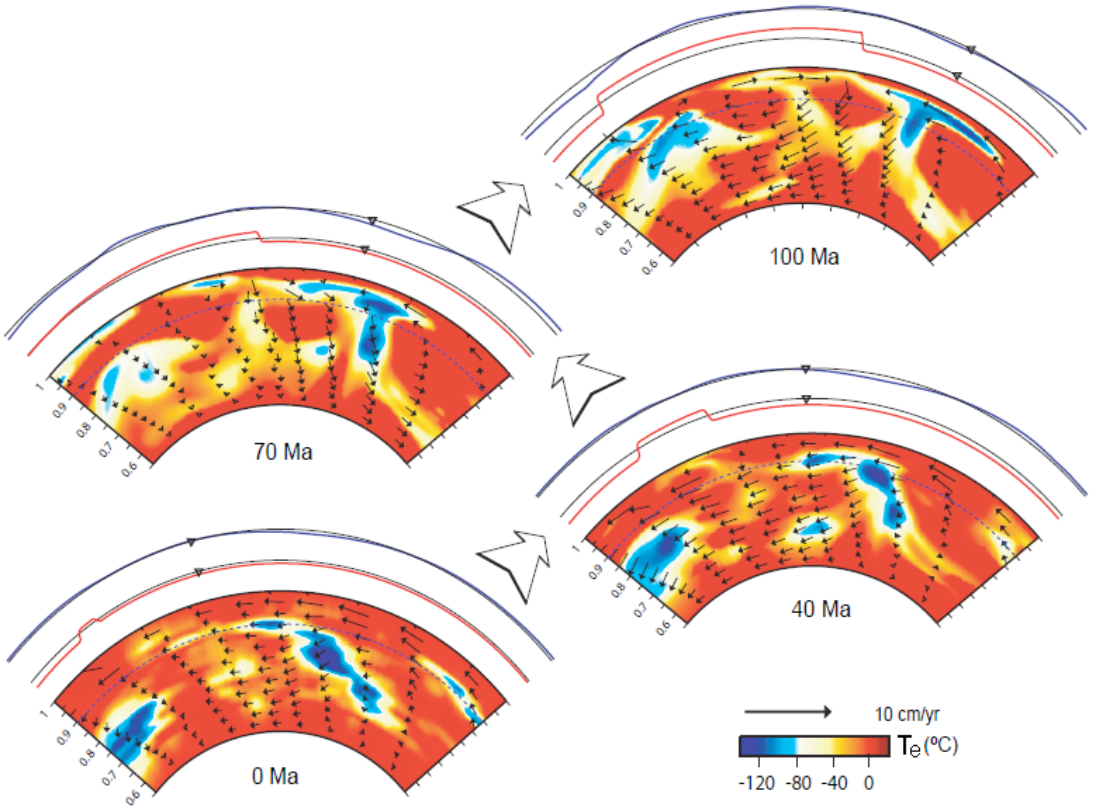

Figure 16 A vertical profile through the whole mantle along 41 °N shows the simple backward integration (SBI) of the Farallon slabs, with the lower:upper mantle viscosity of 15:1 (relative to 10^{21} Pa s) and the maximum effective temperature anomaly (T_e) of 160 ºC. Background color represents the temperature field, where the vertical axis shows the normalized radius and the dashed horizontal line represents 660 km depth. Red curves on top show imposed plate motions, and blue curves dynamic topography, with black triangles indicating the position of a borehole site (41.6 ºN, 254 ºE) about 250 km north of Denver. Arrows indicate the velocity vectors of the mantle flow. Both plate motions and mantle flow are shown in the forward sense of time.

The artifact is inevitable because the present-day Farallon slab does not form a

continuous linear feature in the upper mantle that mechanically connects to the oceanic plate, and therefore, the lower mantle slabs tend to follow the imposed plate motion of North America, rather than that of Farallon. There are two possible causes for this phenomenon. One is that the upper mantle part of the slab has not been detected by seismic tomography due to either poor data coverage or limitation of inversion techniques. Recent higher resolution tomography models still show significant differences in the upper mantle Farallon slab structures [Sigoloch *et al.*, 2008; Burdick *et al.*, 2008; Roth *et al.*, 2008], potentially implying that a robust tomography model of the Farallon slab is yet to come.

Another possible reason is that the Farallon slab indeed broke up during subduction sometime in the past, and this has led to the uncorrelated upper and lower mantle seismic images. Slab failure and breaking is a highly nonlinear dynamic process, whose realization requires sophisticated slab rheology with ultra-high numerical resolution [Burkett and Billen, 2009]. Beside these numerical challenges, there is also little observational evidence that could constrain this possible process. Our global inverse models, with a three-layer mantle viscosity structure and a Newtonian rheology, cannot possibly resolve this detachment process, which would require a more sophisticated forward model with a finer grid.

Since we are only interested in the first order dynamics of the Farallon subduction, we avoid unnecessary complexities by assuming that the oceanic plate should be mechanically coupled to the descending Farallon slab during active subduction. We realize this physical intuition through a stress guide, which consists of a weak horizontal top layer [Manea and Gurnis, 2007] and a high viscosity bottom layer that couples the slab to the

oceanic plate to west of the trench (Fig. 17).

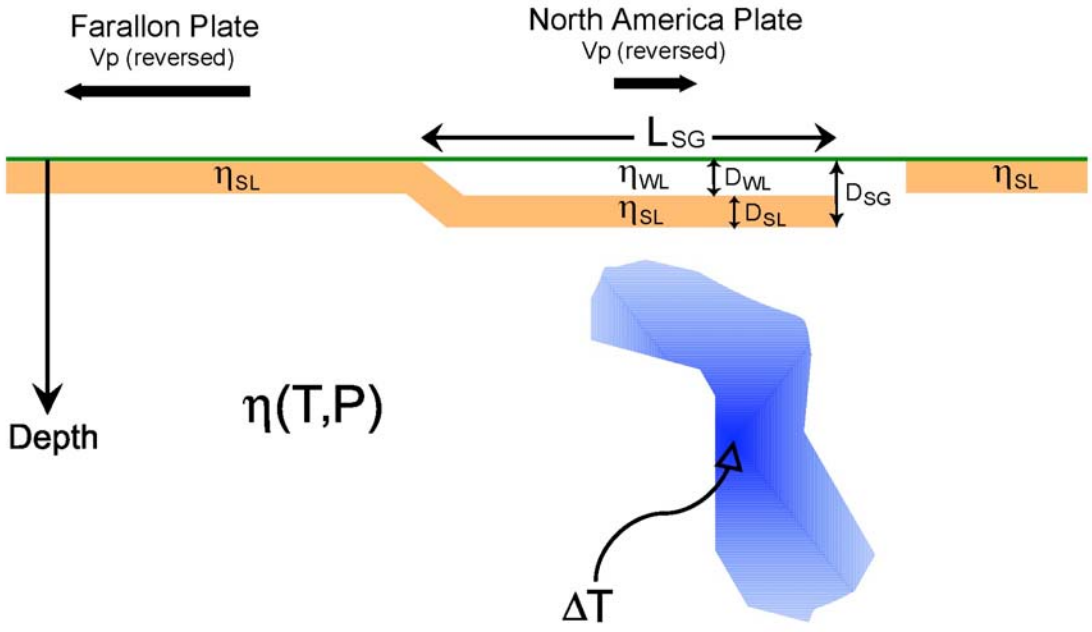

Figure 17 A sketch showing the parameterized stress guide in a trench-normal cross section. The blue structure represents the Farallon slab in the mantle where thermal anomaly drives mantle flow with ΔT being the effective mantle temperature anomaly seen through seismic tomography. The brown-colored layer to the left of the trench represents the oceanic lithosphere and, to the right, the strong layer of the stress guide (at ~100 km depth). Symbol notation: η_{WL} (D_{WL}) is viscosity (thickness) of the weak layer, η_{SL} (D_{SL}) viscosity (thickness) of the strong layer, D_{SG} (e.g. $D_{WL} + D_{SL}$) total thickness of the guide, L_{SG} length of the guide, and $\eta(T, P)$ temperature- and pressure-dependent viscosity.

By incorporating this parameterized stress guide in the inverse model, the cold slab material becomes preferentially attached to the Farallon plate, a process judged more reasonable in terms of actual subduction. Fig.18 depicts the recovered Farallon subduction

after multiple forward-adjoint iterations, with the present-day mantle structure well predicted. Comparison between Fig. 16 and Fig. 18 implies that the stress guide strongly influences slab motion horizontal in the upper mantle, while lower mantle flow is less affected. As the cold slab material rises in a backward sense, the upper part of the slab moves faster horizontally toward the trench than the lower part, and this leads to the formation of a flat to shallow dipping slab around 70 Ma extending 2000 km inland from the trench (Fig. 18).

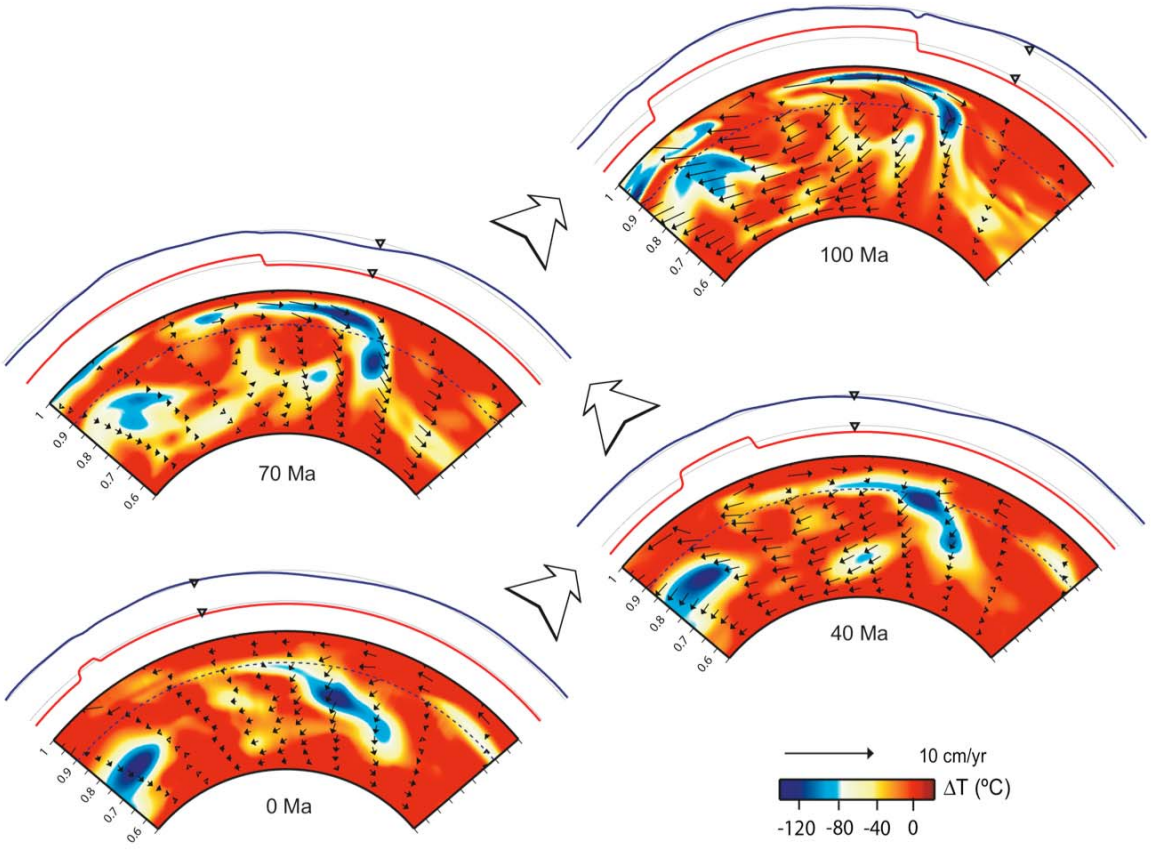

Figure 18 Adjoint recovery of the Farallon subduction, with a parameterized stress guide. Otherwise, the same as Figure 16.

The convergence of the forward-adjoint iterations is shown in Figure 19, for a model with the lower:upper mantle viscosity of 15:1 (relative to 10^{21} Pa s) and the maximum effective temperature anomaly (T_e) of 160 ºC. As the number of forward-adjoint iteration increases (A to C), the structures at 100 Ma become sharper and the predicted mantle structure at 0 Ma converges toward the tomographic image (Fig. 19D). With the increase of iteration number, the residual between the predicted and observed present mantle structure diminishes in magnitude and the initial pattern (A) transforms into a high frequency distribution (C). In addition, the root-mean-squared (RMS) residual with respect to the present day converges after five iterations (Fig. 19E), indicating that the adjoint algorithm is efficient for large scale convection modeling [Chapter 2].

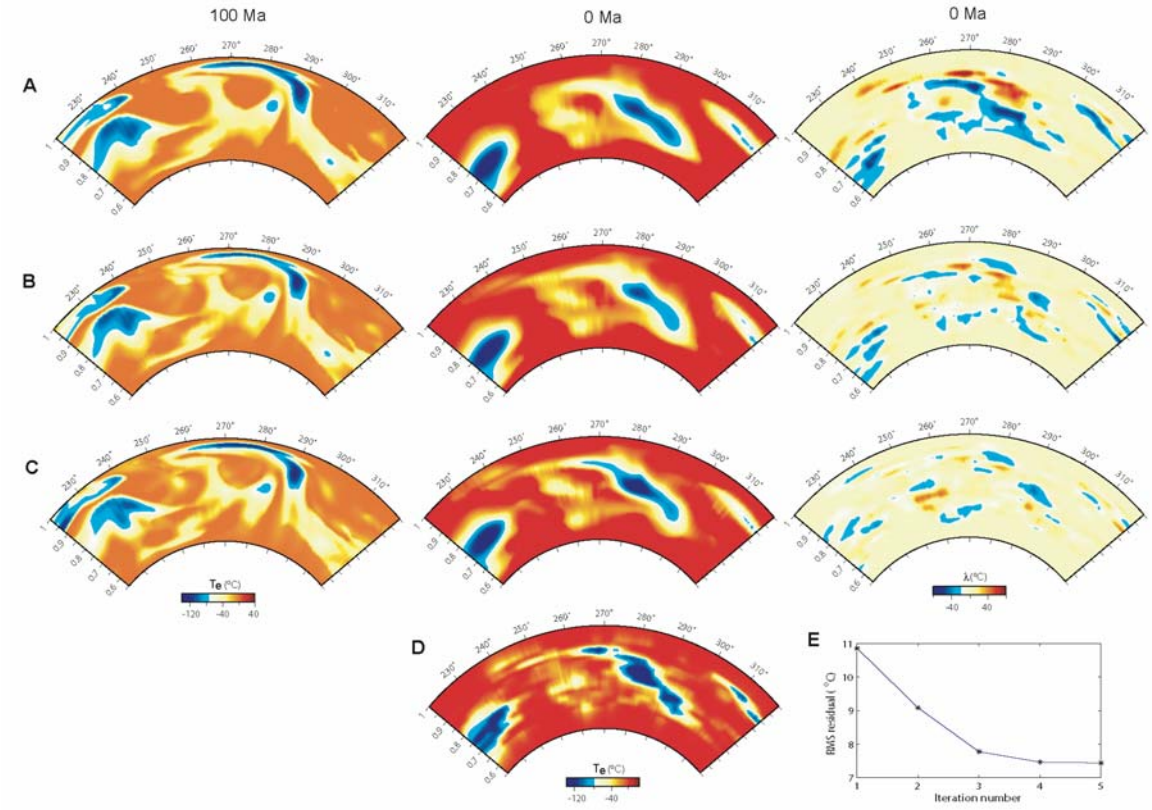

Figure 19 Convergence of the adjoint iterations. A–C corresponds to iteration number 1, 3, and 5, respectively, where the left column indicates initial conditions, the middle final conditions (predictions), and the right residual temperatures. D. Present-day mantle temperature field scaled from seismic tomography. E. Root-mean-squared (RMS) residuals as a function of iteration number.

We examined the influence of the parameterization of the stress guide [Figs. 17, 20B; viscosity of the two layers (η_{SL} and η_{WL}), its thickness (D_{SL} and D_{WL}), and length of the guide under the continent (L_{SG})] on model outcome. For comparison, an SBI run without the stress guide is shown (Fig. 20A). We find that the length of the guide beneath North America must be long enough to capture the Farallon anomaly as it rises into the upper mantle. Stress guides longer than 3000 km lead to similar results (Fig. 20C–E), all similar to Fig. 18. However, if the length is smaller, it fails to recover subduction (i.e., essentially leading to a result like that shown in Fig. 16).

On the other hand, as long as the two layers have a viscosity contrast of more than two orders of magnitude (Fig. 20G–H), we obtain overall results consistent with those shown in the paper. The stress guide leads to the same results when the viscosity contrast is larger, but starts to fail if the contrast is smaller (Fig. 20F). With a total thickness of the stress guide of 130 km ($=D_{WL}+D_{SL}$), the shape of the recovered slab is not sensitive to the relative thickness of the two layers inside the guide. Furthermore, we can show that the imposed plate motion and the stress guide neither increase nor decrease the vertical velocities in models with plate motions (Fig. 20A) or with both plate motions and the stress guide (Fig. 20J), compared to those without imposed plate motions (Fig. 20K). Overall, the result of subduction beneath North America is robust in that it can be reached with a wide

range of stress guide parameters and that the relevant dynamics and geophysical implications remain unchanged.

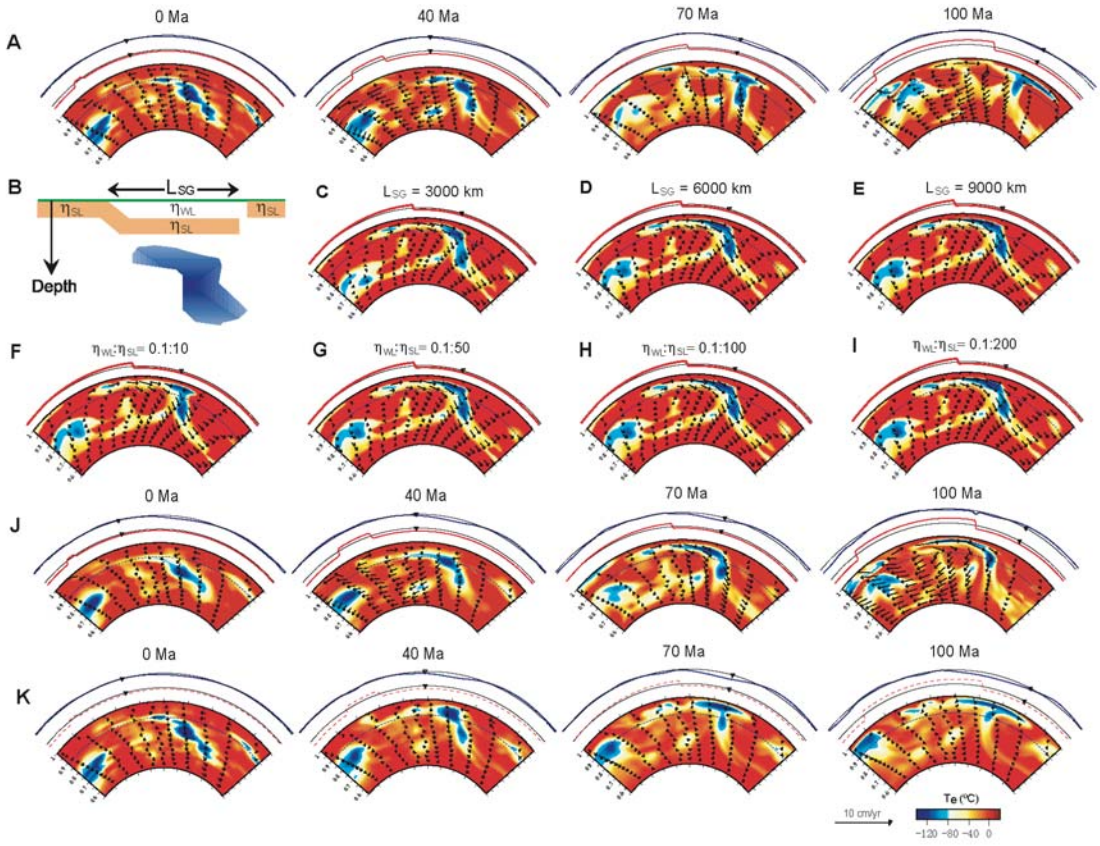

Figure 20 Subduction modeling with inverse method. All cross sections are at 41 °N, with the velocity vectors (black arrows) plotted over the temperature field (in color). Dynamic topography (blue) and plate motions (red) along the profile are shown above the cross-section. The black triangle denotes a borehole site (41.6 °N, 254 °E) that moves with the continent. All runs have a lower mantle viscosity h_{LM} = 15, h_{UM} = 1 and an effective temperature anomaly Te = 160 °C. (A) An SBI run with a standard model from present-day mantle structure leads to unrealistic subduction geometry back in time, indicating the requirement of a stress guide. (B) A sketch of the parameterized stress guide showing an imposed small viscosity (h_{WL}) layer overlying a large viscosity (h_{SL}) layer underneath the continent, where LSG indicates the length of the guide. The

recovered slab at 70 Ma (C−E) with the different values of L_{SG} and (F−I) with various viscosity ratios (relative to 10^{21} Pa s) within the two layers, showing the solutions converge as long as L_{SG} > 3000 km and h_{WL}: h_{WL}< 0.1:50. (J) The evolution of the slab after five forward-adjoint iterations including a stress guide with LSG = 6,000 km and h_{WL}: h_{WL} = 0.1:100, where reasonable subduction geometry develops. (K) A free convection test showing that without the imposed plate motions and stress guide, the slab has almost the same vertical velocities as can be seen from the depth of the structure at different times.

By inverting the Farallon slab subduction, we can also predict the dynamic topography on the surface as a function of time, which can constrain the uncertain mantle dynamic properties. In Chapter 3, we show how to constrain mantle properties by fitting the evolving dynamic topography recorded at one single site on the surface. In practice, we find that there are substantial constraints on the stratigraphy of WIS, including multiple boreholes with backstripped tectonic subsidence rates, several reconstructed paleo-shorelines marking the extents of the continental flooding at different geological times, and an isopach map showing the spatial variation of Cretaceous marine sediment thicknesses (Fig. 14). The extra power of constraints helps to reduce the amount of work involved in constraining mantle properties compare to the synthetic experiments in Chapter 3, as we demonstrate in the following subsections.

4.3.1 Effective Slab Temperature Anomaly

We attempt to put constraints on three model variables: upper mantle viscosity η_{UM}, lower mantle viscosity η_{LM}, and the effective temperature anomalies T_e scaled from seismic shear velocity perturbations.

Using a range of values for the effective temperature anomalies, we find that the recovered slabs have nearly identical geometries if the lower mantle viscosity is compensated so that the Rayleigh number remains invariant. In these cases, the convective velocities are nearly the same, except for small differences in the lateral variations in viscosity associated with temperature, so that the evolution of slabs remains the same for all cases (Fig. 21). Correspondingly, the predicted flooding has the same positions following the slab geometry and provides an opportunity for comparing the effects of different effective temperature anomalies on flooding.

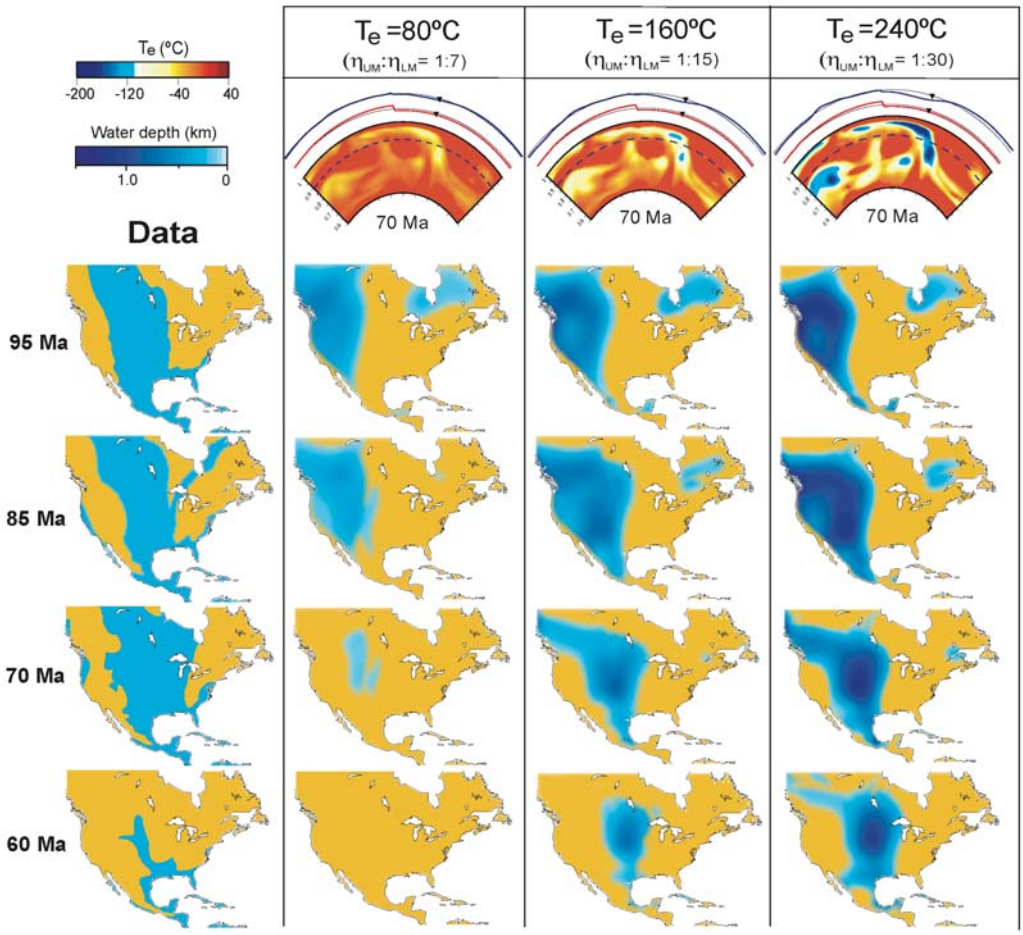

Figure 21 Constraining the effective temperature through flooding predictions. The left (column

1) shows the extents of Western Interior Seaway (WIS) from Late Cretaceous to early Tertiary, as reconstructed by Smith *et al*. [1994]. The right (columns 2–4) list the predicted WIS from three inverse models. These three models have different magnitudes of temperature anomaly (80, 160, and 240 °C, respectively) and lower mantle viscosities largely traded off with temperature (7×10^{21}, 15×10^{21}, and 30×10^{21} Pa s, respectively; all cases have an upper mantle viscosity of 10^{21} Pa s), where all three models produce the same slab geometries (the 70 Ma slab shown on top). The model with the 160 °C temperature anomaly matches observations the best.

On the other hand, although the dynamic topography has the same spatial pattern for cases with different effective temperature anomalies, the magnitudes of dynamic topography differ (Fig. 21). The extent of predicted flooding also varies depending on dynamic subsidence: With an effective temperature anomaly of 80 °C, the flooding occurs widely over the west at 95 Ma, but disappears soon after (Fig. 21); with a larger anomaly (240 °C), the flooding is well correlated with WIS, but persists after the Cretaceous; the flooding is well predicted with an anomaly of 160 °C in both time and space. This value of effective temperature anomaly will be used in subsequent models.

4.3.2 Lower Mantle Viscosity

For a given density, the timing and extent of the flat slab formation depend on mantle viscosity, especially lower mantle viscosity, because the slab has a longer path in the lower compared to the upper mantle. From experiments, we find that the upper mantle viscosity has a minor role in controlling the overall pattern of the WIS predictions. The surface dynamic topography associated with the descending slab causes the continent to

subside dynamically and results in marine deposition, if below sea level. In practice, we assume that the sedimentation rate was constant and we impose a eustatic curve while isostatically adjusting basin depth after each time step of 1 Myr. Therefore, the observed extent of Cretaceous flooding (Fig. 14), besides constraining slab density (i.e., T_e), also provides direct constraint on lower mantle viscosity for a fixed density anomaly. Fig. 22 demonstrates this process.

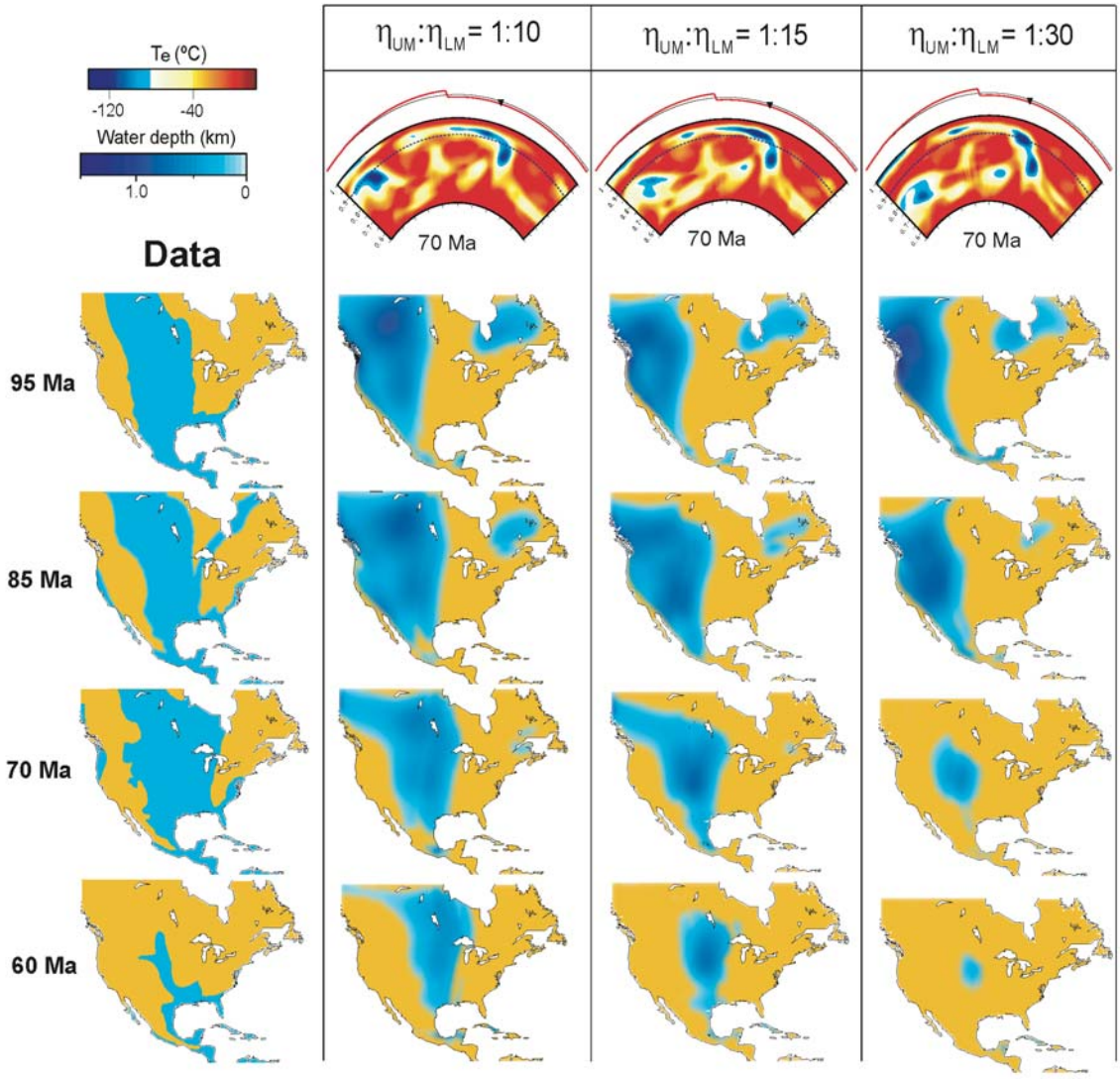

Figure 22 Constraining lower mantle viscosity through predicting the position and extent of WIS,

given a density anomaly. Column 1 shows the reconstructed WIS. Columns 2–4 show predicted flooding from three models with different lower mantle viscosities (10×10^{21}, 15×10^{21}, 30×10^{21} Pa s, respectively; T_e is the same as inferred from Figure 21).

As seen in Fig. 22, in a backward sense, a high viscosity (3×10^{22} Pa s) lower mantle causes the slab to rise slowly, reach the surface closer to the trench, and form a small area of flat slab subduction; the associated dynamic subsidence causes flooding with a smaller wavelength over shorter duration than observed (Fig. 22, column 4). Alternatively, a mantle of smaller viscosity causes the slab to rise faster and reach the surface farther from the trench, while forming a larger area of flat slab subduction, which causes extensive flooding spatially and temporally (Fig. 22, column 2). A good fit to observed flooding is obtained if we decrease the lower mantle viscosity to 1.5×10^{22} Pa s (Fig. 22, column 3).

Another viable means to retrieve lower mantle viscosity is to predict dynamic topography and its rate of change by comparing the fit to borehole tectonic subsidence curves and their temporal variation. For more details about this approach, please refer to Spasojevic *et al*. [2009].

4.3.3 Upper Mantle Viscosity

The rate of change of dynamic topography is inversely proportional to the upper mantle viscosity (Chapter 3). If we consider the vertical motions evident in WIS as proxy of absolute dynamic topography, and the backstripped tectonic borehole subsidence curves as rates of change of dynamic topography, we can infer the value of upper mantle viscosity by fitting the borehole subsidence rates as shown in Fig. 14.

There are 12 boreholes used in total, sampling the Cretaceous isopachs along east-west and north-south sections, which provide constraints on the upper mantle viscosity (Fig. 23A). If the upper mantle viscosity is too small, the slab sinks too fast, and the resulting subsidence rate is too large; as the upper mantle viscosity increases, the corresponding rate of change of subsidence decreases, and by best fitting these subsidence curves, we conclude that the upper mantle viscosity is about 1×10^{21} Pa s (Fig. 23B shows three such boreholes). On the other hand, a root-mean-squared (RMS) measure of the misfit from all boreholes may provide additional constraints. Fig. 23C plots these misfits along both the EW and NS lines, with the borehole listed as a function of distance from the west (north) end. Systematically, the misfits for the case with upper mantle viscosity of 1×10^{21} Pa s are the smallest among all experiments, validating the result from comparing the rates (Fig. 23B).

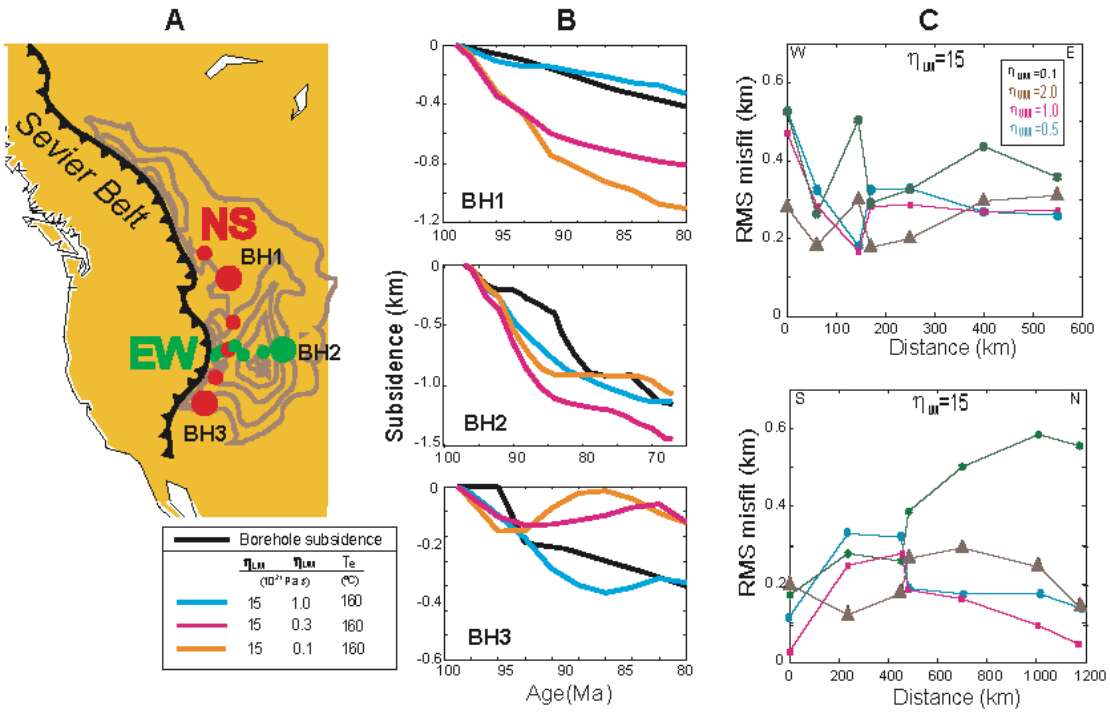

Figure 23 Constraining upper mantle viscosity with subsidence rates and RMS misfits. A. Site

locations of all boreholes (color dots) sampling the Cretaceous sediment isopach (brown contours), where three representative boreholes (big dots, i.e., BH1−3) are chosen to show the predicted subsidence rates. B. Observed (black) and predicted (color) dynamic subsidence rates at three borehole sites shown in A. Model parameters for these experiments are shown at the bottom of panel A. C. RMS misfits for all boreholes (triangles) along both the EW and NS sections.

We conclude this section by showing more models with different upper and lower mantle viscosities, in order to expand the parameter space explored (Fig. 24). As seen, the one with upper/lower mantle viscosity ratio of 1/15 is the best-fit model (Fig. 24B).

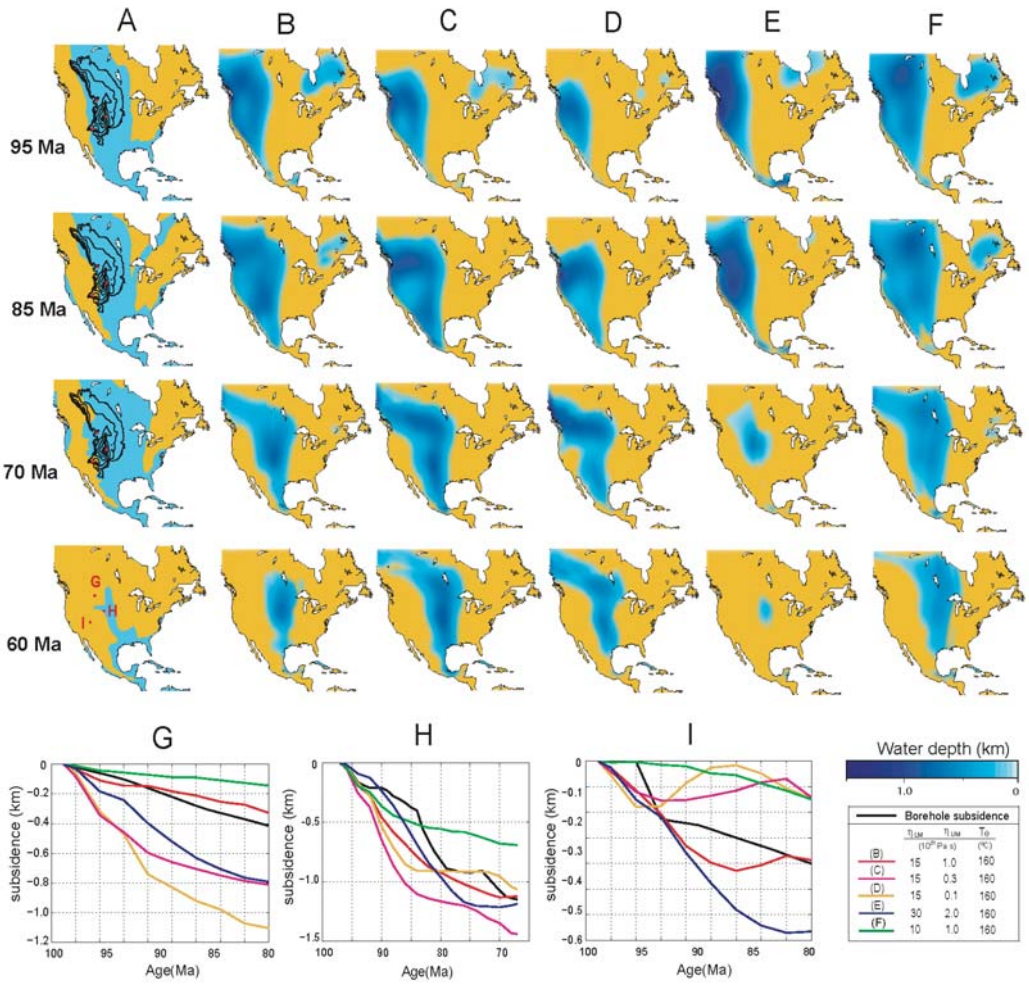

Figure 24 More models showing the effects of mantle viscosities on flooding predictions and borehole subsidence. (A) Observed flooding [Smith *et al*., 1994]. (B−F) Predicted flooding with different models (parameters are given in the bottom right corner; viscosities relative to10^{21} Pa s). (G−I) Borehole subsidence predictions (colored lines) compared to observations (black line).

4.3.4 Discussion

We attempted to constrain the uncertain mantle dynamic properties, including upper and lower mantle viscosities, and effective temperature anomalies associated with the subducting oceanic slabs. Our inferred mantle viscosities fall in the range of published values, including estimates from studies of postglacial rebound [Mitrovica and Forte, 1997; Milne *et al*., 2004; Paulson *et al*., 2007] and modeling the geoid [Richard and Hager, 1984; Hager, 1984] for the region of North America. The range of published values for the upper mantle viscosity (averaged if multiple layers were parameterized) is ~0.5-1×10^{21} Pa s, and that for the lower mantle is ~2-30×10^{21} Pa s. The upper/lower mantle viscosity ratio of 1:15 we infer falls within the middle of the earlier published values.

Conversion of a seismic-velocity anomaly recovered from tomography into a mantle density anomaly can be defined as a density/velocity ratio

$$R_{\rho/S} = \frac{\Delta\rho/\rho_0}{\Delta V_S/V_S} \tag{23}$$

where $\Delta\rho/\rho_0$ is the density perturbation, and $\Delta V_S/V_S$ is the shear wave velocity anomaly.

Earlier studies predicting geoid [Forte *et al*., 1994; Cadek and Fleitout, 1999] or plate

motions [Simons *et al*., 2007] suggest that this ratio ranges from 0.1 to 0.35. Our preferred density anomaly associated with the Farallon remnant slabs indicates a value of 0.35, at the top end of previous inferences. Our inference by fitting surface stratigraphy, however, is not directly comparable with other studies, because this ratio is constrained when the Farallon slab was at a much shallower depth than its present-day position, where the compressibility of mantle materials reduces this ratio as the slab sinks deeper. Given a density reduction factor of 2 from the flat slab stage during Late Cretaceous to its current mantle depth (~1400 km), the implied density/velocity ratio of ~0.2 is well within the range inferred by other studies.

Our inferred mantle properties are subject to change, and there are several reasons. First, the three-layer mantle viscosity structure is probably too simple to represent the earth, and the viscosity change from the upper to lower mantle may be gradual. But we are not confident that the current data assimilated in the inverse model can constrain a more sophisticated mantle rheology. Second, we assume a spatially uniform scaling from seismic velocity anomaly into density and this assumption may not be exact, as the response of different minerals to seismic properties and density varies. Existence of chemical heterogeneity inside the slab, for example an oceanic plateau, tends to respond differently to seismic wave speeds from the ambient slab. Third, as the resolving power of seismic tomography increases, the mantle image will evolve, which will certainly change the circulation pattern associated with these structures. Finally, omission of phase changes, both along the major seismic discontinuities and a possible basalt to eclogite transformation within the crust of the oceanic plate upon subduction, may trade off with the inferred

dynamic parameters of mantle. Specifically, phase changes at 410 and 660 km depths may increase and decrease, respectively, the velocity of the sinking slabs and, in some cases, trap slabs within the transition zone [e.g., Christensen, 1996; Cízkova *et al*. 2002]. Neglecting the phase transitions could have led to an overestimate of slab velocity, which in turn requires a larger lower mantle viscosity to counteract the buoyancy. This trade off, however, is likely to be a secondary effect, because the density anomalies associated with these phase transformations are minor compared to the total buoyancy of slabs, and the two phase changes have opposite Clapeyron slopes that will canceling each other if the subducting slab is strong enough [Billen, 2008]. The omission of the phase change of the crust by assuming a uniform density within the slabs, however, may affect the inferred temperature scaling from seismic velocity anomalies, especially in the presence of a possible oceanic plateau, as we will discuss more in the next chapter.

Another aspect of the inverse model that needs further improvement is to use more realistic rheology structure to replace the stress guide. In effect, the stress guide represents an enhanced version of temperature-dependent viscosity, plus a weakly coupled interface between the down-going slab and the overriding plate. With a better seismic image of the upper mantle structure beneath the western U.S., in which the younger part of the Farallon slab is better resolved and will presumably form a continuous subduction system, the stress guide may then be replaced by a strong slab with temperature-dependent viscosities. In this case, the continuity of the seismic image will provide a sustained mechanical coupling between the surface oceanic plate and the down-going slabs inside the mantle during active subduction.

On the other hand, the inverse model can be further validated by comparing with more independent observations, as will be one of the main themes of Chapter 5. With these new constraints, we can show that the inverse model we have developed fits a variety of observations, supporting its physical validity.

4.4 Flat Subduction of Farallon Plate during the Late Cretaceous

By predicting the formation of the Western Interior Seaway (WIS), while providing constraints on mantle dynamic properties, we recover the Farallon plate subduction back to the Late Cretaceous. Formation of this continental marine inundation is due to broad scale surface dynamic subsidence induced by the dense down-going oceanic slabs beneath North America (Figs. 21, 22, 24).

From structural geology and the history of magmatism [Coney and Reynolds, 1977; Henderson *et al*., 1984; Saleeby, 2003], it has long been postulated that a flat slab of the subducting Farallon plate lay beneath the western United States during the Late Cretaceous to early Cenozoic. This flat slab is thought to have occurred within a restricted area covering several states including Wyoming, Utah, Colorado, Arizona, and New Mexico. Our inverse models, by explicitly bringing the old Farallon remnant slabs back to the position where they subducted, provide complementary evidence for this flat-subduction episode.

At 100 Ma, the slab is shallow dipping, but not flat lying (Fig. 25A). Slab flattening starts at about 90 Ma progressively from the trench, and is characterized by a patch of thickened oceanic lithosphere about 1000 km wide, which subducts to the northeast (Fig. 25B). The model predicts that this segment of the Farallon slab evolved into an isolated and thickened patch of oceanic lithosphere bounded by a series of shallow to steep dipping fragments (Fig. 25D). This configuration is sustained throughout the Late Cretaceous, accompanying a vast inland migration of the whole slab. In the model, the flat lying slab sinks vertically from 70 Ma (Fig. 19). The inferred position of flat lying subduction from the adjoint model correlates with the region of basement cutting Laramide-type faults in the

western U.S. from 80 to 65 Ma [Saleeby, 2003]. Our best model matches the along-strike extent of the faulting and its maximum inboard extent (Fig. 25B–D). However, both the onset and demise of flat subduction occur 10 Myr earlier in the model compared to the structural and magmatic constraints. We made no attempt to tune model parameters based on the geologically inferred position of flat subduction.

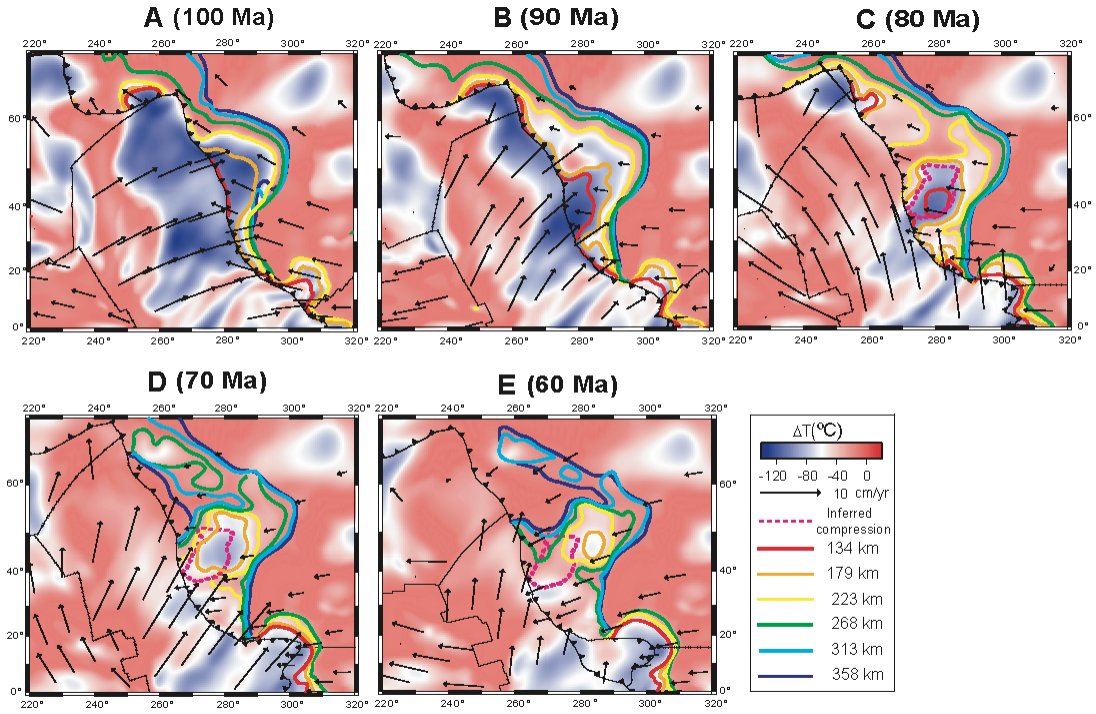

Figure 25 Map view of evolution of the Farallon subduction from the Late Cretaceous (A–D) to the Early Tertiary (E). The background temperature is at depth 223 km and velocity vectors indicate imposed plate motions. The color lines (isotherms for temperature 30 ºC lower than ambient mantle) indicate the upper boundary of the slab at different depths with a warm (cold) color representing a small (large) depth. The dashed pink contour outlines the geologically inferred surface compression area occurring between 80 and 65 Ma [Saleeby, 2003].

We want to point out that depths of these slab contours (isotherms in Fig. 25) make more sense in demonstrating the relative position of different parts of the slab than representing their absolute depths. Because the global model has a radial grid resolution of about 45 km, the inferred absolute depth of slabs is poorly resolved. In fact, these slabs seem to be too deep (almost all below 100 km), in terms of explaining the corresponding surface geology that may require shallower slab underplating, say, at ~50 km (more discussion in Chapter 5.2). Future models with higher numerical resolutions should consider producing more realistic radial positions of the flat slab.

By projecting the Farallon flat slab into the reference frame of North America, we can obtain a clearer picture for comparison between the flat slab evolution (Fig. 26) and various geological observations. On top of the slab contours, we plot the Colorado Plateau, a distinct geological unit that survived most of the tectonic deformations during Mesozoic and Cenozoic time [Burchfiel *et al*., 1992], and the geologically inferred Laramide province [Saleeby, 2003]. We also find that the rapid destruction and exhumation of the southernmost Sierra Nevada batholith [Saleeby *et al*., 2007] correlates with the passage of the flat slab in Southern California, both spatially and temporally.

Besides identifying the geologically inferred flat slab, we further find that this flat slab is not an isolated piece of oceanic plate, but rather that it is a thicker and shallower portion of a continuous slab that extends from Western Canada to Mexico (Fig. 25). The adjoint models suggest that a vast zone of shallow dipping subduction extended more than 1000 km eastward and northward from the zone of flat lying subduction, especially from 90 to 70 Ma (Fig. 25B–D). The zone is larger than inferred from a simplified set of forward

models that neither incorporated the details of subduction nor attempted to match stratigraphy [Bunge and Grand, 2000].

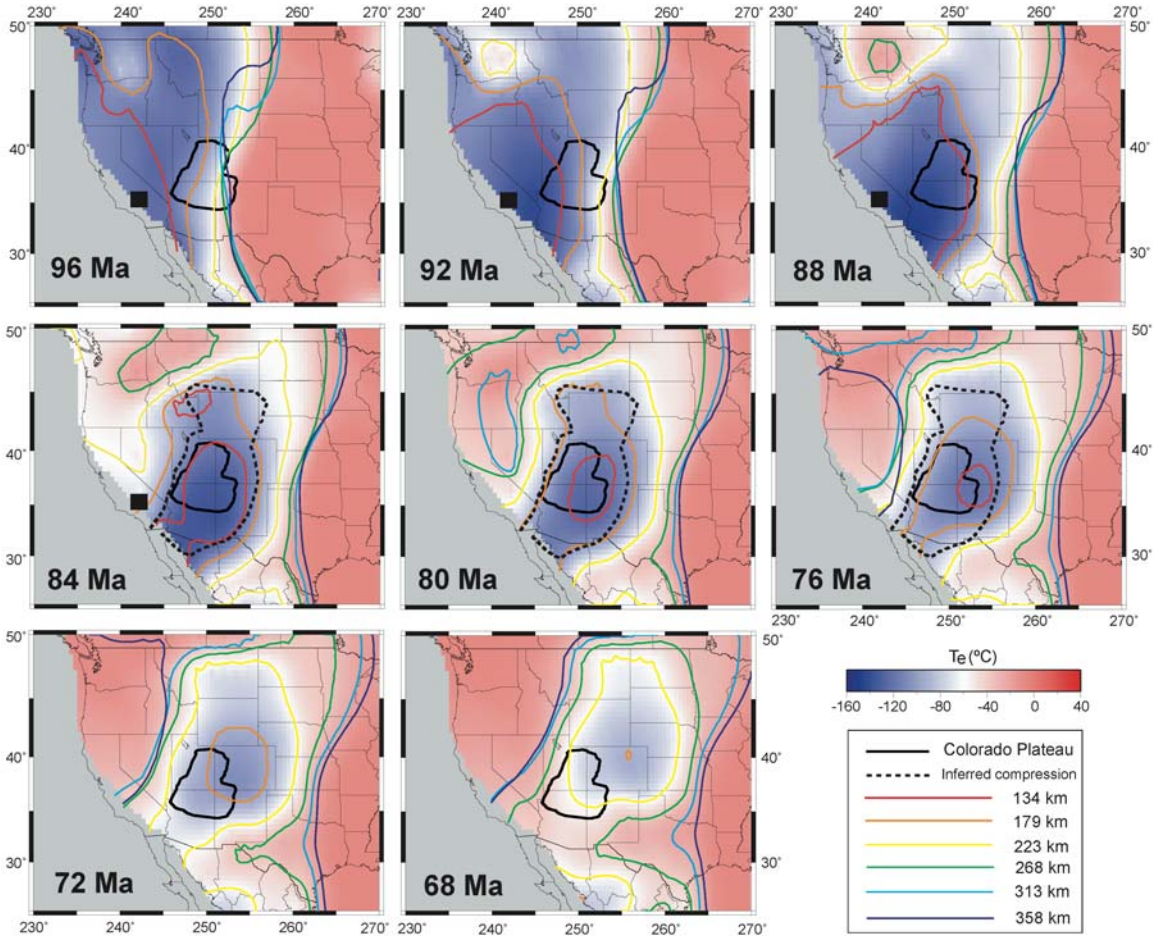

Figure 26 Three-dimensional delineation of the recovered Farallon slab during the Late Cretaceous from our preferred model in the reference frame of fixed North America: color contours depict an isotherm at various depths (these isotherms are 40°C lower than the ambient mantle that represent the edge of the Farallon slab at these depths); the background temperature field is shown for 223 km depth. All time snapshots are projected onto the North American plate. The black square in Southern California represents the location of southernmost Sierra Nevada batholiths during the exhumation event described by Saleeby *et al.* [2007]. The black dashed contour outlines the geologically inferred

Laramide compression zone [Saleeby, 2003].

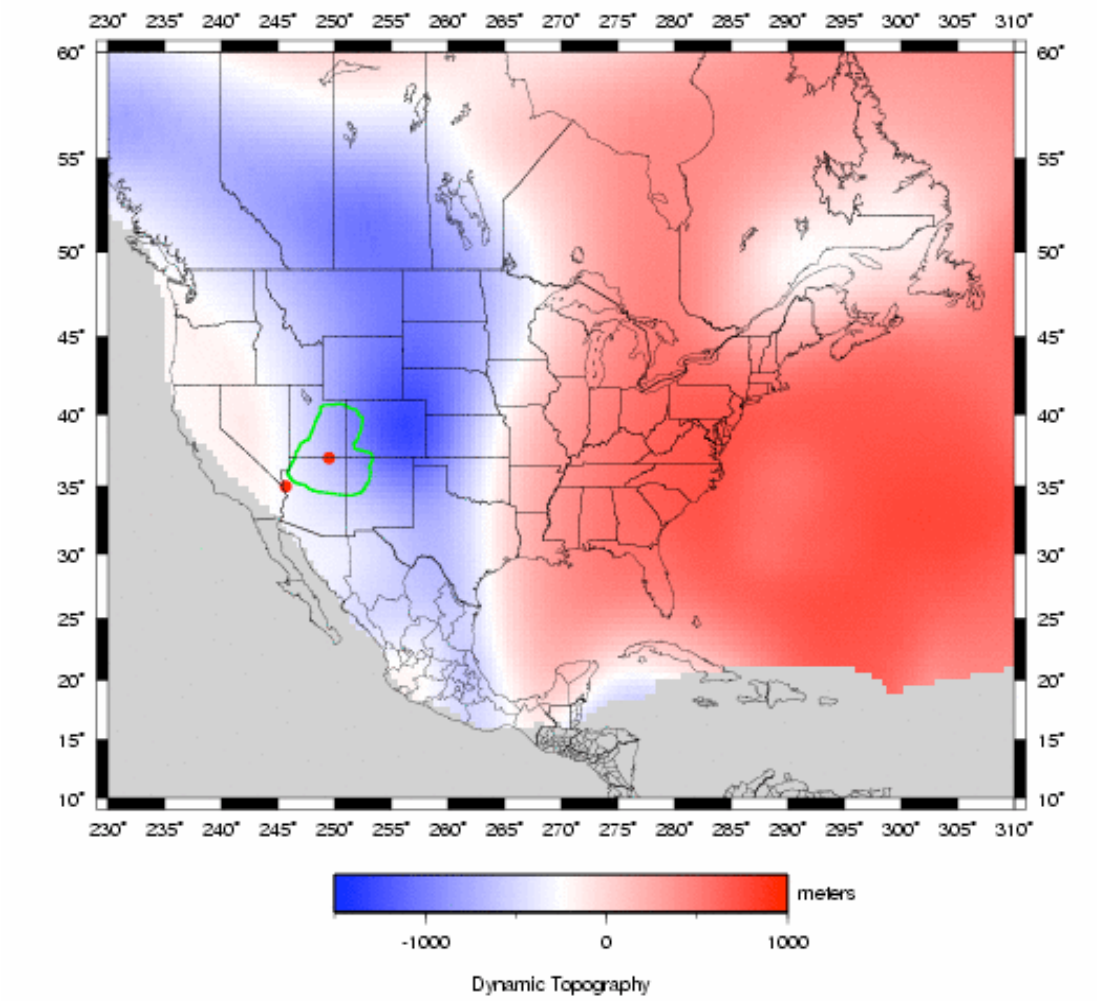

Figure 27 Predicted dynamic topography over North America at 70 Ma. Green contour represents the Colorado Plateau, and the two red dots span a profile along which Flowers *et al.* [2008] inferred for independent constraints for the topography evolution of the Colorado Plateau (more discussion in Chapter 5).

The broad shallow to flat subduction beneath North America caused surface subsidence across the entire western North America (Fig. 27). Therefore, the region of

dynamic subsidence for North America, previously thought to be confined to portions of the western U.S. [Mitrovica *et al.*, 1989; Burgess *et al.*, 1997], was likely substantially larger in extent and mostly characterized by a Cenozoic unconformity [Burgess *et al.*, 1997]. Much of the Canadian shield is sediment free, and the region has not been used to constrain dynamic models, but our model predicts this area also subsided during the Late Cretaceous, consistent with a recent low temperature thermochronology study for basement samples in western Canada indicating a history of sediment burial and unroofing occurred during the Cretaceous-Cenozoic time [Ault *et al.*, 2009]. This suggests that there is substantial ability to infer tectonic events when an adjoint of the convection problem is applied to seismic and plate motion data.

Upon inverting the Farallon subduction as described above, an immediate question to ask is what caused the flat subduction localized along the western U.S. during the Late Cretaceous? The adjoint inversion technique itself cannot be the answer. This is because the present-day seismic image, the starting point of the adjoint inversion, already has a "dome"-shaped structure in it located below the Great Lakes region (Fig. 28). This dome, when advected back to the surface, ultimately leads to the flat slab configuration (Fig. 25).

Specifically, we can track the three-dimensional evolution of the mantle structures in the inverse model (Figure 29). At present day, there is a prominent east-west anomaly (facing east; Figure 29I) occurring at ~1700 km depth, and another broader and obliquely dipping north-south anomaly (facing northwest; Figure 29E) at ~1400 km (cross sections of these structures show their dimensions). These two prominent anomalies form the hook structure well described in the literature [Ren *et al.*, 2007], while inside the 'elbow' is a dome shaped structure with its 'roof' going up toward the west. As these structures are

reversed backward in time (Figure 29B–D, F–H), the dome structure evolves into the flat lying patch of the Farallon slab while the hook structure evolves into the shallow dipping halo (from 100 Ma to 70 Ma) described in Figures 25, 26.

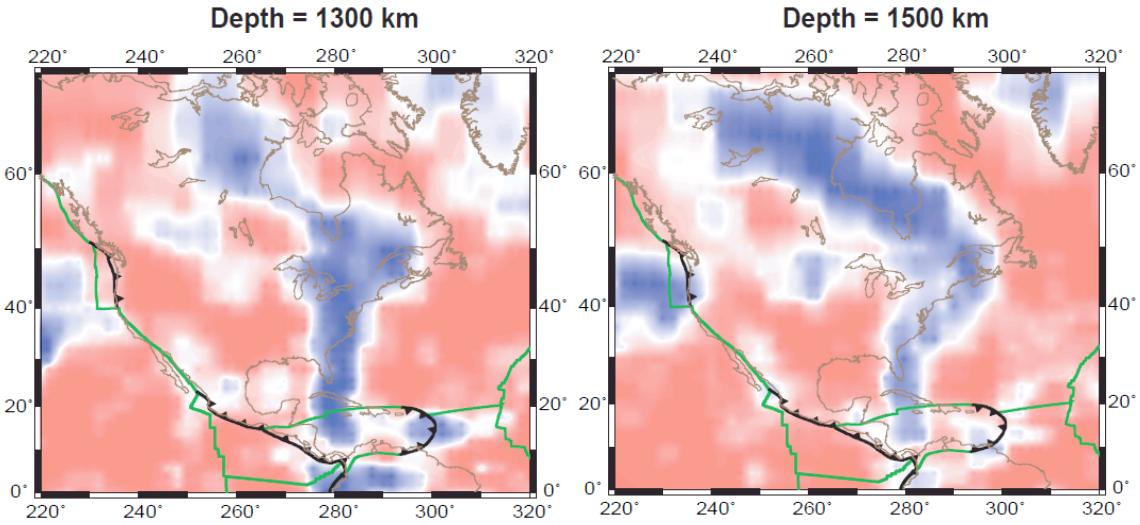

Figure 28 Map view at two different depths showing present-day Farallon remnant slabs in the lower mantle. Green lines represent spreading centers or transform faults, black tooth-line subduction zones, and dark brown, coastlines. Color scale is the same as that in Figure 26.

Since the restored flat-slab is a natural consequence of inverting the seismic image, more evidence, unrelated to seismic tomography, must be sought in order understand the physical mechanism causing the flat Farallon subduction. One possibility seems to be that the flat slab was created by usage of the stress guide implemented in the model. However, although the stress guide enhances the asymmetry of subduction, it does not explain the localized flat slab formation because the stress guide is uniformly, rather than locally, defined under the entire western North America. We will return to this issue in the next chapter.

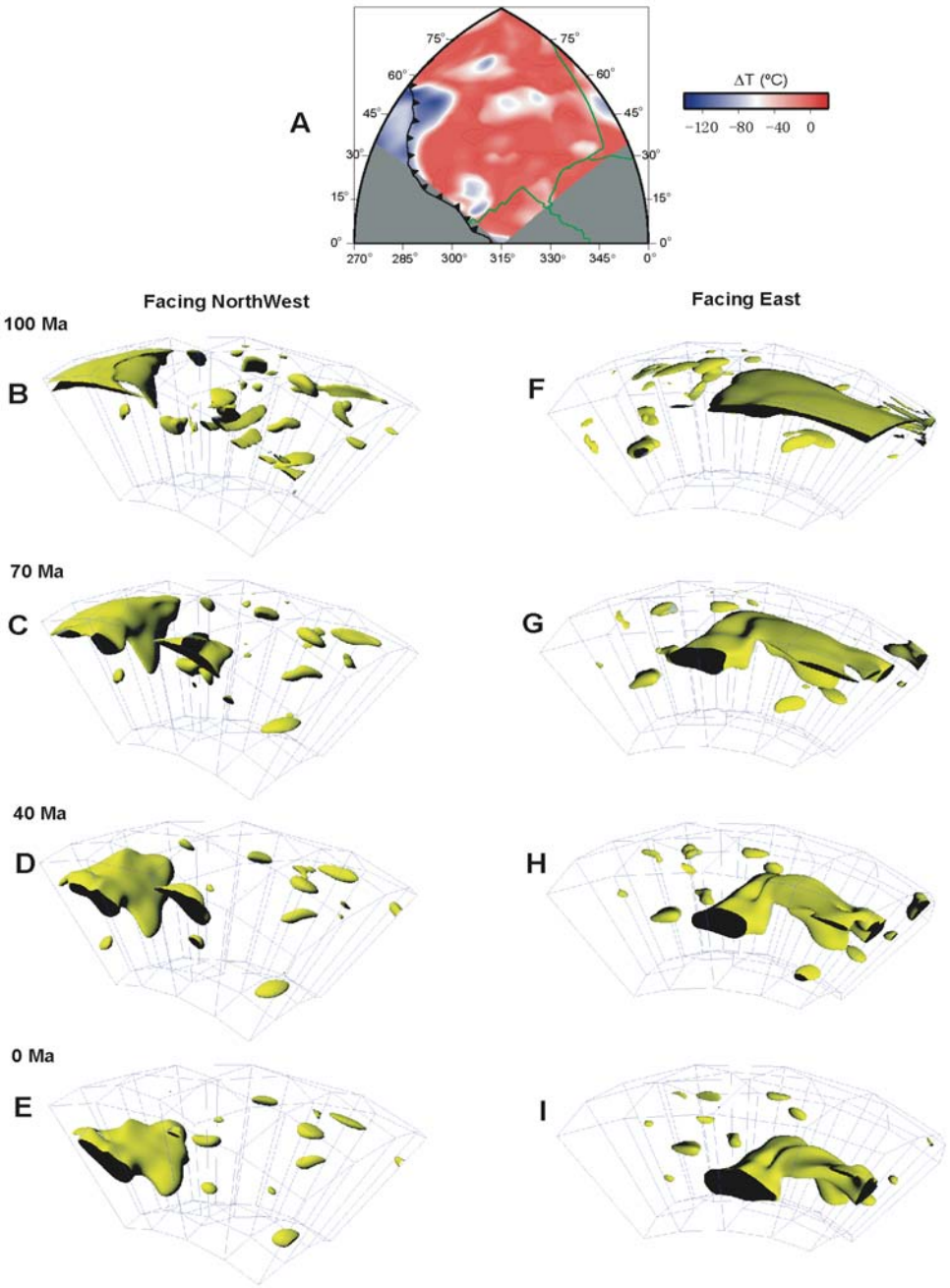

Figure 29 Three-dimensional view of the evolving Farallon slab in our preferred model, shown with isosurface of temperature field at 60 ºC lower than ambient mantle. This is a cut-out from a whole spherical shell (i.e., a Cap from *CitcomS* [Tan *et al.*, 2009]), where the top represents the surface and bottom the core-mantle boundary. The dynamics within the entire spherical domain was solved (12

caps), but only one cap is visualized here for clarity. The geographic location of the surface at 100 Ma is shown in A (the rectangular colored area), where the background temperature is at 223 km depth. The slab is viewed from two different angles, one facing the northwest (B–E) and the other toward the east (F–I), and four geological time periods are chosen from the initial time to the present day. The shaded green-yellow color represents the isosurface and dark area shows cross-sections of the slab against the edges of the cap.

Another possible reason for causing an isolated or segmented slab is the emergence of a spreading-center within the subducting plate. One candidate is the Kula-Farallon spreading ridge that formed during the Late Cretaceous time [Engebretson *et al*., 1986], which may have caused the northward translation of ‘suspect’ terranes along the western continental margin of North America [Debiche *et al*., 1987]. In fact, the plate motions we have used in driving the surface velocities of the inverse model include this phase of Farallon plate splitting [Fig. 25; Müller *et al*., 2008], but the splitting occurs later than the onset of flat slab subduction.

Chapter 5
Farallon Subduction Affecting North American Tectonics[4]

5.1 The Enigmatic Laramide Orogeny

With an inverse convection model, we recovered the Farallon plate subduction from its present-day mantle remnants, and we predicted the Western Interior Seaway (WIS) formation as due to dynamic subsidence associated with broad shallow to flat down-going slabs underneath North America during the Late Cretaceous (Chapter 4). Now we will move on to investigating another enigmatic tectonic feature, the Laramide orogeny.

The Laramide orogeny is an orogenic event occurring in the Late Cretaceous to Paleocene (80–55Ma), during which widespread thick-skinned Laramide block uplifts and the Rocky Mountain fold-and-thrust belt formed in the United States, which, in a broader

---

[4] This chapter is based on: 1) Liu, L., M. Gurnis, M. Seton, J. Saleeby, R.D. Müller & J. Jackson (2010), *The role of oceanic plateau subduction in the Laramide Orogeny,* Nature Geoscience, doi: 10.1038/NGEO829. ***Author contribution:*** L.L. and M.G. designed the whole workflow and carried out the inverse convection model, M.S. and R.D.M. carried out the plate reconstruction, J.S. worked on the geological interpretation and J.M.J. provided mineral physics analysis. All authors participated in preparing the paper. 2) Liu, L. and M. Gurnis (2010), *Dynamic subsidence and uplift of the Colorado Plateau,* Geology, doi:10.1130/G30624.1, in press. 3) Liu, S., D. Nummedal and L. Liu, *Tracking the Farallon plate migration through the Late Cretaceous Western U.S. Interior Basins,* Geology, in review. ***Author contribution:*** S.L. and D.N. backstripped the stratigraphy in WIS basins, L.L. provide the inverse convection model. All authors participate in writing the paper. 4) Spasojevic, S., L. Liu, M. Gurnis & R.D. Muller (2008), *The case for dynamic subsidence of the United States east coast over the Cenozoic*, Geophys. Res. Lett., 35, L08305, doi:10.1029/2008GL033511. ***Author contribution:*** S.S. analyzed the paleo-shoreline migration and sea level curves; L.L. performed the inverse convection model; M.G. supervised the whole workflow.

definition also includes the formation of the Canadian Rocky Mountains and the Sierra Madre Oriental fold-and-thrust belt in Mexico [English and Johnston, 2004, Fig. 30]. Compared to the North American Cordillera system, which sustained through the Jurassic and Early Cretaceous and represents thin-skinned deformations, the Laramide events are much more restricted in time and involve deformation of the entire basement over the western U.S. The extent of Laramide structures reaches a maximum 1500 km inboard (Fig. 30), much farther inland than a typical mountain belt along convergent plate boundaries [e.g., Saleeby, 2003]. Furthermore, the basement-involved deformations largely form a narrow "corridor" from Southern California toward Colorado and Wyoming [Saleeby, 2003].

Mechanisms for the Laramide Orogeny have been debated for decades, with little consensus reached at present [Burchfiel *et al*., 1992; DeCelles, 2004; English and Johnston 2004]. At least four different conceptual models have been proposed (Fig. 31). The "Retroarc Thrusting" mechanism proposed by Price [1981] attributed the inboard Laramide deformations to back-thrusting of the Cordillera onto the adjacent continental interior due to strong regional compressive stresses (Fig. 31A). An "Orogenic Float" tectonic model assumes a major through-going deep crustal basal detachment, which allows collision at plate boundary to be transmitted far inland (Fig. 31B). The "flat slab subduction" model argues that basal traction from the flat lying slab caused the basement-cored uplifts (Fig. 31C). A final model called "Cordilleran Transpressional Collision" assumes that much of

the Canadian Cordillera travelled thousands of km northwards, and this translation caused compressions over the western part of North America (Fig. 31D).

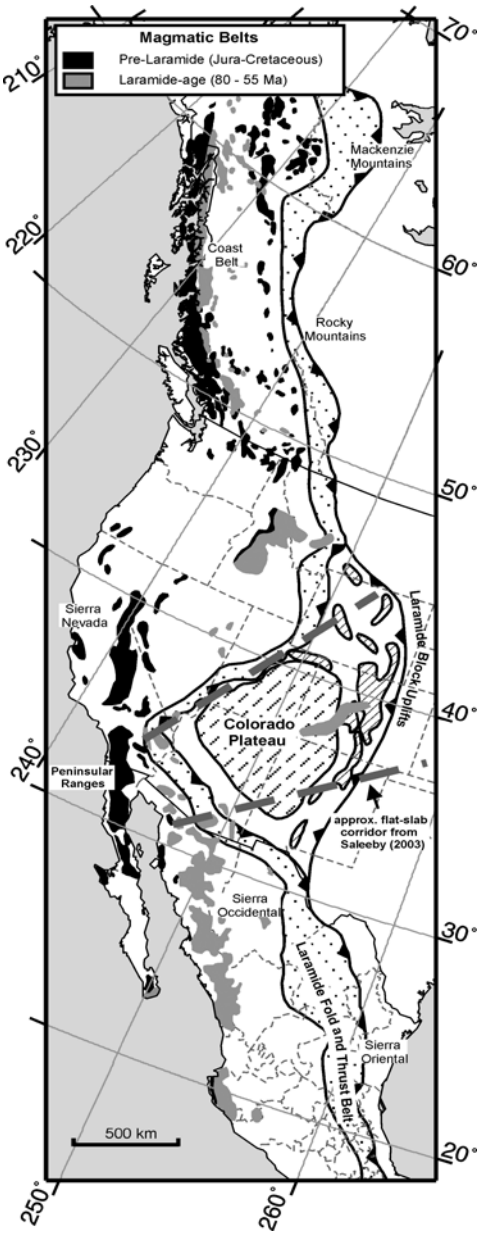

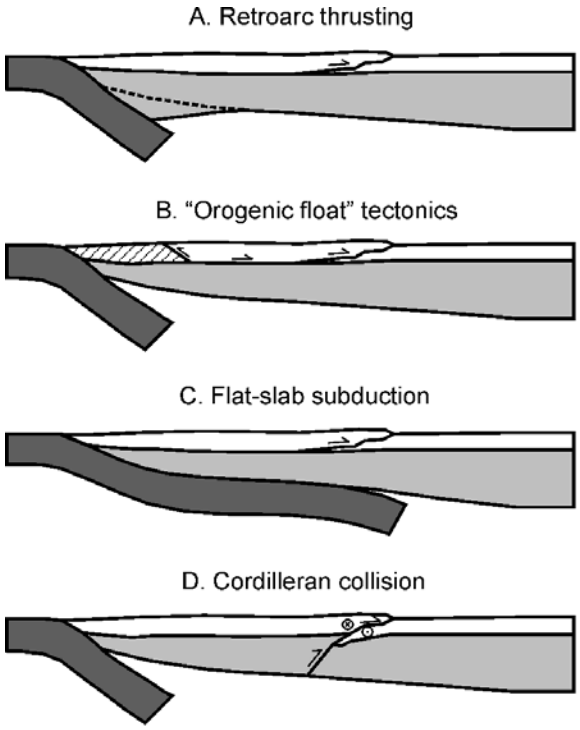

Figure 31 (From English and Johnston, 2004) A sketch diagram showing the various models proposed to explain the inboard deformation belt of the Laramide orogeny.

Figure 30 (From English and Johnston, 2004) Maps of pre-Laramide and Laramide magmatism, the extent of the Laramide thin-skinned fold-and-thrust belt and thick-skinned block uplifts, and the approximate location of the Laramide flat slab, according to Saleeby (2003).

A viable way to test a model is to check whether it can satisfactorily explain most features associated with the Laramide Orogeny. Among these conceptual models (Fig. 31), the flat slab subduction mechanism caused by subduction of either the Farallon-Kula ridge

[Henderson *et al.*, 1984] or a buoyant oceanic plateau [Livaccari *et al.*, 1981; Saleeby, 2003], seems the most promising [English and Johnston, 2004]. However, independent verification of these subduction models has remained elusive, because the putative ridge or plateaus are no longer on the surface. Previously, the plateau subduction model has been investigated through the reconstruction of synthetic conjugates to the plateaus in the western Pacific today [Livaccari *et al.*, 1981; Tarduno *et al.*, 1985], but these models differ substantially from each other depending on the underlying plate kinematic models, and the role of plateau subduction in driving Laramide deformation remains unclear.

The inverse model of mantle convection based on seismic tomography we have developed allows reconstruction of the history of subduction, providing a link between present-day mantle structures and geological observations (Chapter 4). This approach has the potential of recovering the now subducted former oceanic plateaus back to the surface directly from the observed present-day mantle seismic structures. Furthermore, since the plate motions involved in the calculation extend back to the time of interest, the larger uncertainties from earlier stages are avoided. The inverse calculation, therefore, offers a complementary approach to inferring the position of the oceanic plateau back in time. Here, we combine both forward (kinematic) and inverse (dynamic) approaches with geological observations from the overriding plate to test the hypothesis of plateau subduction.

5.2 The Role of Oceanic Plateau Subduction in the Laramide Orogeny

5.2.1 Detection of Oceanic Plateaus with Plate Reconstruction

We first use a recent plate reconstruction model to predict the positions of oceanic plateaus subducting beneath North America during the Late Cretaceous. The predicted positions of the Shatsky and Hess conjugates on the Farallon plate during the Late Cretaceous are shown in Fig. 32. The reconstructed Shatsky conjugate intersects the North American continent at ~90 Ma in southern California, and the Hess conjugate intersects the northern part of Mexico at ~70 Ma (Fig. 32A).

In the reconstruction, we assume that the Shatsky Rise formed at the Pacific-Farallon-Izanagi triple junction [Sager *et al*., 1988; Nakanishi *et al*., 1999] between ~145–130 Ma with conjugates on the Farallon and Izanagi plates. The Hess Rise and its conjugate formed along the Pacific-Farallon ridge at ~110 Ma. An ellipsoidal configuration is assumed for these conjectured plateaus, with contours representing estimated maxima and minima extent of the now subducted plateau conjugates. Positions of the conjugate plateaus are inferred based on the geometry of the preserved plateaus, the age of the underlying ocean lithosphere and the associated mid-ocean ridge system. The Pacific-Farallon ridge was reconstructed by deriving stage rotations from half-stage rotations with an assumption of spreading symmetry [Muller *et al*., 2008]. Reconstruction of the Pacific-Izanagi-Farallon triple junction additionally followed principles of triple junction closure [McKenzie and Morgan, 1969]. The absolute reference frame used for the Pacific plate is based on a hybrid moving Indian-Atlantic hot-spot [O'Neill *et al*.,

2005] and a fixed Pacific hotspot reference frame for times prior to 83.5 Ma [Wessel *et al*., 2006]. Although motion between hotspots in the Indian-Atlantic and Pacific domains has been recognized [Molnar & Atwater, 1973; Tarduno *et al*., 2003; Tarduno *et al*., 2009], moving Pacific hotspots have not been incorporated into our model as there are no published rotations available. Instead, we test two alternative fixed Pacific hotspot reference frames for times prior to 83.5 Ma [Wessel *et al*., 2006; Wessel & Kroenke, 2008] and find a difference of < 300 km between models at 90 Ma. We do not anticipate significantly more than 300 km of motion using a moving hotspot reference model over this 6.5 million year period (from 83.5–90 Ma) as this would require higher rates of motion of the Pacific plate for which there is no evidence.

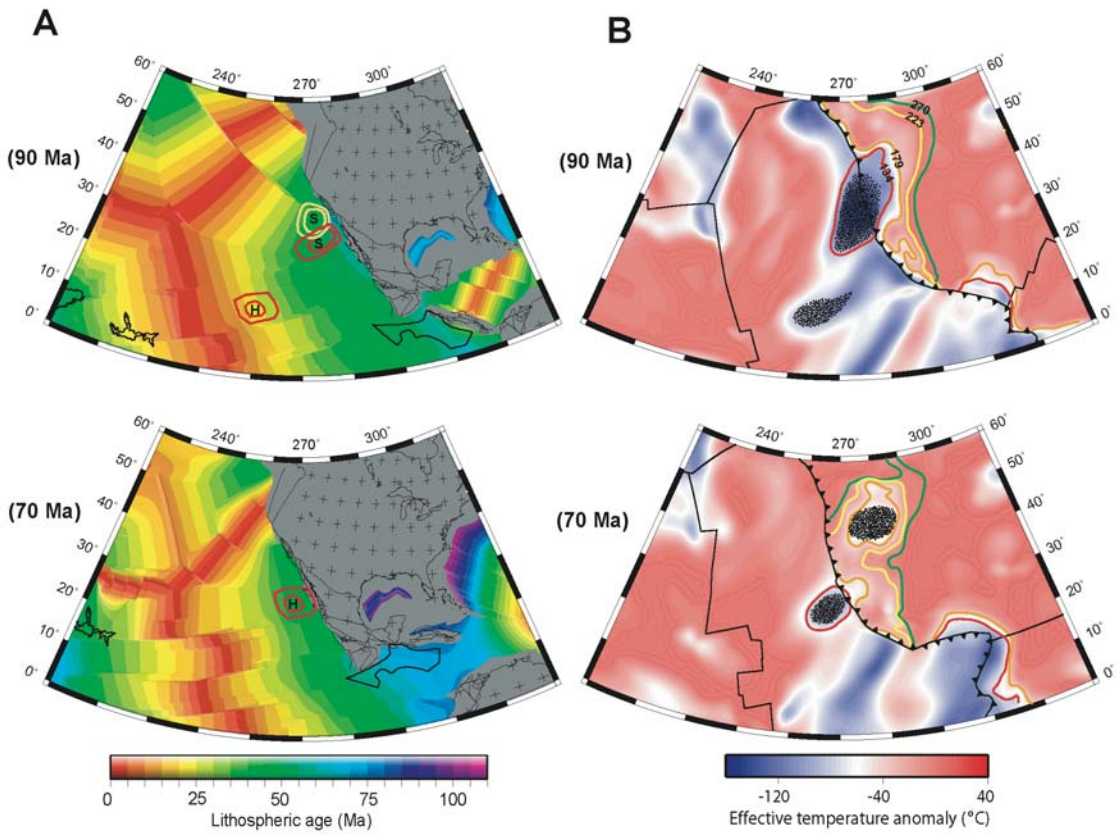

Figure 32 Predicted positions of the Shatsky and Hess conjugates in Late Cretaceous from (A) plate reconstruction and (B) inverse convection models. A. The Hess (H) and Shatsky (S) conjugate plateaus forming along the Pacific-Farallon (Farallon-Izanagi) ridges are denoted by red (yellow) contours; the contours represent their maximum/minimum extents while overlying the age of the sea floor [Muller *et al*., 2008]. Black outlines denote major presently preserved oceanic plateaus. B. Tracers delineate locations of the thickest part of the recovered lithosphere above 179 km depth from inverse convection models starting with seismic tomography, where the background effective temperature is color coded. Color contours show isotherms at different depths (labels in km) of effective temperature anomalies 40 °C lower than ambient mantle.

On the other hand, we perform an inverse calculation of mantle convection starting with a shear wave seismic tomography model [Grand, 2002]. The model that best fits stratigraphy over the western U.S. reveals an epoch of flat slab subduction characterized by a thicker-than-ambient oceanic lithosphere on the Farallon plate during the Late Cretaceous [Liu *et al*., 2008]. We highlight the thickest part of this segment of lithosphere with passive tracers in order to illustrate its location, and run the model forward from 100 Ma to the present. At 90 Ma, the thickened lithosphere is located largely to the west of the Farallon subduction zone while its northeast flank is subducted beneath North America initiating a segment of shallow flat subduction (Fig. 32B). The thickened lithosphere denoted by tracers falls in almost the same area as the kinematically predicted Shatsky conjugate, with both its orientation and geometry in the two models reasonably correlative (Fig. 32). At 70 Ma, the entire area of this thickened lithosphere shifts below the western U.S., while a second flat slab segment forms to the south correlative with the predicted position of the Hess conjugate (Fig. 32A,B).

Since the plate reconstruction approach starts with positions of the extant Shatsky and Hess plateaus while the inverse convection approach utilizes the seismic structures of the present-day mantle, the two approaches are independent, although they share the same plate reconstruction from 90 Ma to the present. Both temporal and spatial consistencies of these now subducted plateaus from the two approaches suggest that these features existed on the Farallon plate during the Cretaceous. Identification of these oceanic plateaus allows a quantitative assessment of their relation to the sequence of geological events over western U.S., especially those of the Laramide Orogeny.

5.2.2 Mechanisms for the Laramide Orogney

Traditionally, plateau subduction is thought to cause synchronous crustal uplift. Therefore, earlier models attributed the Laramide Orogeny to subduction of conjugates of either the Hess [Livaccari *et al.*, 1981] or Shatsky Rise [Tarduno *et al.*, 1985] between roughly 70–60 Ma, the time of classic Laramide exhumation [DeCelles, 2004]. However, we find that this relationship is only true along the continental margin where the plateaus initially entered the subduction zone. Initial subduction of the Shatsky conjugate beneath southern California in both up-to-date plate reconstructions and inverse convection models (Fig. 32) correspond to fore-arc destruction, intra-arc ductile thrusting and rapid exhumation of the southern Sierra Nevada batholith (SNB) during 96-86 Ma[12] (Fig. 26, Fig. 33). Continuing subduction of the Shatsky conjugate progressively disrupted the southern California active margin producing the distinctive southern California batholith (SCB) segment (Fig. 33), characterized by severe tectonic erosion of the fore-arc and

frontal arc, shearing off of the mantle wedge and lower crust, and shallow-level underplating of trench sediments [Saleeby, 2003; Ducea *et al.*, 2009]. Crustal structure of the SCB is currently dominated by the effects of large magnitude Late Cretaceous extension that followed immediately the passage of Shatsky conjugate [Saleeby, 2003], marked in Figure 33 by the much broader SCB than the SNB and the Peninsular Ranges batholith (PRB).

Proximal to the SCB segment both the SNB and PRB segments experienced Late Cretaceous intra-arc ductile thrusting, and parallel forearc unconformities, presumably in response to the subduction of the flanks of the Shatsky conjugate [George and Dokka, 1994; Nadin and Saleeby, 2008]. Large volume magmatism of both the SNB and SCB ceased at ca. 85 Ma, while diffuse supra-subduction magmatism migrated hundreds of kilometers inland [Burchfiel *et al.*, 1992]. The PRB segment of the active margin responded to Hess conjugate subduction, commencing at ca. 65 Ma (Fig. 33), in a more subdued fashion than the SCB response to Shatsky conjugate subduction. The PRB underwent rapid erosional denudation as arc magmatism migrated abruptly inland to Sierra Madre Occidental [Ferrari *et al.*, 2007], and crustal shortening intensified along the Mexican foreland thrust belt, which is considered to be the southward continuation of the Laramide orogeny [Campa, 1985]. A plausible explanation for the differences in intensities of Shatsky and Hess conjugate damage zones is a notable difference in their masses (Fig. 32).

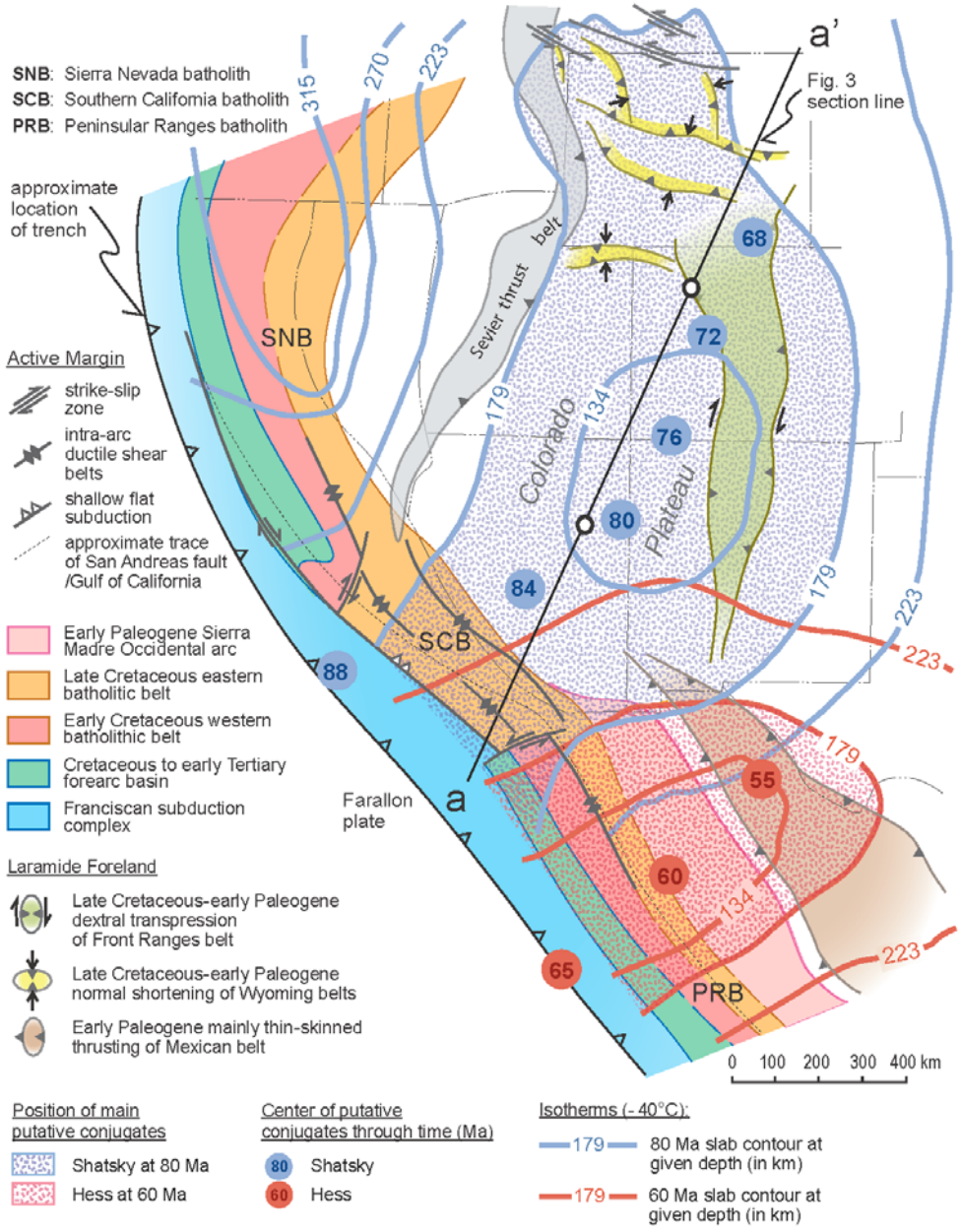

Figure 33 Palinspastic map showing SW Cordilleran active margin and Laramide foreland for end of Cretaceous time with temperature field overlain. Contours (same as Fig. 30; light blue for 80 Ma, red for 60 Ma) and predicted positions of the putative Shatsky and Hess conjugate plateaus (inside the 179 km contour) are from the inverse model. Filled circles represent the volumetric

center of the putative Shatsky (light blue) and Hess (red) conjugate plateaus at given age during their subduction beneath North America. Line a-a' indicates the surface trace of cross-sections shown in Figure 34.

Flat subduction of the Shatsky conjugate during the Late Cretaceous appears to have caused the shortening and faulting inside the classic Laramide province, which flanks the northern and eastern margins of the Colorado Plateau (CP) (Fig. 33). The classic Laramide is distinguished from the Jurassic-Cretaceous thin-skinned Sevier thrust belt by the intimate involvement of cratonic basement and a more restricted timing of Late Cretaceous–early Paleogene [Burchfiel *et al*., 1992]. Our reconstruction places the center of the Shatsky conjugate moving in a northeast arcuate path beneath the CP region between 84 and 68 Ma (Fig. 33). Both the NE trajectory and northward tapering of the plateau thickness correlate with Late Cretaceous–early Paleogene dextral transpression along the Front Ranges belt that transfers northwards into normal shortening across the Wyoming belts [Karlstrom and Daniel, 1993] and sinistral shear to the north [Burchfiel *et al*., 1992] (Fig. 33). While localization of deformation along the Front Ranges and northern Wyoming was facilitated by reactivation of ancient basement structures [Burchfiel *et al*., 1992], shortening in between seems mainly due to NE subcrustal thrusting of the Shatsky conjugate. Sevier belt deformation during the NE motion of Shatsky conjugate along its foreland entailed the final phases of thrusting [DeCelles, 2004] transitioning into the initiation of regional extensional tectonism [Druschke *et al*., 2009]. The migration of the western edge of the Shatsky conjugate along the Sevier belt

(Fig. 33) implies a distinct mechanism for classic Laramide deformation, relative to that of the Sevier belt.

In contrast to earlier plate reconstructions [Livaccari *et al.*, 1981; Tarduno *et al.*, 1985], our analysis predicts the continuation of Late Cretaceous marine conditions across much of the Laramide province. This is the time when the WIS occupied most of the western and central North America (Fig. 14), as is well documented in isopach maps distributed over the Colorado Plateau and areas to its north and east, called the Great Plains [e.g., Bond, 1976; DeCelles, 2004]. Even in regions to the south of the Colorado Plateau, where little Cretaceous marine sediment has been preserved probably due to erosion, a recent low temperature thermochronology study based on apatite (U-Th)/He inferred that the southern Plateau and surrounding area must have been buried by at least 1.5 km thick of sediment during the Late Cretaceous [Flowers *et al.*, 2008]. According to our study, such widespread marine sedimentation is due to long-wavelength dynamic subsidence associated with the flat slab underlying these areas (Fig. 34A, B). Collectively, our study suggests that initial subduction of the plateau should have caused the slab to flatten because of the extra buoyancy associated with its thick crust, but continuing flattening would mostly result from the increased plate coupling with a possibly weakened mantle wedge [Manea and Gurnis, 2007]. As the Shatsky conjugate translated beneath the Colorado Plateau region (Fig. 33), the oceanic crust is deep enough to undergo the basalt-eclogite phase transformation, during which the plateau loses its positive buoyancy [Ringwood and Green, 1966]. Both the overall negative slab density anomaly and enhanced plate coupling during shallow subduction drag the surface downward (Fig. 34A). This phase change is not

incorporated in the inverse model, and should be addressed in future research simulating the flattening process of a slab due to subduction of an oceanic plateau.

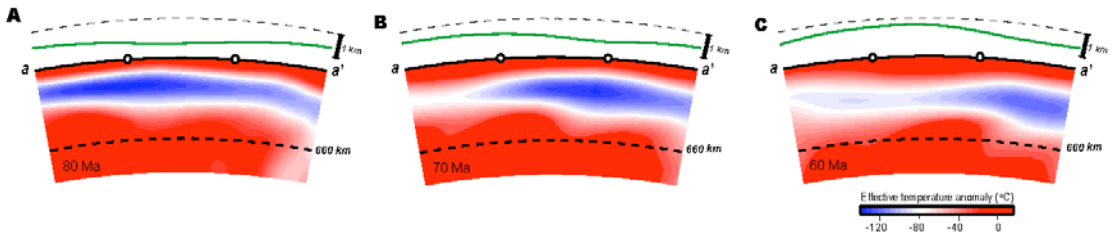

Figure 34 Configuration of the subducting Farallon flat slab and the corresponding surface dynamic topography along profile a-a' (shown in Fig. 33). Three representative times (A–C) during Late Cretaceous to Early Paleocene are chosen. The dynamic topography is shown with green lines.

A present-day analogy to this situation (e.g., shown in Fig. 34A) is the subducting Inca plateau in Peru [Guscher *et al.*, 1999], where broad surface subsidence is observed above the flat slab outlined by seismicity (Fig. 35). In a recent seismic tomography model [Li *et al.*, 2008], the putative Inca plateau shows up as a prominent P wave anomaly whose geometry and location correlate well with the flat portion of the subducting oceanic slab, and with a surface topography low. The similarity between the still subducting Inca plateau and the reconstructed Shatsky conjugate plateau further strengthens our argument that an oceanic plateau, once migrated inland, will cause surface subsidence instead of uplift.

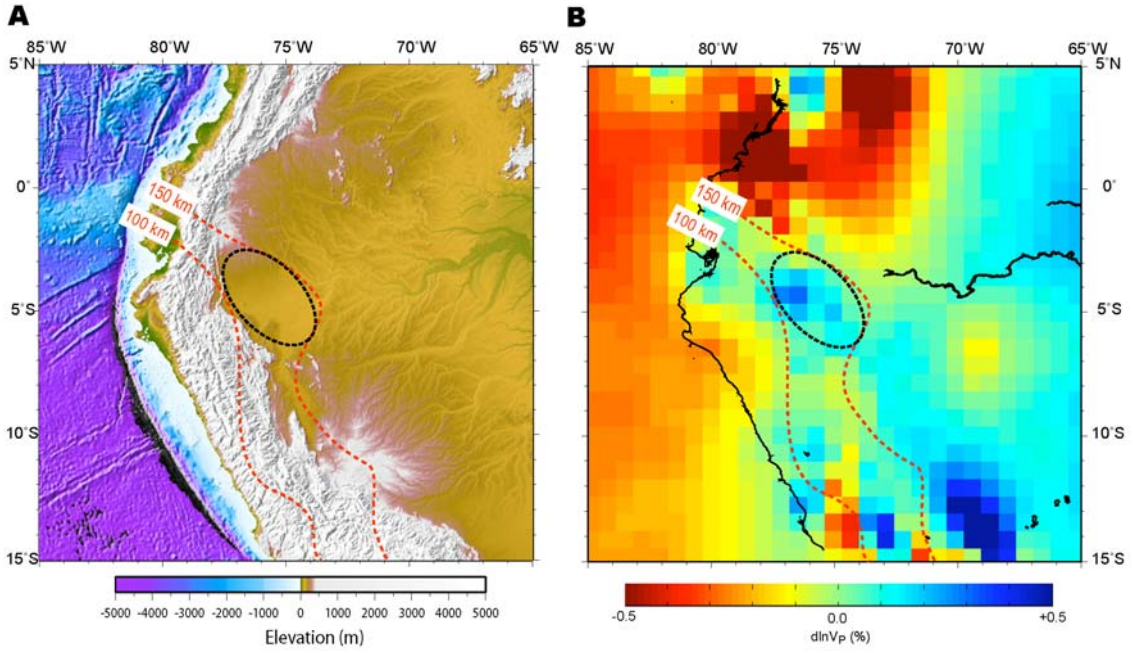

Figure 35 Surface topography (A) and seismic tomography [Li *et al.*, 2008] at 120 km depth (B) of western South America. The dashed red lines indicate slab contours [Guscher *et al.*, 1999] at 100 and 150 km depth, respectively. The dashed black ellipse represents the putative Inca plateau subducting beneath Peru [Guscher *et al.*, 1999]. Note the topography low (presumably subsidence) above the Inca plateau, which shows up as a fast seismic anomaly in B. Both surface subsidence and flat slab formation associated with the subducting Inca plateau makes it a present-day analogy of our model where subduction of the Shatsky conjugate plateau caused the slab to flatten while simultaneously inducing surface subsidence above the plateau during the Late Cretaceous.

Furthermore, our study suggests a mechanism for the Laramide uplift that is different from earlier thoughts. We find that Laramide uplifts at local scales should have initiated along thrust faults [DeCelles, 2004], when the flat slab underplated the Laramide province (Fig. 33). Although not modelled explicitly, this process should reflect relative topography/relief changes in response to crustal thickening and brittle failure subject to

strong basal traction and compression exerted by the plunging oceanic plateau. Subsequent regional scale uplifts, however, are associated with removal of the plateau from beneath the Laramide province. The flat slab associated with the Shatsky conjugate gradually sank deeper into the mantle as it migrated to the northeast. Both horizontal removal of flat slab from beneath the CP region after 80 Ma and the overall diminishing negative dynamic topography associated with cold slabs (Fig. 34B, C) led the surface to rebound in a SW to NE trend with a maximum of ~600 meters uplift occurring during the Latest Cretaceous over the CP (Fig. 34). This corresponds to regional uplifts starting as early as 80 Ma and peaking at 70–60 Ma across the Laramide province, and the overall eastward migration of marine conditions from the Sevier foredeep region to regions further into the continental interior [DeCelles, 2004].

The exact history and amounts of the uplift has been another widely debated issue. Our model predicts that the Laramide province experienced two stages of uplift, with an accumulative uplift by Eocene of about 1.2 km, consistent with the inferred kilometer-scale rock uplift over the southern CP [Flowers *et al*., 2008]. In Section 5.3, I will discuss the uplift history over the Colorado Plateau region in more detail. Removal of the Shatsky conjugate by its sinking north-eastward into the mantle may have further facilitated fault reactivation causing distributed basement uplifts intervened by the Laramide foredeep basins [Burchfiel *et al*., 1992; DeCelles, 2004], although we do not yet understand the details of the process. Our study may explain the 20 Myr time lag between the Late Cretaceous (~80 Ma) shortening deformations and Early Paleocene (~60 Ma) cooling events of the Laramide Orogeny [DeCelles, 2004].

5.2.3 Present-day Position of the Subducted Plateaus

Can a subducting oceanic plate always penetrate into the lower mantle, and where does the crustal material end up after subduction? It is generally accepted now that whole-mantle convection dominates although some slabs still get stagnated at the upper-lower mantle interface [Fukao *et al.*, 1992; Li *et al.*, 2008]. Mineral physics calculation suggests that the crustal material should also get subducted into the lower mantle accompanying the downgoing oceanic slab [Hirose *et al.*, 1999]. Direct image of lower mantle remnant crusts, however, has not been obtained, leaving many aspects of their elastic and dynamic properties unknown. Therefore, locating and verifying the existence of the foundered oceanic plateaus (with thick crusts) inside the present-day mantle will be of significance to several fields of earth sciences, including seismology, geodynamics, and mineral physics.

If our arguments about oceanic plateau subduction are reasonable, the geodynamic model we construct can predict the locations and geometries of the deeply subducted plateau conjugates in the present-day mantle via tracers (Fig. 36). By tracing the two oceanic plateaus to the present day, we find that both conjugates are now situated under the east coast of the U.S., with the Shatsky conjugate to the east of the Great Lakes and the Hess conjugate to the south. The Shatsky conjugate is predicted to extend from 900 to 1400 km in depth, covering ~1000 km in the north-south direction and ~500 km east-west; the Hess conjugate essentially stays above 1000 km depth with ~500 km cross-sectional dimensions (Fig. 36). In a recent high-resolution P wave seismic inversion [Li *et al.*, 2008], very similar configurations of the Farallon remnant structures are observed, compared to those in the S wave tomography (Fig. 13), reinforcing the interpreted

positions of these oceanic plateau conjugates. We emphasize that the tracers outlines the possible location ranges of these sank plateaus, and the smearing effect of global tomography inversions tend to blur/average the signature of these plateaus during the seismic imaging process.

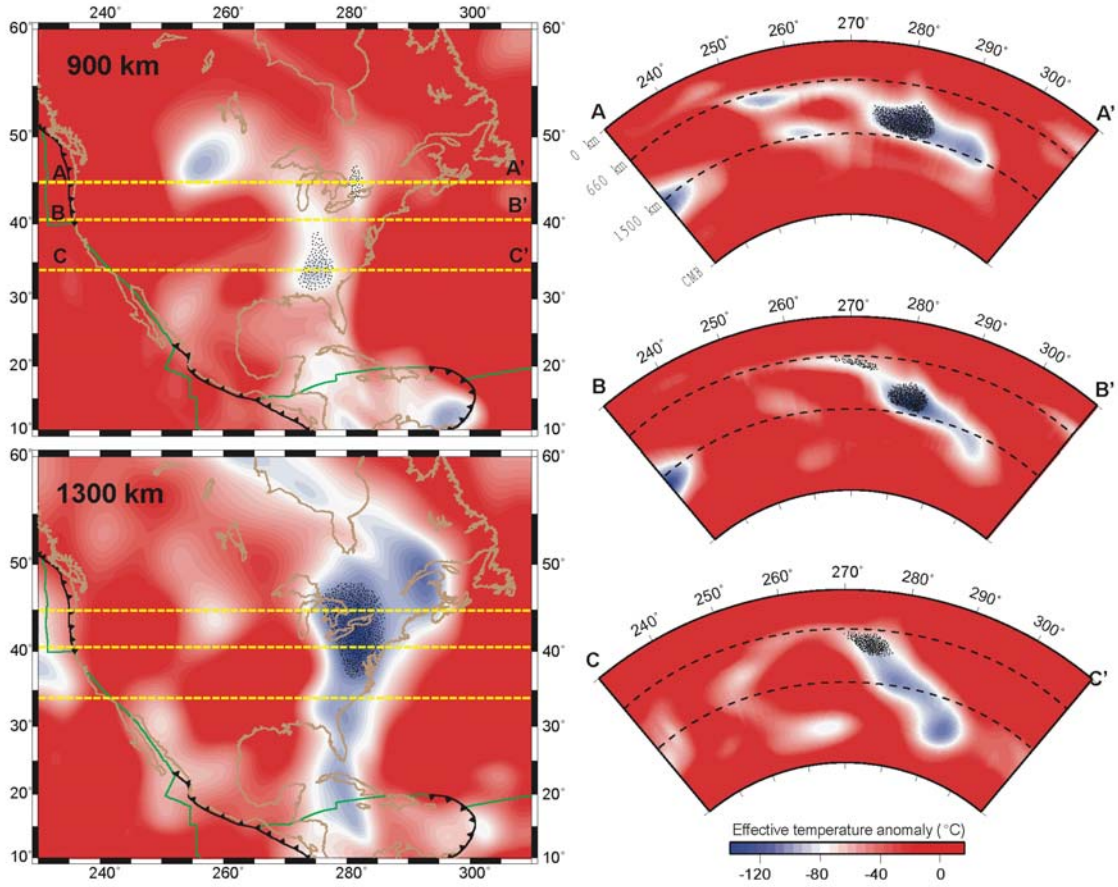

Figure 36 Location and geometry of the Shatsky and Hess conjugate plateaus inside present-day mantle. Map view at two different depths (900 and 1300 km) and cross-sectional view at three latitudes (45°, 41° and 33° North) are shown. Tracers highlight the predicted locations and distributions of these plateaus. The Shatsky conjugate is to the east of the Great Lakes and the Hess conjugate is to the south.

Stishovite-structured silica, one of the main proposed constituents of deeply subducted mid-ocean-ridge basalt (MORB) [Hirose *et al*., 1999], has seismic velocities ~20% higher than the ambient mantle after the post-stishovite phase transition (P_{tr}) [Carpenter *et al*., 2000]. In MORB, incorporation of a few wt. % Al_2O_3 and H_2O into silica is favorable [Hirose *et al*., 1999; Lakshtanov *et al*., 2007] and decreases the depth of post-stishovite P_{tr} to ~800 km [Lakshtanov *et al*., 2007]. Although effects of temperature on the wave speeds of post-stishovite are unknown, an estimated decrease by <4% in the lower mantle is reasonable [Cammarano *et al*., 2003]. Therefore, ~25% of hydrous aluminous post-stishovite in deep MORB crust would cause seismic velocity anomalies >4%, where current tomography models are blurry. Because of the substantially thicker-than-ambient crust accreted during formation of an oceanic plateau and expected slab thickening upon entrance into the lower mantle, present remnants of the Shatsky and Hess conjugates could have an accumulated crustal pile thickness of >50 km. The predicted strong seismic anomalies in conjunction with the large volumes should make these foundered crustal blocks detectable as sharp seismic features, in which travel time anomalies and waveform multi-pathing are expected [Sun *et al*., 2009]. The ongoing seismic experiment with the USArray shifting to the east coast of U.S. should provide the opportunity to detect these subducted oceanic plateau conjugates.

5.3 Dynamic Subsidence and Uplift of the Colorado Plateau

5.3.1 Background

The Colorado Plateau is a distinct geologic province in the southwestern United States bounded by the Basin and Range province to the west and the Rio Grande Rift on the east (Fig. 37A). Unlike surrounding areas, which have undergone significant orogenic and extensional deformations since the Paleozoic, the plateau has survived these tectonic events with little internal deformation [Burchfiel *et al*., 1992]. The widespread shallow marine deposition over the Colorado Plateau suggests that this area was below sea level in the Late Cretaceous [Bond, 1976], while the present elevation of the plateau is ~2 km. This change of elevation requires the Plateau to have risen by about 2 km during the time in between.

Both timing and mechanics of Colorado Plateau uplift to its present elevation, however, have remained uncertain. Paleo-botanical studies indicate that the central Rocky Mountains region surrounding the plateau reached their present elevation in the Eocene [Wolfe *et al*., 1998]. Interpretation of basalt vesicularity based on late Cenozoic volcanic rocks along the plateau margins suggests that most of the elevation gain might have occurred in the Miocene [Sahagian *et al.*, 2002]. However, a recent exhumation study based on apatite (U-Th)/He thermochronology pushes the age of Colorado Plateau uplift back to the latest Cretaceous, with a kilometer-scale elevation gain over the southwestern part of the plateau [Flowers *et al.*, 2008; Fig. 34A]. Even though the Plateau is a distinct physiographic unit today [e.g., Spencer, 1996], whether it uplifted as an individual block,

or as part of a broader-scale, synchronous uplift of western United States has been debated [Burchfiel *et al*., 1992; Wolfe *et al*., 1998; Flowers *et al*., 2008].

Various models have been proposed to explain the vertical motion, including crustal thickening [Bird, 1988; McQuarrie and Chase, 2000], removal of mantle lithosphere [England and Houseman, 1988; Spencer, 1996], chemical alteration of the lithosphere [Humphreys *et al*., 2003; Roy *et al*., 2004], and active mantle upwellings [Parsons *et al*., 1994; Moucha *et al*., 2009]. In this chapter, we use mantle convection models to investigate the vertical motion on the plateau associated with Farallon plate subduction.

5.3.2 Subsidence and Uplift of CP due to Farallon Subduction

We calculate the dynamically supported topography due to sub-surface vertical stresses originating from convective flows in the mantle through inverse models. These models, based on the adjoint method, attempted to retrieve past mantle structures by predicting present mantle seismic images through a set of forward and backward calculations (Chapter 3). The adjoint method, with seismic tomography, plate motions, and stratigraphy, has allowed us to better constrain geodynamic processes in the geological past [Liu *et al*., 2008; Spasojevic *et al*., 2009]. By being calibrated with vertical motion proxies beyond the Colorado Plateau (e.g., the WIS formation), the models provide a means to explore the vertical evolution of the plateau since the Late Cretaceous. The resolution of the models (50 km horizontally) is sufficient to predict dynamic topography over the scale of the Colorado Plateau.

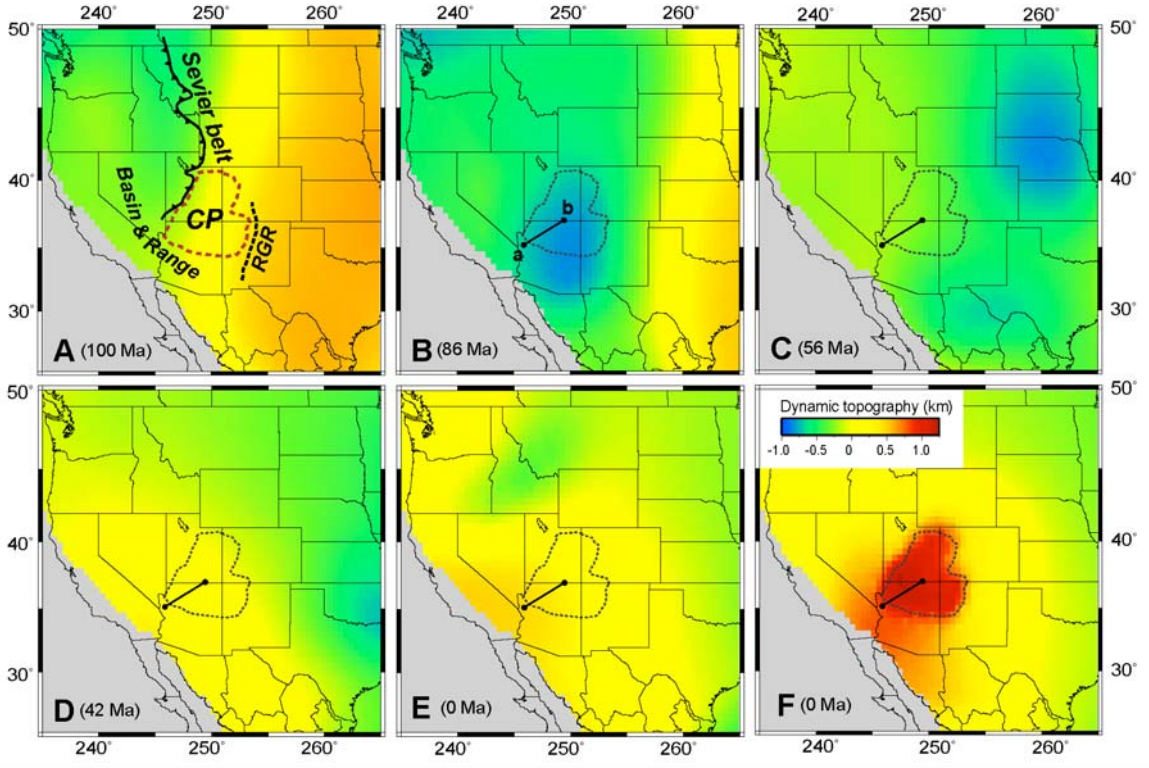

Figure 37 Predicted dynamic topography over the western United States for five different geological times (A–E) based on model M2 (see Table 4), and that for present-day (F) based on M4. Line a-b is the study profile of Flowers *et al*. (2008), same as in Figure 2. Tectonic features (A) are shown for their present-day location (CP - Colorado Plateau; RGR - Rio Grande Rift).

As described in Chapter 4, the inverse dynamic models with three model parameters (upper and lower mantle viscosities and the scaling of seismic variations to temperature associated with the Farallon slab) are constrained by prediction of the Late Cretaceous continental-scale WIS and rates of tectonic subsidence extracted from distributed boreholes [Liu *et al*., 2008; Spasojevic *et al*., 2009]. Our preferred model has only slabs from the Farallon subduction and provides a best fit to both the Western Interior seaway and tectonic subsidence rates (M2 in Table 4). For comparison, we present two

other slab models that fit these constraints less well. One model (M1) has a larger lower mantle viscosity than the preferred model; this model predicted the tectonic subsidence well but had too little marine inundation in the seaway. In another model (M3) we use a larger temperature anomaly and a larger lower mantle viscosity; this model over predicted flooding and its rate of change (through tectonic subsidence rates). Based on parameters from the preferred model for the Farallon slab, we further include the upwelling from the putative buoyant anomaly below the Colorado Plateau (M4).

In order to compare with earlier vertical motion studies, we focus on the southwestern part of the plateau, for which Flowers *et al*. [2008] completed a careful study of exhumation history. The rate of change of dynamic topography from the preferred model, within the Grand Canyon vicinity, is shown in Figure 38A, along with inferences on vertical motion from Flowers *et al*. [2008] and Huntington *et al*. [2010]. The predicted temporal evolution of dynamic topography at several locations along the profile of Flowers *et al*. [2008] is shown in Figure 38B. Map views of dynamic topography over the western United States including the entire Colorado Plateau are shown for five representative times: mid-Cretaceous (100 Ma), Late Cretaceous (86 Ma), Late Paleocene (56 Ma), Middle Eocene (42 Ma), and the present-day (Fig. 37), corresponding to inflexions between subsidence and uplift from the preferred model of dynamic topography (Fig. 38B).

At 100 Ma, before the flat slab stage initiated under the western U.S., the plateau was close to sea level (Figs. 37A and 38). As the Farallon slab moved inland (Fig. 39), the plateau subsided due to the viscous stresses associated with the downgoing slab. The subsidence was sufficiently rapid that by 86 Ma, when the flat slab underplated the

Colorado Plateau (Fig. 39), the entire plateau subsided below sea level with a maximum subsidence at its center (Fig. 37B). As the flat slab migrated to the northeast and sank into the mantle in latest Cretaceous (Figs. 39 and 40), the surface of the plateau began to rebound, causing the first stage of uplift due to the diminishing downward force from the slab (Fig. 37C).

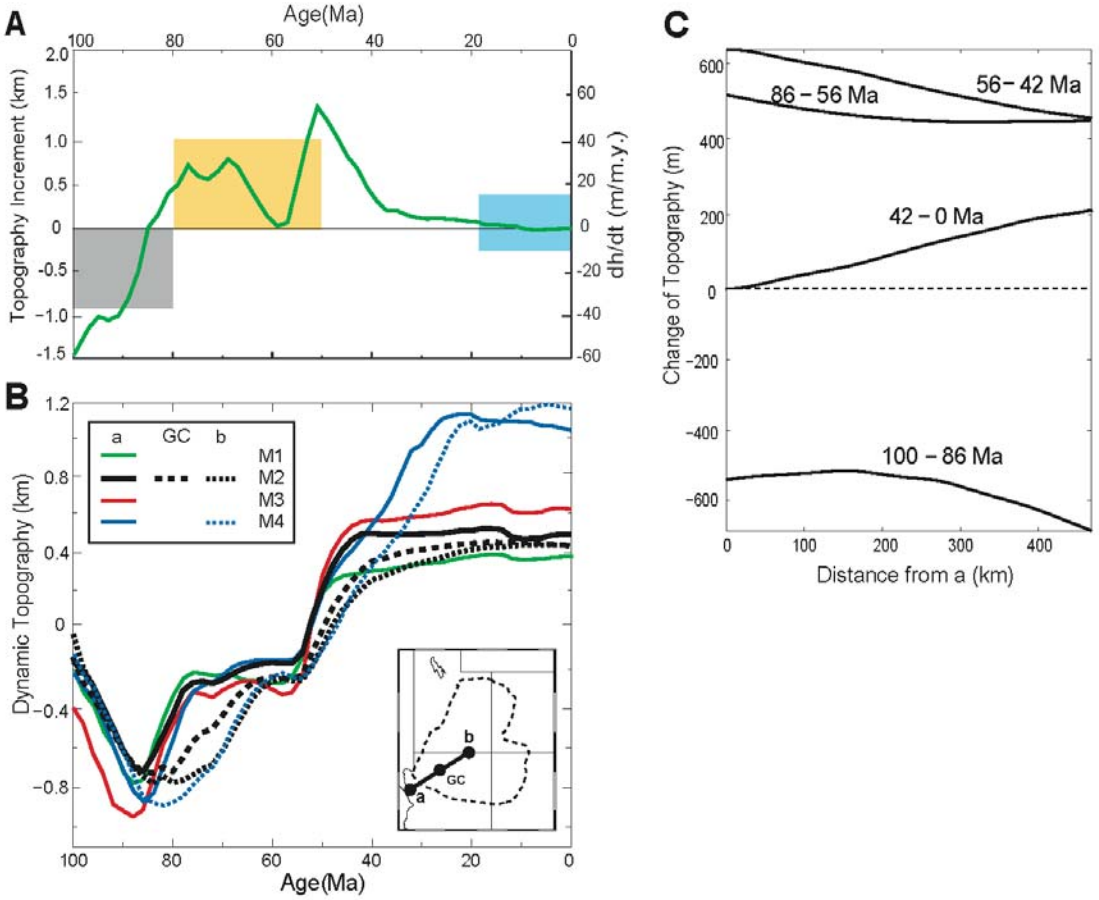

Figure 38 Topographic evolution of the southwest corner of the Colorado Plateau. A: Dynamic subsidence (gray box, isostatically corrected from sediment thickness) and uplift (yellow box) of the southwestern plateau (axis on the left), inferred by Flowers *et al.* [2008]; blue band represents little elevation change inferred by Huntington *et al.* [2010]. Green solid line represents rate of change of

dynamic topography (axis on the right) at the middle of profile (GC - Grand Canyon, in inset map in panel B) from model M2. B: Predicted dynamic topographies since 100 Ma at multiple points along profile (a, GC, and b) based on four different models listed in Table 4. Models M1−M3 show similar trends at all points, so only point a is shown for these models. Addition of positive buoyancy (M4) shows a distinct trend after 40 Ma from other models. C: Changes of dynamic topography during four time intervals along the profile a–b (inset in B) for model M2. These differential topographies illustrate both absolute elevation change and tilting of plateau at different times.

Table 4. Parameters of Models Predicting the CP Dynamic Topography

Model name	η_{UM}	η_{LM}	T_e (◦C)	Active upwelling included?
M1	1.0	30	160	No
M2	1.0	15	160	No
M3	1.0	30	240	No
M4	1.0	15	160	Yes

Note: η_{UM} (η_{LM}) — upper (lower) mantle viscosity, with a reference viscosity 10^{21} Pa s

T_e — effective temperature anomaly

From 56 to 42 Ma, the CP underwent the second stage of uplift (Figs. 37D and 38B) with an instantaneous rate as high as ~60 m/m.y. (Fig. 38A). This fast uplift was caused by removal of the younger part of the Farallon slab from southwest to northeast beneath the plateau, the returning asthenosphere pushing the surface upward (Fig. 40). By 40 Ma, almost the entire slab was removed from beneath the southwest plateau (Fig. 39), and most of the plateau was subject to positive dynamic topography, with the southwest side higher than the northeast (Fig. 37D). From 42 Ma to the present, the southwest margin of the plateau is predicted to have been stable with little vertical motion, while the plateau

interior was uplifted ~200 meters further until the present (Figs. 37E and 38C). The high topography over the plateau since the Eocene in the slab models (M1–M3) was caused by upward return flows generated by the subduction to the north and east of the plateau (Fig. 49).

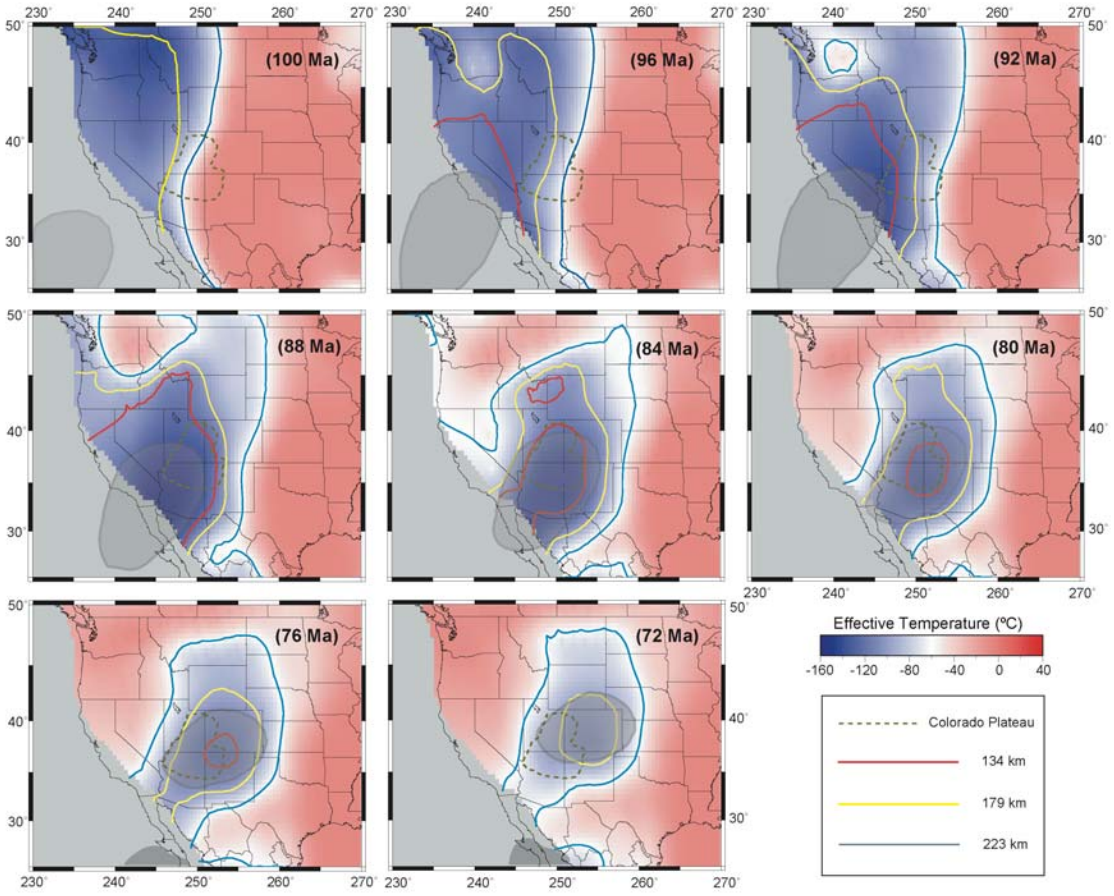

Figure 39 Migration of the Farallon flat slab, surrounding the Shatsky conjugate plateau, with respect to the North American continent during the Late Cretaceous based on the inverse convection model of Liu *et al.* [2008]. The background shows temperature at 220 km depth, while color contours denotes isotherms of temperatures 60 °C lower than the ambient mantle at different depths. The gray area (tracer distribution) indicates the thickest part (core) of the

Shatsky conjugate plateau. A secondary gray area along north Mexico after 76 Ma represents the arrival of the Hess conjugate, causing a secondary flat slab under there.

The predicted subsidence and uplift during Late Cretaceous to Eocene (Fig. 38) correlate well with inferences by Flowers *et al*., [2008]. The southwestern plateau subsided by ~800 m by 85 Ma with an average rate of –40 m/m.y., consistent with the inferred 1.5-km-thick marine deposition (Flowers *et al*., 2008), given an isostatic adjustment factor of ~1.8. Dynamic uplifts occurred quickly following subsidence ca. 85 Ma, with an average rate of 30 m/m.y. until ca. 40 Ma, during which ~1.2 km of elevation was gained, also in agreement with the Flowers *et al*. [2008] results (Fig. 38A). It is worth noting that all models predict that there were two stages of uplift since the Late Cretaceous, with both the trends and timing being consistent with one another, although the magnitude of uplift varies (Fig. 38B).

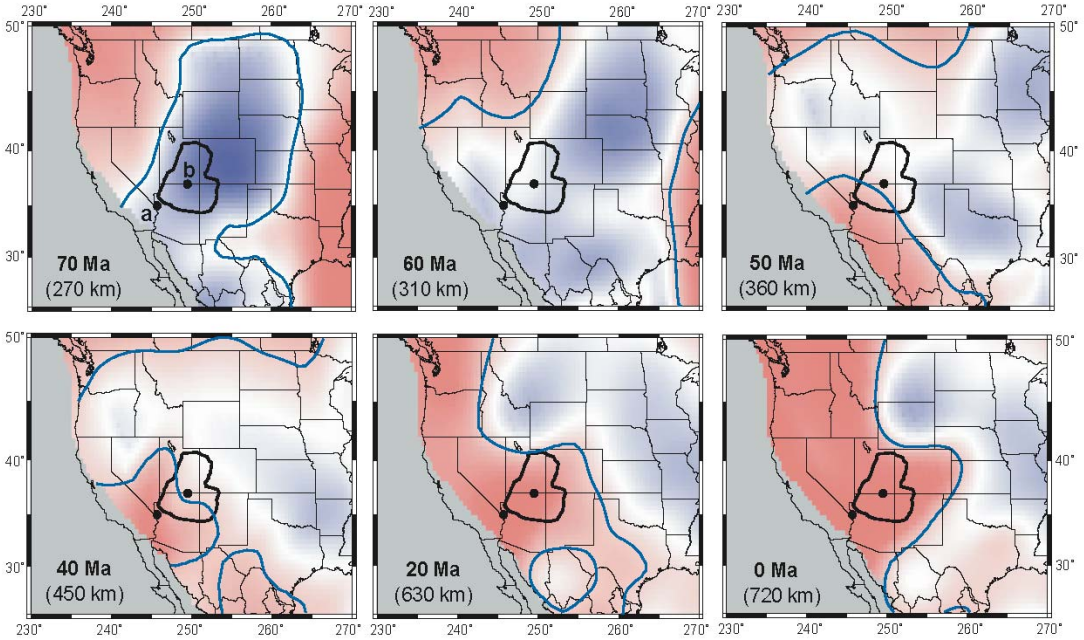

Figure 40 Migration of the Farallon slab inside the mantle beneath the Colorado Plateau after the Late Cretaceous flat subduction from the preferred model in Liu *et al.* [2008]. Each time snapshot corresponds to a different depth where the Farallon slab is best resolved. All time snapshots are projected onto the North American plate. The blue contour represents an isotherm of 30 °C lower than the ambient mantle. Temperature scale is the same as Fig. 35. The two points are the same as in Fig. 33.

5.3.3 Plateau Uplift since Oligocene due to Active Mantle Upwelling

Putative active upwellings associated with upper mantle low seismic velocity anomalies localized beneath the Colorado Plateau were not incorporated in the pure slab models (M1–M3). By including these structures in the inverse model (Fig. 41), the predicted dynamic topography increases by ~700 meters within the Colorado Plateau region (M4) compared to models with only slabs for the present day (Figs. 37E, 37F, and 38B), consistent with recent dynamic models that focus on the late Cenozoic topographic evolution of the plateau [Moucha *et al.*, 2009]. In this case, the earlier evolution of the plateau remains largely the same (Fig. 38B), because the Farallon slab dominates the dynamic topography before the Eocene (Fig. 38B).

We further find that, in models with shallow buoyancy anomalies, lateral variations in lithosphere thickness affect short wavelength surface topographies: A thicker-than-ambient lithosphere associated with the Colorado Plateau predicts the plateau's distinct high topography at present, with sharp topographic gradients on the edge of the plateau (Fig. 37F); a uniform lithosphere thickness leads to a smooth topography with a slightly

reduced magnitude within the plateau relative to that with thicker lithosphere (Fig. 40). The sharp topographic gradient may reflect stress concentration along large viscosity variations inside a convection system, which represents a special mechanism generating surface topographies.

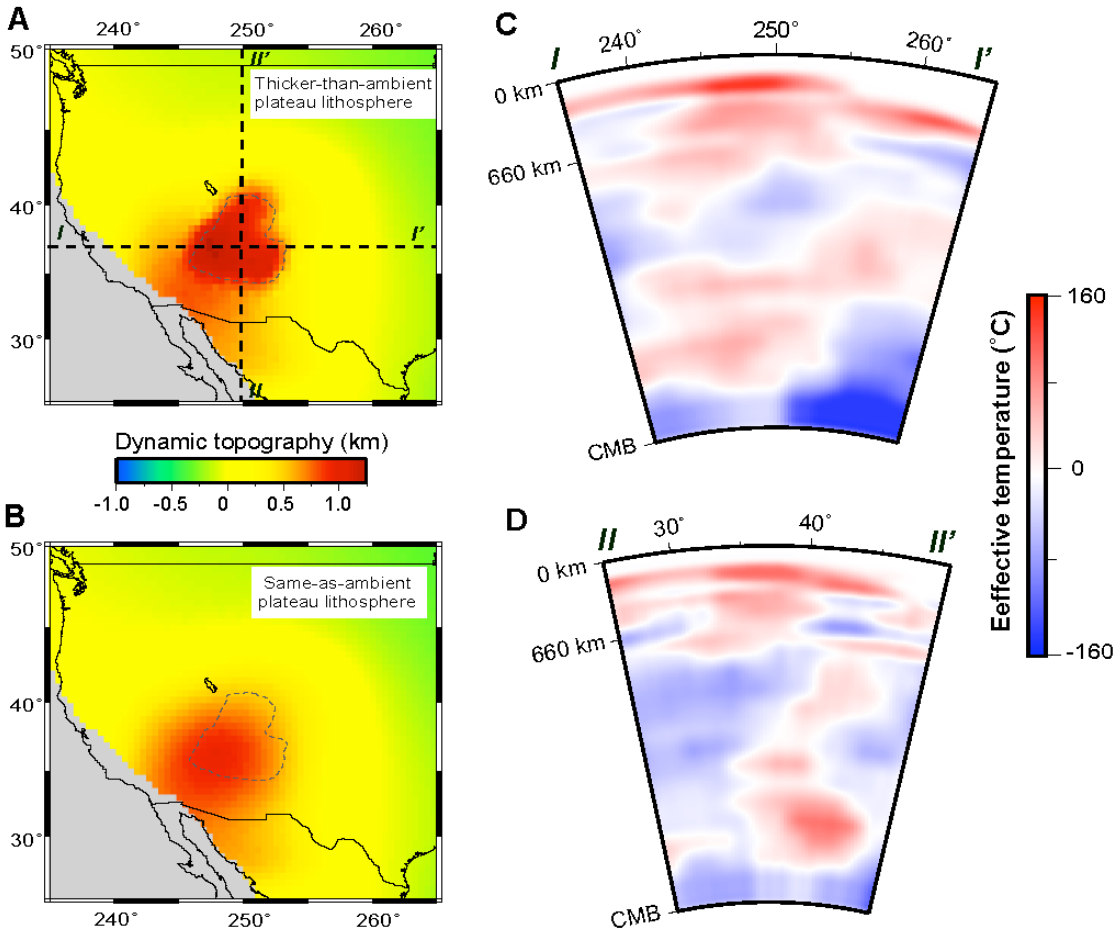

Figure 41 Active upwellings beneath western U.S. and associated surface dynamic topography. A: Predicted present-day dynamic topography by model M4 where the plateau lithosphere is thicker (130 km) than ambient (90 km). The two profiles *I-I'* and *II-II'* indicate cross-sections shown in C and D, respectively. B: Predicted present-day dynamic topography by model M4 where the plateau lithosphere thickness is the same as ambient (90 km). C: East-west vertical profile across the

plateau showing the effective temperature anomaly based on the scaling factor constrained by Liu *et al.* (2008). D: Same as C, but along a north-south vertical profile. In C and D, both the top 150 km signal and that associated with the North American craton are removed.

5.3.4 Tilting of the Plateau during Uplift

Besides the absolute elevation change, dynamic topography also tilts the Colorado Plateau (Figs. 38B and 38C). For example, differential topographies at two end points of a profile (a, b in Figs. 37 and 38) show a tilt in the SW-NE direction.

Specifically, from 100 to 86 Ma, point b subsided more than point a (Fig. 38C), leading to a gentle northeast tilt (Fig. 37B). With the northeastward removal of the flat slab beneath the plateau (Fig. 39), the southwest margin of the plateau rose earlier than the interior (Figs. 38B, C). This northeast tilt became largest ca. 75 Ma, when a differential topography of ~500 meters between the two points was achieved (Fig. 38B).

The tilt diminished at around 60 Ma when the two points (a and b) came to about the same elevation again (Figs. 37C and 38B), driven by the older flat slab moving out to the northeast and younger slab moving below the Colorado Plateau lithosphere from the southwest (Fig. 40). The second uplift phase also accompanied an increase of the northeast tilting, where the southwest margin accumulated >200 m more topography than the plateau interior during the Early Eocene (Fig. 38C), corresponding to the northeast-trending removal of the trailing slab (Fig. 40). Decrease of predicted topography toward the northeast during uplift (Figs. 37 and 38) induced by the northeast-trending subduction of Farallon slab (Fig. 40) may explain the overall northeastward flow direction of the river

drainage systems in central and southern Rocky Mountains [Dickinson *et al*., 1988] and those over the Colorado Plateau [Potochnik, 2001] before the Oligocene.

From 42 to 20 Ma, although absolute uplifts differ among the four models (M1–M4), they all have a diminishing northeast titling, with more topography gained in the plateau interior than the southwest margin (Figs. 38B, 38C). Inclusion of active upwellings (M4) has a change of the tilting direction ca. 15 Ma (Fig. 38B), consistent with the SW carving of the Grand Canyon during the Neogene [Karlstrom *et al*., 2008].

In addition, we note that the predicted dynamic topographies show little change during the Late Cenozoic for all models considered (Figs. 38A, B), consistent with a recent study of clumped carbon isotopes from lacustrine deposits showing that the Colorado Plateau underwent little vertical motion since around 20 Ma (Fig. 38A) [Huntington *et al*., 2010].

5.3.5 Discussion

With an inverse model that satisfies a range of observational constraints, we predict the evolving dynamic topography over the Colorado Plateau from 100 Ma to the present. The area in southwest Utah and northwest Arizona started to raise ca. 85 Ma (Fig. 38B), which seems to mark the inception of the Laramide uplift, while ensuing uplifts until Late Eocene coincide with the entire Laramide orogenic events [DeCelles, 2004]. The predicted two-phase uplift prior to Oligocene seems to agree with the stratigraphically inferred two-stage Laramide orogeny in the southern Rocky Mountain area with an intervening Early

Paleocene deformation hiatus [Cather and Chapin, 1990], although we still do not understand the exact relationship.

In Section 5.2, we show that the flat slab inside the Farallon plate represents a subducting oceanic plateau whose extra initial buoyancy caused the flattening. This also poses another question about the inverse dynamic model: When exactly did the oceanic plateau lose its buoyancy? In other words, will the predicted dynamic subsidence over the western U.S. (Fig. 37) change upon considering this additional complexity during subduction? If the thick crust of the oceanic plateau had completely eclogitized by ~86 Ma, meaning the plateau density did not differ from the ambient lithosphere, the predicted pattern of subsidence is Fig. 37 will hold true.

However, if the eclogite phase transformation was not complete by this time and the plateau still buoyant, the induced surface subsidence above the plateau will be smaller than outside, given the same flat slab geometry from inside out of the plateau area. Because the predicted subsidence over the Colorado Plateau agrees with inferred rock uplift [Flowers *et al*., 2008], we would expect the region right above the flat slab but beyond the thick oceanic plateau, say in Wyoming, to experience more dynamic subsidence than shown in Figure 37. In fact, the Cretaceous sediment isopach does show thicker marine deposits over Wyoming than areas to the south [DeCelles, 2004], and similarly backstripped residual subsidence also decreases southward from Wyoming [Pang & Nummedal, 1995]. Another useful constraint comes from the geoid: Right above the currently subducting Inca plateau in Peru, there is a local geoid minimum [Fig. 42]; this pattern does not correlate well with the surface topography but does with the seismic

image, which suggests deeper mass deficit and indicates that the Inca plateau may have not lost all its extra buoyancy yet.

As a result, this suggests that our inverse dynamic model may have underestimated the density of the Farallon slab beyond the oceanic plateau. Consequently, the lower mantle viscosities inferred by predicting the WIS and borehole subsidence curves is also likely underestimated, since it trades off with slab density (Chapters 3, 4). Of course, further refinement of these mantle properties has to be subject to future research.

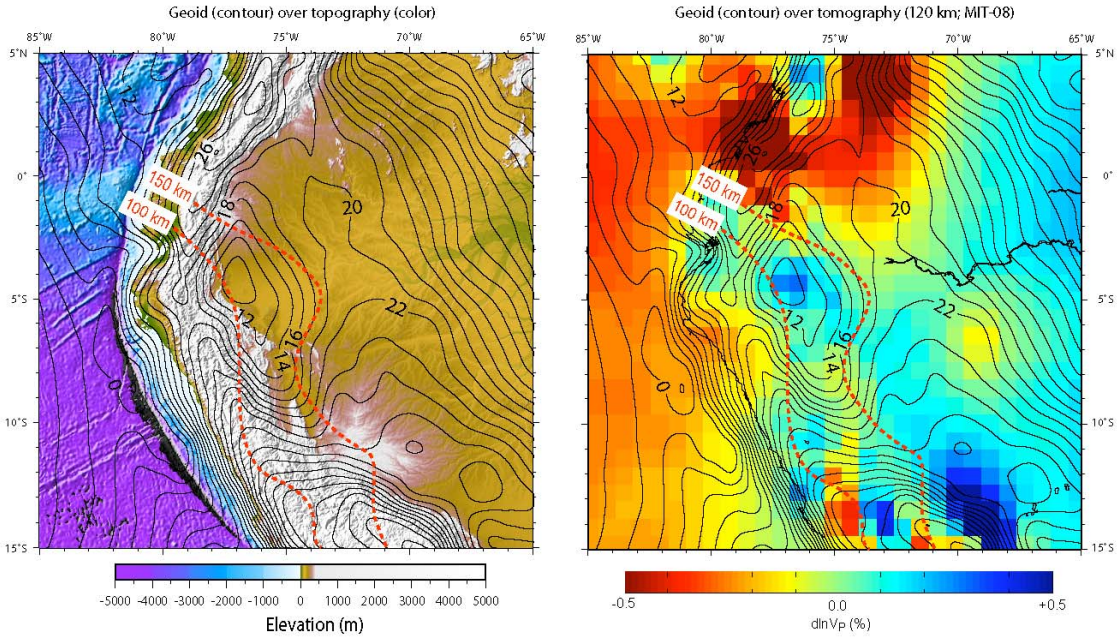

Figure 42 Same as Figure 33, only that both topography (left) and seismic tomography (right) are overlain by geoid (black contours incrementing by 8 meters per interval). Note the geoid low right above the flat slab according to the Inca plateau, indicating that the plateau is still buoyant at this stage of subduction.

When the Colorado Plateau rose above the surrounding areas and formed a unique topographic unit remains unknown. The inverse convection models suggest that Colorado Plateau uplifted high above sea level by the end of Eocene, as part of a broader uplift of the western United States (Fig. 37D), consistent with the high elevations inferred from fossil botanical records for areas surrounding the plateau and the adjacent Basin and Range province [Wolfe *et al.*, 1998]. During the Oligocene, buoyant upwellings further raised the plateau locally (Figs. 38B and 41), while a thicker-than-ambient lithosphere caused sharp edges to the plateau topography, due to enhanced coupling to the upper mantle (Fig. 37F). This suggests that the Colorado Plateau could have became a more isolated crustal block following lithospheric thinning associated with Basin and Range extension. High topography in the Rocky Mountains is not explained by our proposed mantle forces (Fig. 37), which could have resulted from crustal shortening during the Farallon flat subduction [Bird, 1988].

Because the adjoint models satisfy multiple observational constraints during the Late Cretaceous to Early Tertiary, including both the WIS stratigraphy (Chapter 4) and inferences from thermochronology (Chapter 5), we think the predicted vertical evolution of Colorado Plateau before the Late Eocene is likely to be robust. The uplift history after this time associated with the occurrence of active upwellings, however, is less well constrained, where the prediction is only validated by a recent study of clumped carbon isotopes since the Miocene [Huntington *et al.*, 2010]. Given the fact that the nature of low velocity anomalies beneath the CP is less well understood than the Farallon slabs, and that considerable discrepancies in both the magnitude and pattern of these low seismic velocity

anomalies still exist [Grand, 2002; Wang *et al.*, 2007; Burdick *et al.*, 2008; Tian *et al.*, 2009], we propose the dynamic evolution of the putative active mantle upwelling beneath the Plateau may still need more comprehensive constraints, especially in identifying their composition as being chemical (e.g., containing water), thermal or phase changes (e.g., partial melt). As a result, some other mechanisms proposed earlier could still contribute to the Plateau uplift to some extent. For example, the conceptual model of chemical alteration of the Plateau lithosphere during the Farallon flat subduction [Humphreys *et al.*, 2003] argues for uplift due to compositional changes within the lithosphere. On the other hand, a thermal-mechanical model of lithosphere heating due to thermal diffusion after the flat subduction terminates [Roy *et al.*, 2009] provides a mechanism for the topographically higher Plateau rim than the interior.

In summary, the predicted uplift of ~1.2 km for the Colorado Plateau from Late Cretaceous to Eocene was induced by northeastward translation of the Farallon slab, which was augmented by ~700 meters during Oligocene in response to active mantle upwellings beneath the plateau [Fig. 38B]; combined, the two processes largely raised the Colorado Plateau to its current elevation. Because the inverse models are constrained by various geological data from the Late Cretaceous to the present, our predicted trends and timing of plateau vertical evolution could represent important components of the actual motion.

5.4 Implications for the Evolution of the Western Interior Basins

5.4.1 Migrating Depocenter within the WIS Subsidence

Upper Cretaceous strata of the United States western interior basin (WIB) are well suited for quantitative subsidence studies because of precise stratigraphic knowledge [Dyman *et al.*, 1994]. A recent backstripping study along two sections inside the western interior basins were performed by Liu *et al.*, [in revision]. One section extends across central Utah and Colorado (UT–CO); the other across southern Wyoming (WY). Decompaction and flexural backstripping of the UT–CO stratigraphic section are conducted by procedures described in Liu & Nummedal [2004]. The difference between the total decompacted subsidence and the amount of subsidence caused by flexural loading of the Sevier thrust belt, and sediments and water within the WIB, i.e., the "residual" subsidence, across both sections, demonstrates the presence of a dominant, long-wavelength component at all times (Figs. 43 and 44).

As shown in Figs. 43 and 44, a long wavelength (~1000 km) residual subsidence migrated from west to east along both sections. The magnitude of subsidence, averaged along the whole sections, follows a pattern of an initial increase to a maximum in "mid-life" of basin evolution, and a subsequent decrease. A trend of landward translation of the whole long-wavelength subsidence profile in both sections is observed. This trend is characterized by maximum subsidence in the west during time intervals 1 and 2 (Figs. 43, 44), transforming into an eastward-moving trough-shaped subsidence profile during intervals 3 and 4.

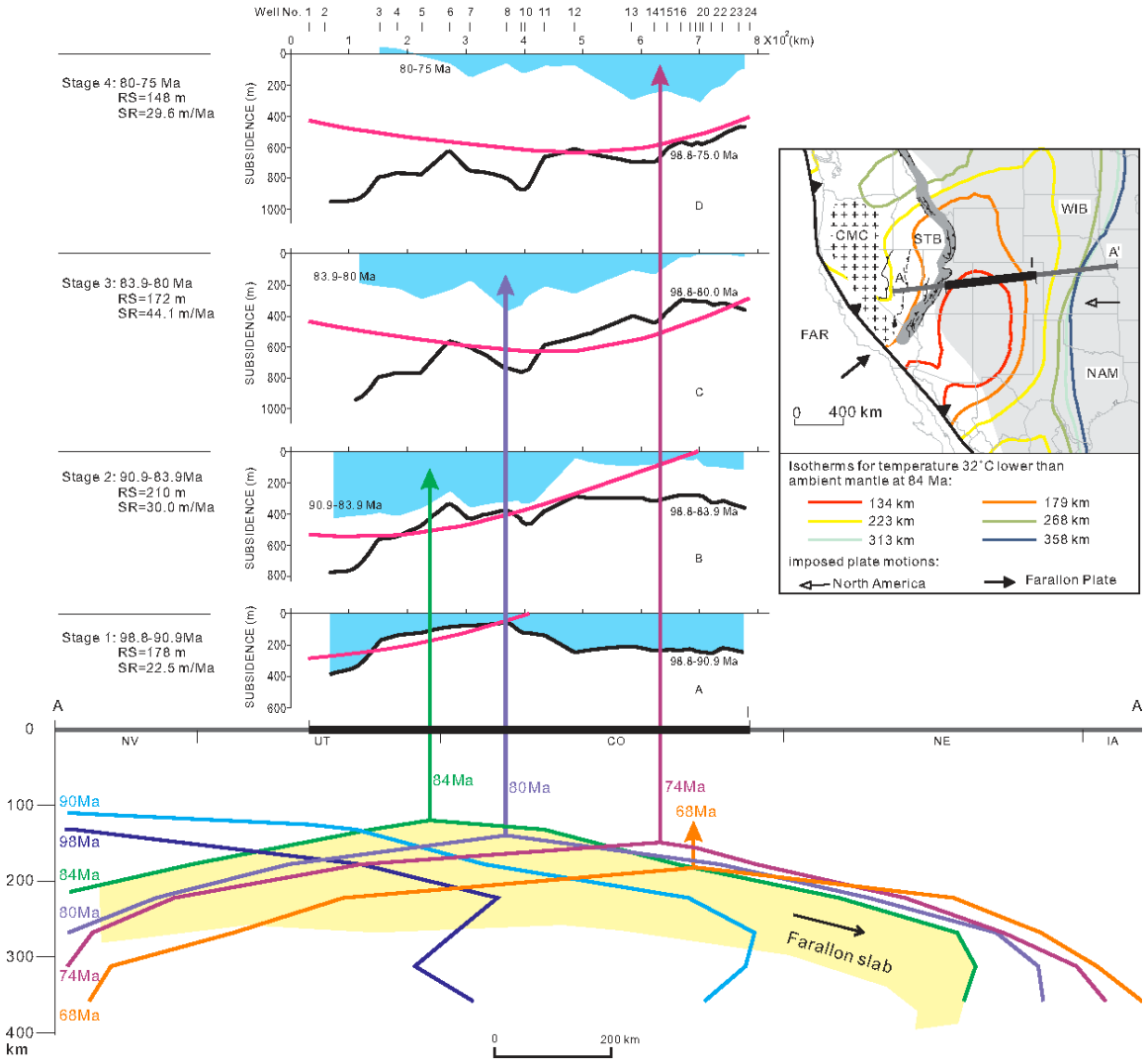

Figure 43 (Upper) Profiles of backstripped residual subsidence and their comparison with modeled dynamic subsidence across UT-CO over four time intervals. Location of this section is shown with the heavy dark line A-A' in the inset map. Black curves and blue-colored bands represent cumulative and incremental residual subsidence, respectively, and the pink curves represent modeled cumulative dynamic subsidence, for each time intervals. RS: incremental residual subsidence averaged over the whole profile; SR: averaged incremental subsidence rate. (Lower) Cross-sectional view of the flat Farallon plate from 98 to 68 Ma, along Section C-C' (heavy gray line in the inset map). Color lines indicate the upper boundary of the slab at different times, represented by an isotherm 32˚C lower than ambient mantle. The whole cross-section of flat slab at 84 Ma is highlighted in light yellow with black arrow indicating its moving direction. Vertical

arrow-lines indicate locations of the slab crests. The inset map shows main tectonic elements (the Cordilleran Magmatic Arc (CMC), Sevier thrust belt (STB), Western Interior Basin (WIB), Northern America (NAM), and Farallon plate (FAR)), and the depth to the upper boundary of the reconstructed Farallon slab at 84 Ma (colored contours). The North American plate is plotted in its present-day coordinates.

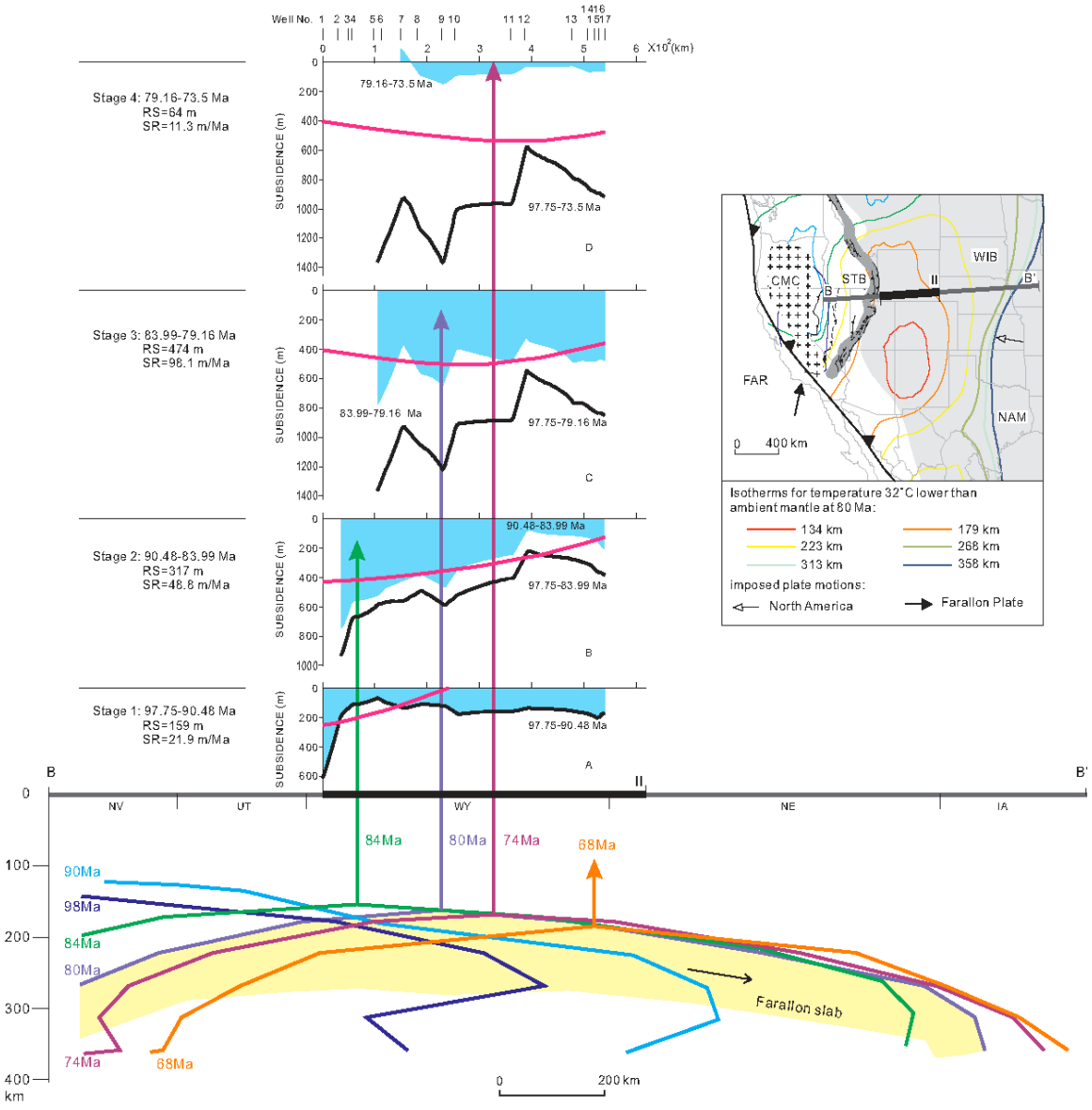

Figure 42 Same as Figure 41, only that this is for the WY section.

This temporal evolution of subsidence suggests that the subducting Farallon plate caused a regionally focused surface subsidence that moved inland over the North American plate. Convection models assuming subduction with a fixed geometry of down-going slabs relative to the overriding plate do not fit this observation, because in such cases, the induced dynamic subsidence patterns on the overriding plate are also stationary. Models involving gradually shallowing and/or steepening subducting oceanic slabs have been proposed to explain the migration of volcanism over the western United States [Coney and Renolds, 1977] and the continental scale tilting of North America [Mitrovica *et al*., 1989]. These earlier models suggest an overall broadening (narrowing) in the extent of dynamic subsidence as the slab shallows (steepens), but not the successive landward shift of subsidence centers, as revealed by our backstripped results.

5.4.2 Implication for Oceanic Plateau Subduction

The observed evolving long-wavelength residual subsidence seems to be consistent with our inverse convection models. By comparing the accumulative residual subsidence with predicted dynamic topography from the inverse model, we find that the overall eastward migration matches both sections (Figs. 43, 44), and magnitudes are also consistent along the UT-CO section (Fig. 43). We, therefore, conclude that these long-wavelength residual subsidence represent the dynamic subsidence caused by the passage of the flat Farallon slab.

Specifically, the eastward-dipping limb of the flat slab before 90 Ma causes the widespread small magnitude subsidence, whereas the high rate of subsidence to the west is

due to the shallower western edge of the slab (Figs. 43, 44, stage 1). As the slab translates inland with its crest beneath eastern UT (Fig. 43) and western WY (Fig. 44) at ~84 Ma, the dynamic subsidence shifts eastward with its highest rates occurring right above the center of the flat slab (Figs 43, 44, stage 2). The increase in dynamic subsidence from stage 1 to 2 is due to the eastward motion of the slab that broadens the subsidence area, and the shallowing of the slab beneath the continent. At ~80 Ma, the dynamic subsidence center moves to western Colorado (and the middle of Wyoming) and the averaged subsidence further increases (Figs 43, 44, stage 3), consistent with it being induced by the shallow flat slab that causes the whole surface profile to subside. The symmetric geometry of the flat slab defines the trough-shaped subsidence profiles. After 80 Ma the Farallon plate changes its direction with respect to North America from east to northeastward during which the Farallon slab sinks deeper into the mantle. Because the bulk of the flat slab was to the south of Wyoming during most of the Late Cretaceous (inset map of Figs 43, 44), the UT-CO section experiences its continued effects, but Wyoming is north of its zone of impact. This generates the continued high subsidence rates in eastern Colorado (Denver basin) to the end of the Cretaceous, whereas dynamic subsidence in Wyoming at this time essentially comes to an end. The migration of subsidence profiles and their correlation with the inferred Farallon slab, therefore, reveals that the western United States underwent dynamic subsidence subject to buoyancy-induced mantle flow, similar to what Australia may have experienced during the Cretaceous [Gurnis *et al*., 1998].

The different rates of dynamic subsidence inferred from the two profiles, with WY experiencing a faster subsidence than UT-CO during time intervals 2 and 3 (Figs. 43, 44),

are not explained by our convection model. Accordingly, the flat slab under WY is deeper than that under UT-CO, and the slab thickness, thus negative buoyancy, under WY is also smaller. If the slab had the same composition under the two profiles, both of these factors suggest a smaller dynamic subsidence along the WY section, opposite of what is observed. Whereas the overall geometry of the localized flat slab is constrained by seismic tomography, its regional variation in composition is not known. This high-resolution stratigraphic data provide additional constraints on the dynamic property of the inferred flat slab: the observed larger dynamic subsidence in WY than in UT-CO strongly argues for a lower density associated with the thickened flat slab.

An ideal candidate for causing such a flat slab is a subducting oceanic plateau, a conclusion reached independently (Chapter 5.2). In this case, the extra buoyancy associated with the thick oceanic crust of the plateau would cause less dynamic subsidence than the denser slab underlying the Wyoming lithosphere to the north. Our argument that the Shatsky conjugate plateau subducted beneath North America during the Late Cretaceous is further supported by this new stratigraphic data. On the other hand, future models simulating the oceanic plateau subduction beneath the western U.S. should attempt to address the problem raised in Figure 45, where the maximum dynamic subsidence occurred to the north of the thick slab, rather than right above (Fig. 45b). Therefore, surface rebound (i.e., uplift) accompanying removal of the oceanic plateau (Fig. 45c) is also likely to have affected areas to the north of Colorado and Utah more than our inverse model have predicted (Figs. 33, 34).

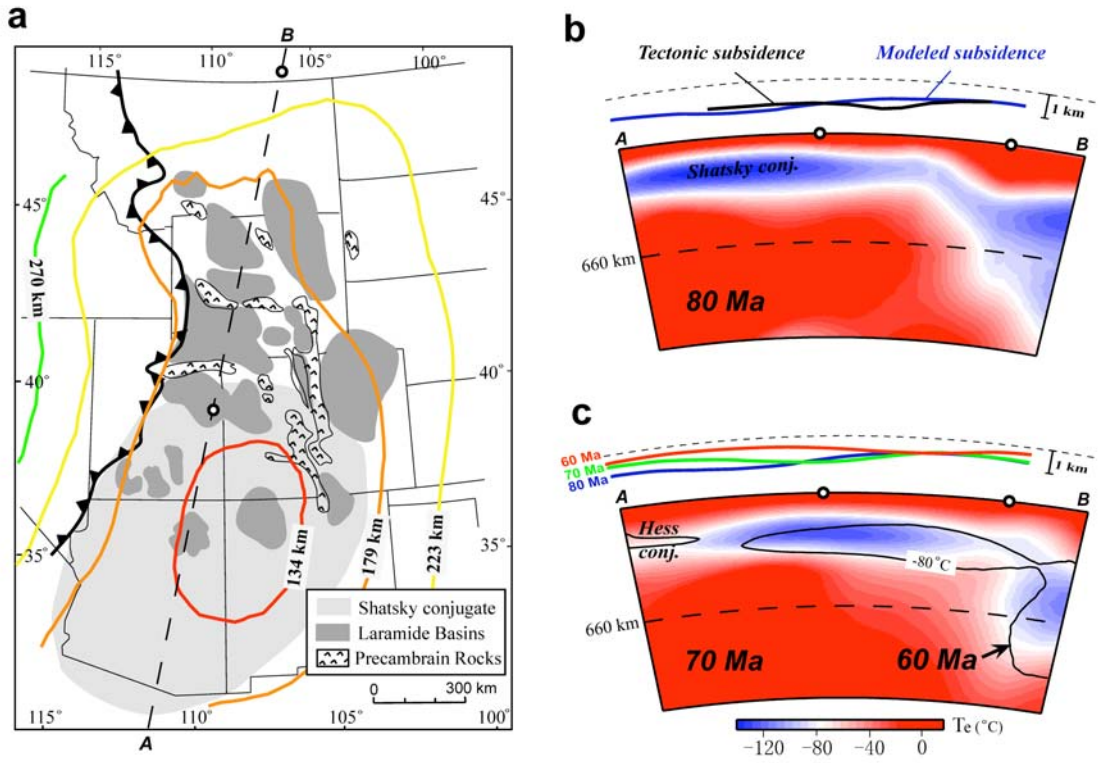

Figure 45 New constraints for improving the inverse model. a) Map view of major Laramide mountains and basins, overlain by slab contours (color) from the inverse model. Profile A−B marks the location of cross-sections shown in b & c. b) Recovered slab geometry from tomography, and predicted dynamic topography that is phased shifted southward relative to observed tectonic subsidence. c) Regional surface uplift accompanying removal of the flat slab from underneath. Color shows the 70 Ma slab geometry, while black contour is for an isotherm (80 °C lower than ambient) at 60 Ma. Predicted Shatsky (80 Ma) and Hess (60 Ma) conjugate plateaus are also shown.

The discrepancy between predicted dynamic topography and observed residual subsidence indicate the inadequacy of the inverse model, and therefore, also provides new constraints on further improving the inverse dynamic model, especially in simulating the exact process of oceanic plateau subduction. First of all, the difference between profile UT-

CO and WY suggests the oceanic plateau maintains at least part of its initial buoyancy at ~80 Ma, consistent with the observation on the present-day Inca plateau, which correlates with a geoid low (Fig. 42). This requires future models to incorporate the appropriate basalt-eclogite phase transformation to accommodate this process of density change.

Second, although patterns of the cumulative subsidence along the UT-CO profile are well predicted, predictions of their time derivatives (differential subsidence, Figs. 43, 44) are not satisfactory. This shows up as a gradual overprediction of dynamic subsidence toward the end of the study period (Fig. 43, 44, stage 3, 4). We also encountered this problem when attempting to predict tectonic subsidence rates from borehole, where a systematic increase of subsidence rate toward the east is predicted, which was absent in the data (Section 4.3). While considering the chemical buoyancy of the oceanic plateau may improve the fit, this may also require the existence of a low viscosity mantle wedge that diminishes surface subsidence above [Billen and Gurnis, 2003].

5. 5 Subsidence of the U.S. east coast since the Eocene

North America has been suggested as a dynamic topography low by using either density structures inferred from seismic tomography [Hager *et al*. 1985; Steinberger, 2007] or the history of subduction [Lithgow-Bertelloni and Richards, 1998]. Both global [Grand, 2002; Ritsema and van Heijst, 2000; Li *et al*., 2008] and regional [Ren *et al*., 2007] seismic tomography models show a linear high seismic velocity anomaly beneath eastern North America at mid-mantle depths, interpreted as the remnants of Farallon plate subduction [Bunge and Grand, 2000; Ren *et al*., 2007]. Independent of these geophysical concepts, Miller *et al.* [2005] made new sea-level estimates that putatively reflect eustasy, based on the backstripping of sedimentary sections at five boreholes located on the New Jersey coastal plain [Van Sickel *et al*., 2004]. The maximum long-term sea-level change is around 70 m [Miller *et al*., 2005], which is lower than most other published global sea-level estimates (Fig. 46A).

Comparison between the Miller *et al*. [2005] long-term sea-level estimate with other estimates shows that there appears to be a significant discrepancy between maximum Late Cretaceous sea levels on the order of 50–200 meters (Fig. 46). Consequently, we hypothesize that the estimate of Miller *et al*. [2005] reflects regional, rather than global sea-level variations on the 10^7-year scale considered in global dynamic models. Further, we suggest that the discrepancy is driven by a dynamic subsidence of the eastern areas of the United States but the magnitude of the subsidence has been somewhat smaller than the fall in global sea level over the same period.

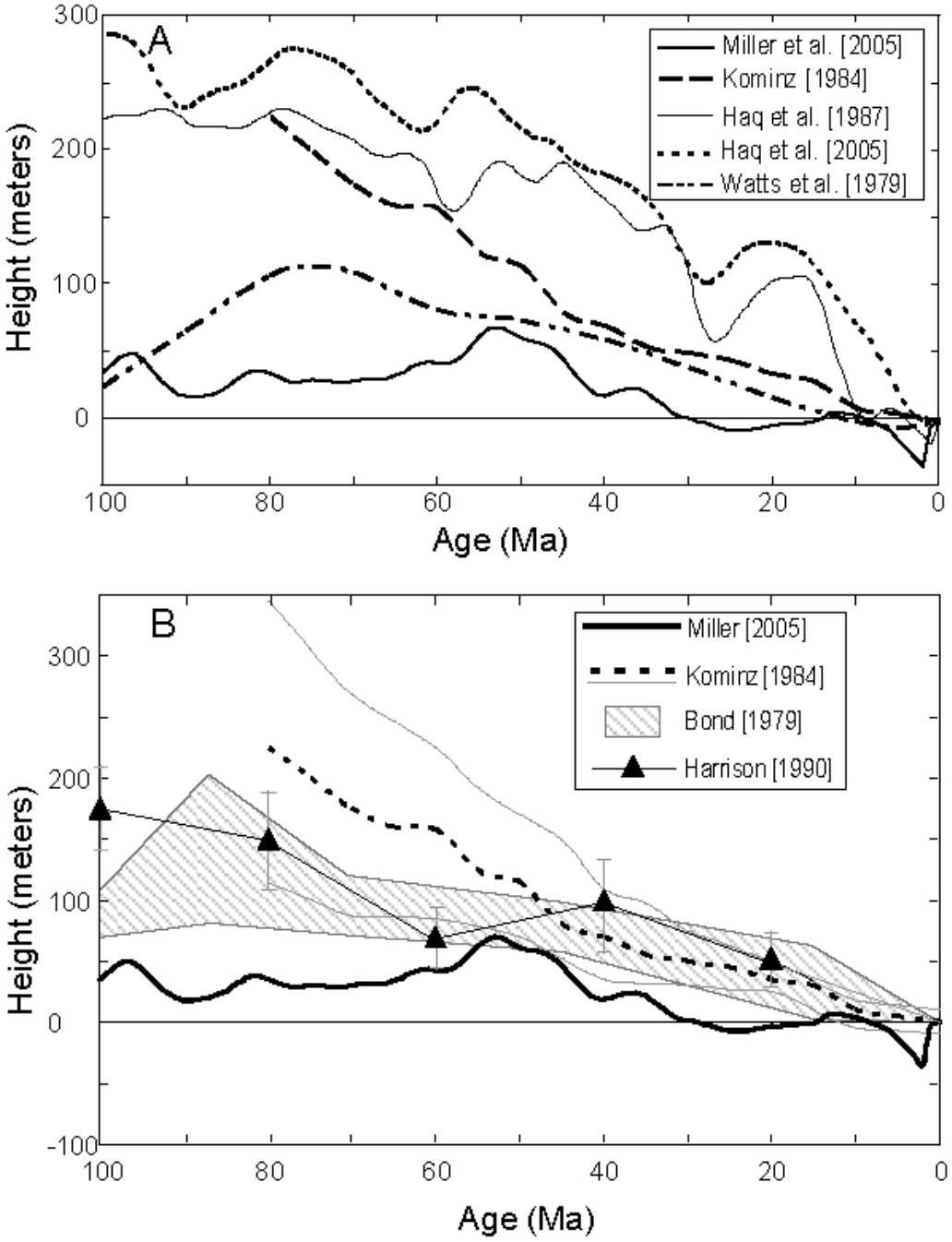

Figure 46 [from Spasojevic *et al*., 2008] Comparison between sea-level curves. (A) Comparison between Haq *et al.*, [1987], Haq and Al-Qahtani [2005], Kominz [1984], and Watts and Steckler [1979] curves with sea-level curve derived for New Jersey coastal plain [Miller *et al.*, 2005] for last 100 million years, smoothed by a 10 m.y. cosine arch filter to isolate long-term sea-level change. (B) Comparison between sea-level estimates based on the analysis of continental flooding

[Harrison, 1990; Bond, 1979] and Miller *et al.* [2005] and Kominz [1984] sea-level curves. Thin continuous lines indicate maximum and minimum estimates from Kominz [1984], hatched area range of estimates from Bond [1979], and black line with triangles average estimates of Harrison [1990] with associated error bars.

Both migration of paleo shorelines in the eastern United States [Spasojevic *et al.*, 2008] and adjoint models of mantle convection (Chapter 4) are used to determine the requisite dynamic subsidence at the east coast. Although the paleo shorelines analysis is characterized by relatively large uncertainty, the trends from the paleo shorelines indicate at least 50 m, and possibly as much as 200 m of subsidence since the Eocene. Details of the paleo shorelines analysis can be found in Spasojevic *et al.* [2008].

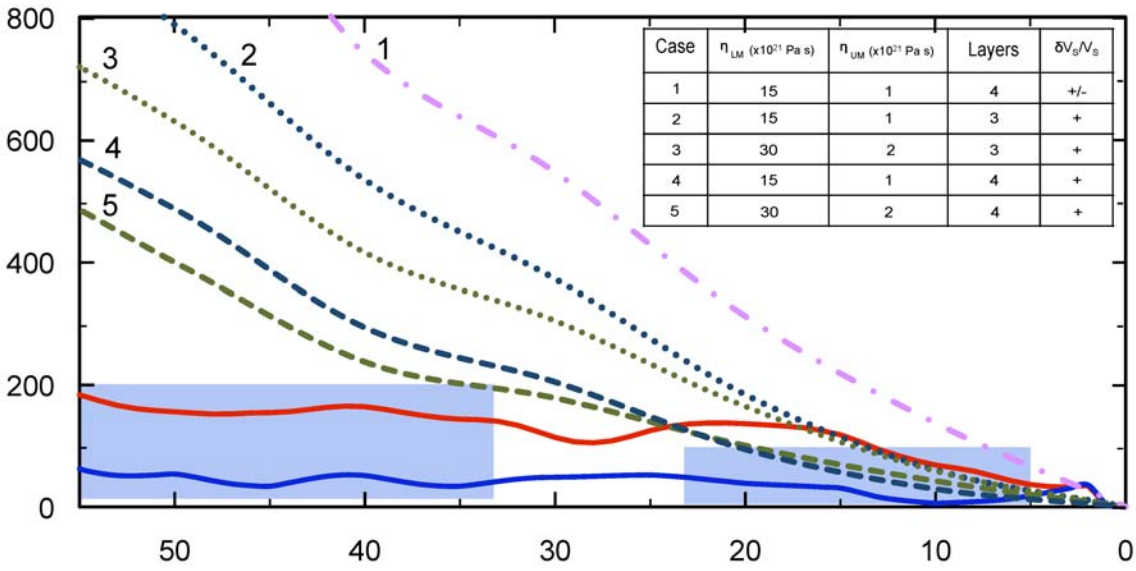

Figure 47 Predictions of the U.S. east coast subsidence. Dynamic topography change for a well in New Jersey coastal plain (coordinates 285°30', 39°30'N) from five dynamic models is shown with colored dotted and dashed lines, solid red and blue lines show difference between sea-level models of Haq and Al-Qahtani [2005] and Miller *et al.* [2005], and Kominz [1984] and Miller *et al.* [2005], respectively. Blue colored boxes show estimated subsidence range from paleo shoreline analysis [Spasojevic *et al.*, 2008] for Eocene and Miocene. Table insert shows model

parameters (η=viscosity, LM=lower mantle, UM=upper mantle viscosity, $\delta V_S/V_S$= seismic anomaly with positive (+) or both positive and negative (+/-) signals included).

All inverse models that we explored predict Tertiary subsidence of the U.S. east coast (Fig. 46). Models that yielded the best fits to WIS borehole subsidence (Fig. 47, cases 2–3) predict 700–900 m subsidence since the early Eocene, and 250 m since the early Miocene. Models scaling both positive and negative S wave anomalies (Fig 47, case 1) yield the largest estimate of post Eocene subsidence. These models (Fig. 47, cases 1–3) overestimate the amount of subsidence, compared with paleo-shorelines and sea-level discrepancies. In order to reduce dynamic subsidence since 55 Ma, we introduce an additional viscosity layer in the uppermost mantle that was not required to fit Late Cretaceous flooding and subsidence. This layer extends from the base of the lithosphere to 410 km depth with a viscosity of 10^{20} Pa s, while the transition zone has a viscosity of 10^{21} Pa s. Estimates of dynamic subsidence since the early Eocene for this four-layer mantle are 480–560 m (Fig. 47, cases 4–5), consistent with subsidence estimates based on paleo shorelines and sea-level discrepancies. Models with additional layer in the upper mantle yield the same Late Cretaceous subsidence and flooding as the three-layer models, given that lower mantle viscosity is the same in both three- and four-layer model, and that upper mantle viscosity in 3-layer model is the same as transition zone viscosity in the four-layer model.

Therefore, the proposed dynamic subsidence can possibly explain the discrepancy between the Miller *et al.* [2005] sea-level curve and other eustatic curves [Spasojevic *et al.,* 2008].

Chapter 6

Broader Implications and Discussions

6.1 Subduction Evolution Beyond North America

In Chapters 4 & 5, we discussed the application of the adjoint models to the evolution of North America, including an initial inversion of Farallon subduction consistent with the WIS, model validation using vertical motion proxies from the Colorado Plateau and WIS basins, and a prediction of possible oceanic plateau subduction through comparison with plate reconstructions and structural geology. As noted earlier, these models were global but with the calibration restricted to North America. Therefore, the model that best fits the constraints from North America may also provide some useful directions on relating surface evolution to internal dynamics over other parts of the world.

Several snapshots of the recovered mantle structures from our preferred adjoint model are displayed in Figure 48. The map view display is centered over the Pacific Ocean, where different color contours outline the restored plates and slabs at different depths (Fig. 48). These solutions are obtained after five forward-adjoint iterations starting with an SBI first guess (Fig. 19), and incorporate the North American-restricted stress guide that mechanically couples the Farallon slab to the Farallon Plate. Model parameters including mantle viscosities and slab density are constrained by predicting the WIS stratigraphy (Chapters 4 and 5). During the conversion of seismic anomalies to buoyancy, we remove the low velocity signals and consider the high velocity anomalies as subducting oceanic slabs. Due to the uneven sampling of seismic ray paths for mantle structures, the slab image

is not smooth and the recovered features near the surface are also irregular (Fig. 48). Most of the widespread sheet-like high velocity mantle anomalies are restored onto main oceanic plates especially the Pacific, Farallon, Nazca and Indian plates (Fig. 48), consistent with the oceanic origin of these slabs.

Overall, the surface high velocity anomalies pulled out along subduction zones to the west and south of the Pacific Ocean (against Japan, Philippines and Australia) are the most voluminous, consistent with the large area and fast subduction speed of the Pacific plate throughout the Cenozoic. Going backward in time, a clear Nazca anomaly is restored up at 30 Ma that keeps expanding in area until the Late Cretaceous, while the Farallon anomaly does not reach the surface until 70 Ma. Within the Indian Ocean, two separate segments of high velocity anomalies are restored, each at a different time: the anomaly against western Australia and Southeast Asia is subducting since ~50 Ma, while the subduction age of the segment to the south of India appears to be older than this time. Both the depth and lateral distance from subduction zones of the remnant slabs revealed by seismic tomography affect their mechanical coupling to the surface, and therefore, their recovered ages of subduction: slabs close to the trench with shallow depth are most strongly coupled to surface plate motions, and translate onto the surface the fastest, such as those surrounding the Pacific; slabs at larger depth are more loosely connected to the surface at present-day, whose recovery takes a longer time, such as the anomaly south of India; slabs that are both deep in the mantle and shifted laterally relative to the trench from which they were subducted are nearly completely decoupled from the surface oceanic plate at present, and an appropriate recovery to their original position on the surface has to be

aided with a stress guide, which also takes the longest time, and one such example is the Farallon anomalies beneath North America.

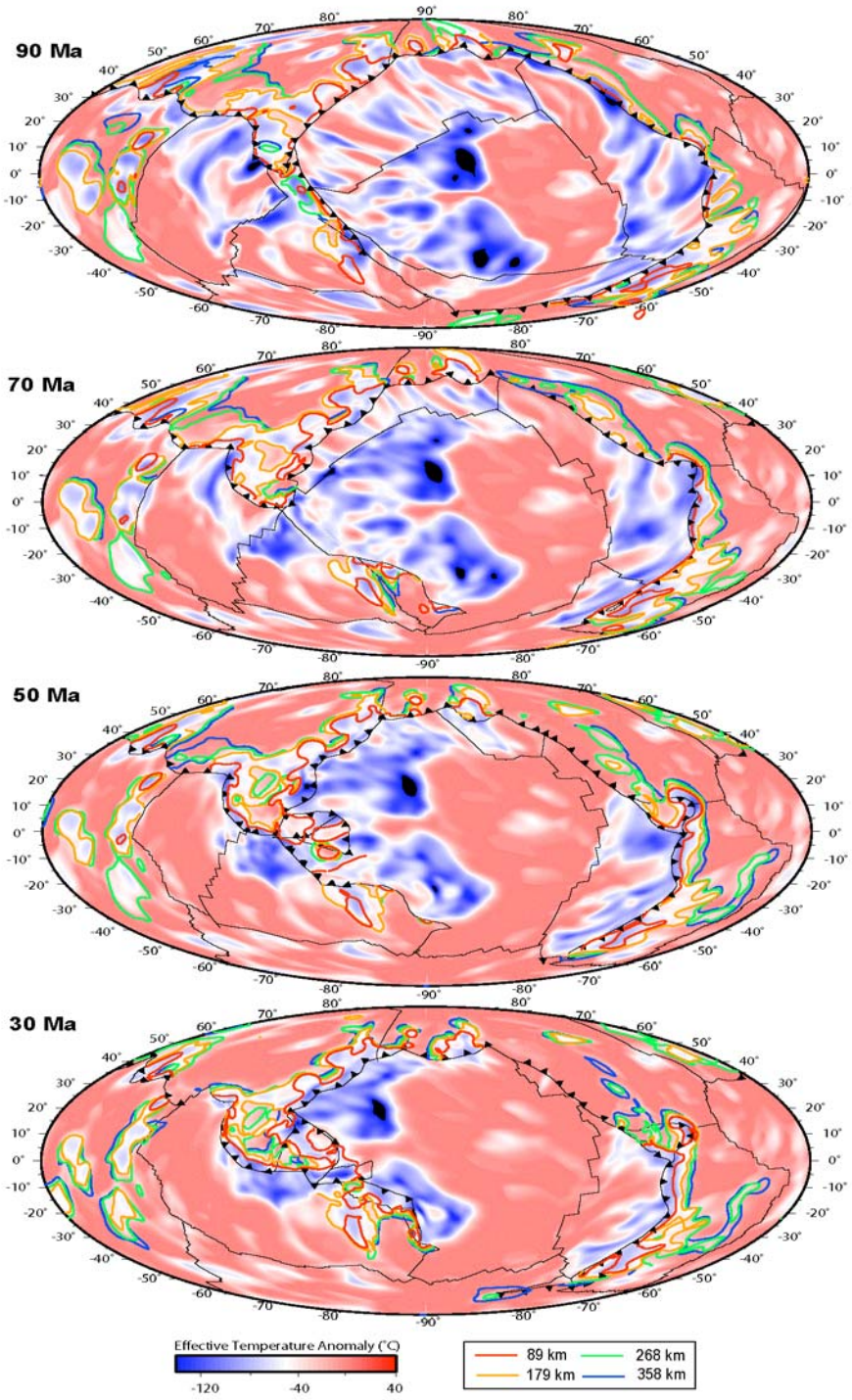

Figure 48. Reconstructed global subduction systems from the adjoint model at four different geological times. The background temperature is at 179 km depth, with color contours indicating slab edges at different depths.

The area of the Pacific Ocean decreases since the Cetaceous due to the retreat of trenches along its western and eastern margins (Fig. 48). During the subduction of oceanic plates, continents move toward the trench, override previously subducted slabs, and experience dynamic subsidence. As can be seen from the discussion in Chapter 4 and 5, North America has been such an example where the westward migration of the continent over the subducting Farallon slabs has led to a dynamic subsidence sweeping from west to east across the entire continent. Since a westward motion also occurred on South America, the continent may have experienced similar vertical motions. Recently, in collaboration with the research group at Sydney University, we analyzed dynamic topography output from the inverse model over South America, and the predicted vertical motion along the Amazon River (Fig. 49). The eastward migrating subsidence center followed by regional uplift in northwest South America, due to the continent's progressive overriding of sinking slabs with the decrease in age of the subducting plate partly responsible, provides an explanation to the reversal of the Amazon River drainage system during the Late Miocene [Shephard *et al*., 2010]. Possible future study areas could include Australia and Southeast Asia where trench retreat also occurred (Fig. 48).

In addition, the morphology and geographic distribution of recovered seismic structures may provide constraints (or feedback) on the imposed plate motions in places where direct measurement from paleo-magnetic data is unavailable. For example, because

the seafloor at the active spreading center has zero age, this part of the oceanic plate represents a discontinuity in the thermal structure of lithosphere, with the part closer to the ridge having less negative buoyancy. Morphology of the recovered Pacific thermal anomalies does not seem to follow this character of a spreading center: in the vicinity of the imposed Izanagi-Pacific ridge, the restored anomalies on the Pacific side shows a strong signature continued from the older part of the plate (Fig. 48, at 70 Ma), instead of giving rise to a weaker-than-ambient signal due to decrease in the age of the lithosphere. Several possible reasons can lead to this inconsistency between recovered thermal anomalies and assumed plate motion history. First, the seismic image beneath East Asia, especially at small scales (~200 km), may still not be well resolved, although increasing agreements among different models are obtained [Grand, 2002; Zhao, 2004; Li *et al*., 2008]. Second, the dynamic properties of the inverse model, including the scaling from velocity perturbation to density anomalies and the depth-dependence of mantle viscosity, may vary geographically, such that the values constrained in North America (Chapter 4) are different from those beneath East Asia; consequently, the recovered Pacific subduction process is not appropriate. A third possibility is that the imposed plate motions are not accurate; in fact, the timing of subduction of the Izanagi-Pacific spreading center against Japan was inferred based on a sequence of idealized assumptions that may not hold true [Whittaker *et al*., 2007], while the mismatch between the restored Pacific anomalies with imposed ridge positions (Fig. 48) may suggest that this ridge could have subducted earlier than assumed. These speculations, of course, are subject to future study with a systematic investigation on the compatibility of the imposed plate motions with recovered seismic anomalies associated with past subduction.

Apparently the inverse models still need further improvement, especially better realizations of the convergent plate boundaries, which is crucial for recovery of subduction zones. Overall, the model shown in Figure 48 seems to have recovered subduction geometries along most of the trenches reasonably well, but small-scale artificial features along subduction zones exist (i.e., cold anomalies get entrained under the overriding plates, where in reality subducted slabs only come from the oceanic plate). This is not the case for North America where its boundary with the Farallon plate is explicitly parameterized as a low-viscosity zone overlying a high-viscosity stress guide, so that the thermal anomalies can become completely restored onto the Farallon plate. Future models should seek a better treatment of all the plate boundaries, especially subduction zones, as expanded on below.

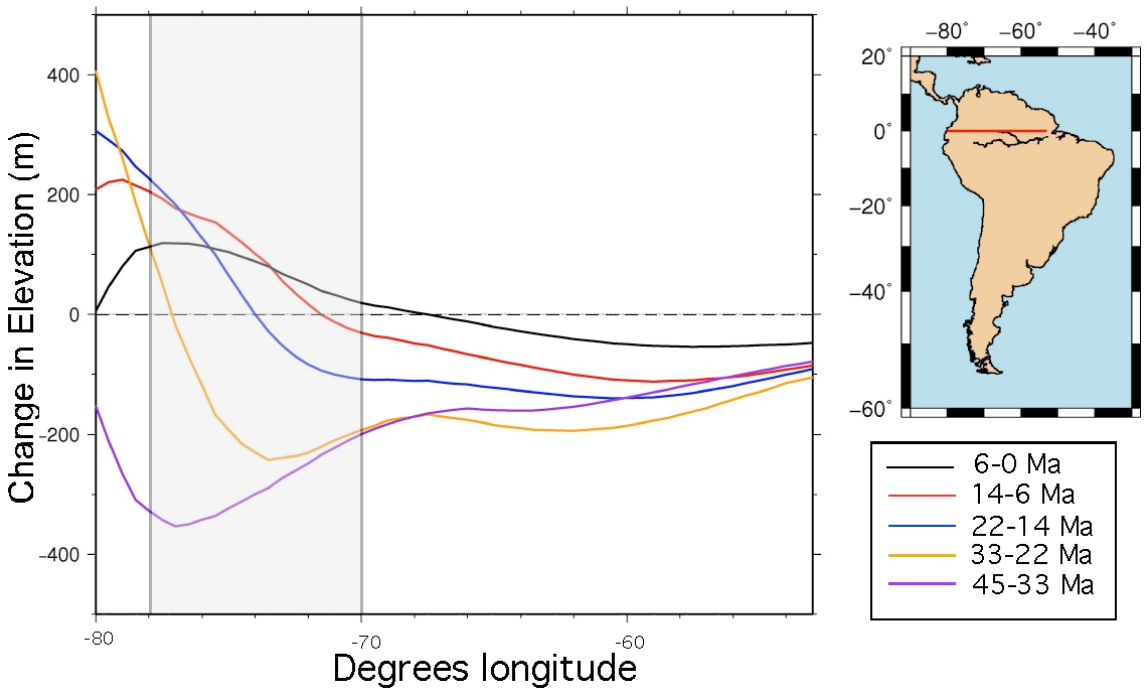

Figure 49 Modeled change in continental elevation of South America at the equator for five stages (from Shephard *et al*., in review). Note the eastward propagating change from subsidence to uplift in the Pebas Sea area after 33 Myrs ago, accompanied by an accentuation of subsidence at the mouth of the evolving Amazon River. Gray band indicates the approximate longitudinal extent of the Pebas Sea at this latitude (adapted from Marshall and Lundberg, 1996).

6.2 Limitations of the Current Adjoint Models

In this thesis, I explored the adjoint data assimilation techniques applied in mantle convection. Stitching together various observational constraints, including both static and time-dependent ones, the adjoint inversion has been shown to be useful in solving geophysical and geological problems. Several important problems have been explained by inverting the present-day seismic tomography image of mantle subject to forced plate motions on the surface. Although promising, the models are still primitive due to both simplifications in physics and limited model resolutions. The major limitations of the adjoint models are as follows.

6.2.1 Poorly Resolved Boundary Layers

In the adjoint models purely based on seismic tomography, the surface and lower (core-mantle boundary) thermal boundary layers (TBL) are not entirely appropriate. Because seismic velocity anomalies revealed by tomographic inversion represents perturbations relative a reference one-dimensional velocity model (e.g., Grand [2002] used a hybrid model where the upper mantle is based on Grand & Helmberger [1984] and lower mantle PREM [Dziwonski & Anderson, 1981]), the resolved seismic image tends to fail in delineating the exact configuration of the upper and lower mantle boundaries. Compositional differences between continental and oceanic lithosphere further complicate the interpretation of tomography image. Consequently, the structure of the adjoint models, converted from seismic velocity anomalies, does not have a realistic lithosphere, both for oceanic plates whose thermal structure is dominated by secular cooling, or continental

whose vertical temperature gradient is more gradual than that of an oceanic plate. In practice, we removed the upper 200 km of mantle from the seismic image, resulting in a "hot" surface (Fig. 48). The models, therefore, did not properly simulate the thermal evolution of the lithosphere or the core-mantle boundary. A possible solution is to prescribe a top TBL before running the inverse model (Fig. 50), as we will discuss later [Section 6.3.1 & 6.3.3]. The same issue for the bottom TBL arises in dealing with lowermost mantle dynamics and heat transfer across the core-mantle boundary (CMB), where a reasonable expression of the temperature jump from the mantle to the core is essential [Bunge, 2005; McNamara and Zhong, 2005; Leng and Zhong, 2008].

Besides the thermal evolution of lithosphere, mechanical deformations are also of great interests. Future models based on the adjoint method could attempt to assimilate a proper definition of continental structures in order to model geological processes within the subducting and overriding plates during active subduction. Recent developments in this direction with forward models include simulating backarc basin evolution [DiCaprio *et al.*, 2009], mantle wedge process and orogenic deformation [Farrington *et al.*, 2010; Rey and Müller, 2010], and fracture of subducting plate inducing possible slab dehydration [Faccenda *et al.*, 2009]. Toward a prediction that can be compared directly with geology, rather than making inferences based on qualitative correlations as we did for explaining the Laramide (Chapter 5), future adjoint models must be improved in representing lithosphere structures.

6.2.2 Uncertain Interpretation of Seismic Tomography

Conversion of seismic velocity anomalies into buoyancy is crucial for the dynamic evolution of the inverse models. During the past decades, increasing consistencies emerge from different tomography models, especially on structures with large spatial scales (>500 km) in areas with good data coverage [Van der Hilst *et al*., 1997; Grand, 2002; Zhao, 2004; Ren *et al*., 2007; Li *et al*., 2008]. However, existing tomography models still show considerable discrepancies in resolving mantle structures at small scales (e.g., features with a dimension of a couple hundred kilometers), due to both the uneven seismic sampling and different resolving powers of inversion techniques [e.g., Grand, 2002]. By comparing different tomography inversions, we find that the Farallon remnant slabs in the lower mantle beneath North America are well resolved, with both the dimensions and magnitude of anomalies consistent among different models. However, the agreement on upper mantle Farallon slabs is much worse, especially among global tomographies. In fact, even the recent high-resolution regional tomography models based on the USArray seismic experiment still show substantial disagreements [Roth *et al*., 2008; Burdick *et al*., 2008; Tian *et al*., 2009], but this situation is likely to be improved given the fact that the surface coverage of USArray is still expanding to the east coast. Consequently, the results we present based on the adjoint models are mostly dealing with the North American evolution prior to the Oligocene time, when the present-day lower mantle Farallon slabs were close to the surface. Because the poorly resolved upper mantle structures do not form a coherent tabular slab system that could allow stresses to transmit along the length of the slab, we had to implement a parameterized stress-guide in order to bring the lower mantle slabs back

onto the surface. A comprehensive study exploring the recent tectonic and geologic evolution during the past 30 million years will require a better-resolved upper mantle image beneath North America, especially those related to the subducted Farallon plate.

Another issue is how to appropriately interpret the low velocity anomalies from seismic inversions. In our models, we removed all the low velocity anomalies from the seismic image when converting into density, essentially assuming that these structures are neutrally buoyant. This assumption is not necessarily valid, given the putative role mantle upwelling plays in terms of driving convection, both in enhancing the long-term mantle-scale flow velocity by forming a 'superplume' above the CMB [e.g., Zhang *et al*., 2010] and in generating focused plume conduits that may form surface hotspots [e.g., Smith *et al*., 2009]. Although the bulk of the large low velocity provinces above the CMB is considered to be chemical in origin based on their seismic properties [Ishii and Tromp, 1999; Masters *et al*., 2000; Ni *et al*., 2002] and their stability in the lower mantle [McNamara and Zhong, 2005; Torsvik *et al*., 2008], they seem to also possess some extra buoyancy driving mantle flow [Lithgow-Bertelloni and Silver, 1998; Gurnis *et al*., 2000; Simmons *et al*., 2007]. Similarly, the low velocity anomalies beneath North America also seem to be thermal-chemical in origin. On the one hand, prediction of the present-day topography of the Colorado Plateau (Chapter 5) requires extra buoyancy associated with the low velocity anomaly beneath the western U.S. On the other hand, magnitudes of dynamic subsidence inferred from regional vs. global sea-level curves suggest that the low velocity anomaly below the U.S. east coast should have little thermal buoyancy, implying a composition-dominant origin of this anomaly. We suggest that a quantitative understanding of the extra

buoyancy associated with the low velocity anomalies beneath North America is subject to future research.

In fact, most tomography models agree better on the high velocity structures than the low velocity ones [Grand, 1997; Li *et al*., 2008], and this indicates that the nature of mantle upwellings is less well understood than that of downwellings. Special attention is needed in dealing with upper mantle structures, where melting may also occur. One good example is the low velocity anomalies revealed by recent regional tomography models beneath western U.S., including the structures below Yellowstone [e.g., Burdick, 2008; Sun and Helmberger, 2010] and Colorado Plateau [Wang, 2007]. A quantitative estimate of composition and properties of these anomalies based on an inverse approach may require an extensive constraining process such as investigating the resulting dynamics on the surface including topography and geoid, heat flow, and a detailed history of magmatism and regional geology. An alternative approach is to simulate melting with forward models following laboratory or petrological empirical relations. Recent work focuses on subduction zones [Kincaid and Hall, 2003; Gorczyk *et al*., 2007; Hebert *et al*., 2009; Zhu *et al*., 2009] and mid-ocean ridges [e.g., Katz *et al*., 2006; Katz, 2008; Ito and Behn, 2008], while a trend is also observed in modeling sub-continental melting processes [Hernlund *et al*., 2008; Conrad *et al*., 2010].

6.2.3 Simplification in Physical Assumptions

In order to keep the number of unknowns small, we have assumed a simple mantle structure during the inversion of the Farallon subduction. For example, the model has a three-layer viscosity structure, without any phase transformations or possible chemical anomalies. Through forward models, we find that the phase change at 660 km depth plays a smaller role in controlling Farallon plate subduction, compared with the total buoyancy associated with the slabs. Since the Olivine-Spinel phase transformation at ~410 km depth tends to enhance subduction while the Spinel-Perovskite phase change at 660 km depth tends to slow down the subducting slabs, the net buoyancy effects of these two competing phase changes is playing a minor role controlling the overall speed of subduction, given that the slab is strong enough to transmit thermal buoyancy along the length of the slab [e.g., Billen, 2008]. Phase transformations will affect the morphology of slabs when the slab rheology varies along its length and thermal buoyancy diminishes (say, due to young slab ages). Because these phase changes occur at different depths (above and below the mantle transition zone), the down-going slab will experience a torque that can deform the flow pattern locally by causing slab thickening or buckling within the transition zone [e.g., Christensen, 1996; Tetzlaff & Schmeling 2000; Cízkova *et al*. 2002]. Therefore, in a more realistic model, these physical processes still need be incorporated. Other phase changes may also be considered in future models, including a possible post-peroviskite transformation at the core-mantle boundary [Sidorin *et al*., 1999; Hernlund *et al*., 2005] and the basalt-ecologite transformation at the base of the lithosphere [Ringwood and Green,

1966], which may affect subduction dynamics through changing the density and rheology of slabs [e.g., Ji and Zhao 1994].

Although the influence of phase changes may be secondary compared to the overall buoyancy of thermal anomalies, both the adiabatic compressibility of the mantle with depth and the decreasing thermal expansion coefficient at higher pressures can affect convection [e.g., Hansen *et al.*, 1994]. Another factor that influences slab morphology is rheology: with varying slab strength relative to the surrounding mantle, the subducting slabs will evolve into different geometries [e.g., Billen, 2008; Stegman *et al.*, 2010]. It is, therefore, important to explore the effects of rheology on the style of subduction and generation of surface plates [Zhong and Gurnis, 1996; Tackley, 2008; Stegman *et al.*, 2010], especially for the development of fully dynamic inverse models (i.e., the prediction rather than the imposition of surface plate motions, see next section for more discussion). However, we realize that, within the adjoint models, a sophisticated realization of complex slab rheology as that used in forward models [e.g., Billen, 2008] is limited by the intrinsically low resolution images obtained by seismic tomography. A possible solution is through a hybrid model with explicitly defined upper mantle slabs embedded in the adjoint models (see section 6.3.3).

6.2.4 Limited Applications with Forced Convection

As mentioned in the previous section, the adjoint models we developed use prescribed surface velocities rather than predicting them by the internal convection of the mantle, i.e., a forced convection. With surface plate motions imposed as boundary

conditions, mantle flows close to the surface (e.g., within the lithosphere) are largely passive, while convection at larger depth is more subject to internal buoyancy forces. Consequently, these models have limited applications in exploring the driving mechanism of motions of tectonic plates, which has been an import unresolved question. Potentially, uncertainties or errors associated with plate reconstructions can be mapped into model results, although some of these artifacts can be ruled out through comparisons with tomography image [Bunge and Grand, 2000] or together with geology [Van der Meer *et al.*, 2010].

While imposed velocity boundary conditions take plate motions as constraints, a fully dynamic model treats them as predictions, which, by comparison to the observed values, inform us of the driving mechanism of plate tectonics and mantle convection [e.g., Stadler *et al.* 2010]. In order to construct a fully dynamic model, special attention must be paid to slab rheology and numerical resolution. The essence of plate tectonics is that the surface shell of the earth can be divided into quasi-rigid pieces that are moving relative to each other with most of the deformation occurring at their boundaries. This requires a proper rheology that generates plate-like kinematics with either prescribed weak zones between strong slabs [Zhong and Gurnis, 1996] or yielding stresses that allow certain parts of the rigid plate to weaken [Tackley, 2008]. On the other hand, mesh resolution and computational cost are additional limitations for large-scale numerical models. This is especially the case in models with a more realistic parameterization of plate boundaries including faults or orogenic deformations. More discussion about this issue can be found in the next section.

6.3 Some Thoughts on Future Model Development

Given the limitations of the current models and possible developments of data and techniques, future geodynamic models with data assimilation may be improved in the following aspects.

6.3.1 Tomography: Push the Limit of Resolution

Global tomography models usually have poor resolving power for fine-scale features, because both their long ray path inside the mantle and coarse data coverage on the surface cause smoothing of the inverted seismic image [e.g., Ritsema *et al*., 2007]. Regional tomography, with shorter ray path and denser coverage of receivers, reveals the local structures better. Recent development of tomographic inversions based on finite-frequency sensitivity kernels using multiple frequency bands may resolve structures better [Sigloch *et al*., 2008; Li *et al*., 2008]. Toward a realistic representation of mantle structure, the most promising approach is adjoint tomography, which avoids the blurring effect of seismic inversion by solving for the seismic wave field in a domain with full 3-D seismic velocity anomalies. Such model have increased wave speed variations up to several tens of percents, much larger than the standard perturbations expressed in traditional tomography [Tape *et al*., 2009]. The adjoint tomography, however, is computationally expensive, and has only been applied locally.

With the continuing deployment of the USArray seismic network across the U.S., several high-resolution tomography models have appeared in the literature [Sigloch *et al*., 2008; Burdick *et al*., 2008; Roth *et al*., 2008; Tian *et al*., 2009]. Various features have been detected beneath the western U.S., including a parallel-subducting slab doublet related to

the Juan de Fuca plate subduction [e.g., Burdick *et al*., 2008; Roth *et al*., 2008], a controversial high velocity anomaly below Nevada [West *et al*., 2009], and plume-like low velocity anomalies around Yellowstone [Sigloch *et al*., 2008; Burdick *et al*., 2008; Roth *et al*., 2008; Sun and Helmberger, 2010]. These new generation of regional tomography models provides a chance for the adjoint convection model to recover the recent evolution of subduction along western North America.

I have started to develop such a high-resolution inverse convection model based on the tomography of Burdick *et al*. [2008] to reverse the subduction process beneath western U.S. since the Miocene. The effective temperature anomalies scaled from tomography is shown along a east-west profile at 41°N (Fig. 50). A temperature-dependent viscosity with lateral variations by four orders of magnitude is used, and a thermal boundary layer on top is included. Inversion to the past based on this model is still ongoing research.

Regional high resolution tomography models below the western U.S. based on either different datasets [Burdick *et al*., 2008 vs. Tian *et al*., 2009] or different inversion techniques [Roth *et al*., 2008 vs. Burdick *et al*., 2008] show significant consistency for the major features, especially the upper mantle slab structures. Eventually this will help to construct a coherent image of the Farallon subduction by connecting the upper and the lower mantle structures. This may also provide a chance for a more realistic reconstruction of the Farallon subduction, where the stress-guide discussed in Chapter 4 is no longer necessary.

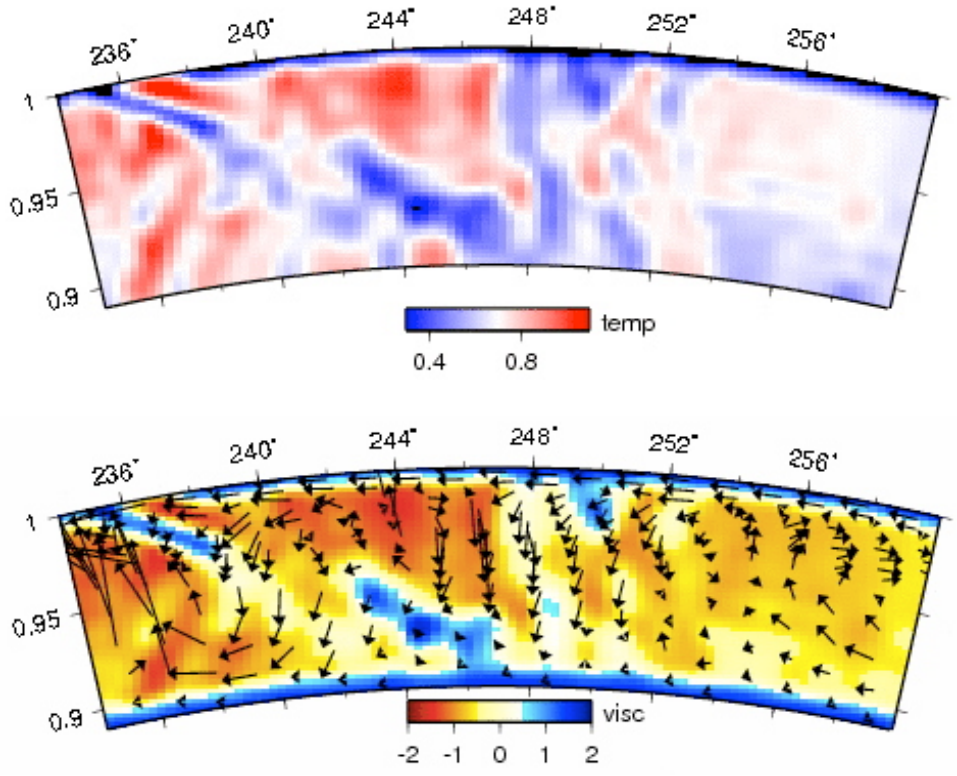

Figure 50 E-W cross-section along latitude 41°N in western U.S. upper mantle, showing its present-day buoyancy field. (Top) Temperature anomaly converted from seismic image of Burdick *et al*. [2008]. A thermal boundary layer is added, and the Juan de Fuca slab redirected to its surface plate at the trench (~236°E longitude). Vertical axis shows normalized radius. (Bottom) The viscosity structure based on a temperature-dependent rheology (relative to 10^{21} Pa s) and the density driving flow field (arrows) with the plate motion imposed as boundary conditions on top.

6.3.2 Constraints: Multiple Datasets

So far, we have attempted assimilation of several different datasets into the inverse model, including seismic tomography, plate motions and surface dynamic topography. We also adopted qualitative constraints from structural geology after the fact for further model validation, but have not established a formal algorithm allowing strict assimilation of these datasets.

In theory, any observation related to the dynamics of the mantle could constrain the model. On the other hand, application of these constraints is restricted by limitations of the numerical models. As more powerful and adaptive algorithms are created in future simulation software, more types of data can be brought in, which will make the model more earth-like. With the current computational ability of the software CitcomS, other observations like the geoid [Zhong *et al.*, 2008] can be extended into our predictions. Future inverse models with data assimilation should follow this trend, as is the same path the general circulation models in meteorology and oceanography have covered.

As every single simulation approach has its own limitation in terms of assimilating data and representing the earth, mutual consistencies between different modeling techniques are an important alternative measure of the validity of a physical model. The adjoint models, by satisfying various data with distinct natures, have the potential to better explain the evolution of solid earth than traditional means. With the several existing limitations improved, such as realistic boundary layers, more complete physical assumptions and higher numerical resolutions (Section 6.2.1), the adjoint models will gradually move toward this goal.

6.3.3 Algorithm: Hybrid Models

By purely assimilating seismic images, the inverse model cannot represent the thermal boundary layers of the mantle properly. This is because tomography inversions based on body waves (representing the majority of such models), especially for global tomography, have little sensitivity to shallow structures like the crust, because the ray paths

are largely vertical at shallow depth [e.g., Grand, 2002; Burdick *et al*., 2008]. Therefore, the adjoint convection models converted from tomography also do not have a realistic lithosphere structure. Since most geophysical and geological observations are recorded at the earth's surface, an appropriate representation of the lithosphere is important, especially for future high-resolution models with extensive data assimilation. A possible way to solve this problem is to prescribe the lithosphere via traditional forward modeling techniques and maintain this constraint during the adjoint iterations, so that not only are major mantle structures captured based on scaled seismic images, but that fine features along boundary layers can also be expressed through explicit definitions with forward modeling (e.g., Fig. 50). In this case, the iterative procedure of the adjoint inversion will need to be updated so that it does not overwrite the forward constraints.

Another advantage of hybrid models is to help increase local numerical resolutions. As global models based on traditional uniform meshing are computationally expensive, and regional models suffer from artificially imposed vertical boundaries, new mathematical concepts for more efficient calculation must be generated. One approach has been to use a nested model where a coarse global model contains a finer regional one [Tan *et al*., 2006]. An alternative means is adaptive mesh refinement and coursing (AMR) techniques, which allow realization of local features with high resolutions while maintaining the total number of mesh grids largely the same [Burstedde *et al*., 2008; Stadler *et al.* 2010]. Implementation of these techniques is likely to improve the power of future geodynamic models greatly.

BIBLIOGRAPHY

Atwater, T., and J. M. Stock, Pacific-North America plate tectonics of the Neogene Southwestern United States - An update, *Int. Geol. Rev., 40*, 375-402, 1998.

Billen, M. I., and Gurnis, M., Comparison of dynamic flow models for the Central Aleutian and Tonga-Kermadec subduction zones, *Geochem., Geophys., Geosys.*, 4(4), 1035, doi:10.1029/2001GC000295, 2003.

Billen, M., Modeling the dynamics of subducting slabs, *Annu. Rev. Earth Planet. Sci., 36*, 325–356, 2008.

Bird, P., Formation of the Rocky Mountains, western United States: A continuum computer Model: *Science*, 239, 1501–1507, doi: 10.1126/science.239.4847.1501, 1998.

Bond, G., Evidence for continental subsidence in North America during the Late Cretaceous global submergence, *Geology*, 4, 557 (1976).

Bond, G. C., Evidence for some uplifts of large magnitude in continental platforms, *Tectonophys.*, 61, 285-305, 1979.

Bunge, H.-P., M. A. Richards, Lithgow-Bertelloni, C., J. R. Baumgardner, S. P. Grand, and B. A. Romanowicz, Time Scales and Heterogeneous Structure in Geodynamic Earth Models, *Science*, 280, 91-95, 1998.

Bunge, H.-P. and Grand, S. P., Mesozoic plate-motion history below the northeast Pacific Ocean from seismic images of the subducted Farallon slab, *Nature*, 405, 337-340, 2000.

Bunge, H-P., M. A. Richards and J. R. Baumgardner, Mantle-circulation models with sequential data assimilation: inferring present-day mantle structure from plate-motion histories, *Phil. Trans. R. Soc. Lond.*, A360, 2545-2567, 2002.

Bunge, H.-P., C. R. Hagelberg, and B. J. Travis, Mantle circulation models with variational data assimilation: Inferring past mantle flow and structure from plate motions histories and seismic tomography, *Geophys. J. Int.*, 152, 280-301, 2003.

Bunge, H.-P., Low plume excess temperature and high core heat flux inferred from non-adiabatic geotherms in internally heated mantle circulation models, *Phys. Earth Planet. Int.*, 153(1-3), 3-10, 2005.

Burchfiel, B.C., Cowan, D.S., and Davis, G.A., Tectonic overview of the Cordilleran orogen in the western United States, *in* Burchfiel, B.C., et al., eds., The Cordilleran orogen: Conterminous U.S.: Boulder, Colorado, *Geol. Soc. Ame.*, Geology of North America, G-3, 407–479, 1992.

Burdick, S., et al., Upper mantle heterogeneity beneath North America from travel time tomography with global and USArray transportable array data, *Seism. Res. Lett.*, 79, 384-390, 2008.

Burgess, P.M., M. Gurnis, L. Moresi, Formation of sequences in the cratonic interior of North America by interaction between mantle, eustatic and stratigraphic processes, *Bull. Geol. Soc. Am.* 109, 1515, 1997.

Burkett, E. and M. I. Billen, Dynamics and Implications of Slab Detachment Due to Ridge-Trench Interaction, *J. Geophy. Res*, 114, B12, B12402, 2009.

Burstedde, C., O. Ghattas, M. Gurnis, G. Stadler, E. Tan, T. Tu, L. C. Wilcox, and S. Zhong, Scalable adaptive mantle convection simulation on petascale supercomputers, *International Conference for High Performance Computing, Networking, Storage, and Analysis (ACM/IEEE Supercomputing 2008)*, 15, 2008.

Cammarano, F., S. Goes, P. Vacher & D. Giardini, Inferring upper-mantle temperatures from seismic velocities, *Phy. Ear. Plant. Int.* 138, 197-222, 2003.

Campa, M.-F., in *Tectonostratigraphic Terranes of the Circum-Pacific Region. Circum-Pacific Counc. Energy Miner. Resour., Earth Sci. Ser.* (ed. Howell, D.G.) 299-313, 1985.

Cather, S.M. and Chapin, C.E., Paleogeographic and paleotectonic settings of Laramide sedimentary basins in the central Rocky Mountain region: Alternative interpretation and reply: *Geol. Soc. of Am. Bull.*,102, 256–260, 1990.

Christensen, U.R., The influence of trench migration on slab penetration into thelower mantle, *Earth Planet. Sci. Lett*., 140, 27-39, 1996.

Coney, P. J. and S. J. Reynolds, Cordilleran benioff zones, *Nature*, 270, 403-406, 1977.

Cízkova H, J. van Hunen, A.P. van den Berg, N.J. Vlaar, The influence of rheological weakening and yield stress on the interaction of slabs with the 670 km discontinuity, *Earth Planet. Sci. Lett*. 199, 447–57, 2002.

Conrad, C.P., and C. Lithgow-Bertelloni, How mantle slabs drive plate tectonics, *Science*, 298, 207-209, 2002.

Conrad, C. P. and M. Gurnis, Seismic tomography, surface uplift, and the breakup of Gonwanaland: Integrating mantle convection backwards in time. *Geochem. Geophys. Geosys., 4(3)*, 1031, 2003.

Conrad, C.P., C. Lithgow-Bertelloni, and K.E. Louden, Iceland, the Farallon slab, and dynamic topography of the North Atlantic, *Geology, 32*, 177-180, 2004.

Conrad, C.P., B. Wu, E.I. Smith, T.A. Bianco, and A. Tibbetts, Shear-driven upwelling induced by lateral viscosity variations and asthenospheric shear: A mechanism for intraplate volcanism, *Phys. Earth and Planet. Inter.*, 178, 162-175, 2010.

Costa, J. B. S., Bemerguy, R. L., Hasui, Y. & da Silva Borges, M. Tectonics and paleogeography along the Amazon river. *J. S. Am. Earth Sci.* 14, 335-347, 2001.

Cross, T. A., and R. H. Pilger, Tectonic controls of Late Cretaceous sedimentation, westem interior, USA, *Nature, 274*, 653-657, 1978.

Debiche, M.G., A. Cox and D. Engebretson, The motion of allochthonous terranes across the North Pacific basin, *GSA Spec. Pap.*, 207, 1-49, 1987.

DeCelles, P.G., Late Jurassic to Eocene evolution of the Cordilleran thrust belt and foreland basin system, Western U.S.A, *Am. J. Sci*., 304, 105–168, 2004.

DiCaprio, L., M. Gurnis, and R. D. Müller, Long-wavelength tilting of the Australian continent since the Late Cretaceous, *Earth and Planet. Sci. Lett.*, 278, 175–185, 2009.

DiCaprio, L., R. D. Mueller, M. Gurnis, and A. Goncharov, Linking active margin dynamics to overriding plate deformation: Synthesizing geophysical images with geological data from the Norfolk Basin, *Geochem., Geophys., Geosys.*, 10, Q01004, 2009.

Dickinson, W.R., Klute, M.A., Hyes, M.J., Janecke, S.U., Lundin, E.R., McKittrick, M.A., and Olivares, M.D., 1988, Paleogeographic and paleotectonic settings of Laramide sedimentary basins in the central Rocky Mountain region: *Geol. Soc. Am. Bull*., 100, 1023–1039, 1988.

Druschke, P., A.D. Hanson, M.L. Wells, T. Rasbury, D.F. Stockli, and G. Gehrels, Synconvergent surface-breaking normal faults of Late Cretaceous age within the Sevier hinterland, east-central Nevada, *Geology* 37, 447-450, 2009.

Ducea, M.N., S. Kidder, J. T. Chesley & J. Saleeby, Tectonic underplating of trench sediments beneath magmatic arcs: the central California example, *Int. Geol. Rev.* 51(01), 1-26, 2009.

Dyman, T.S., Merewether, E.A., Molenaar, C.M., Cobban, W.A., Obradovich, J. D., Weimer, R.J. & Bryant, W.A. in *Mesozoic systems of the Rocky Mountain region, USA* (eds Caputo, M. V., Peterson, J. A. & Franczyk, K. J.) 365–392 (*Soc. Sedim. Geol*., Denver, 1994).

Dziewonski, A.M. and D.L. Anderson, Preliminary reference Earth model, *Phys. Earth Planet. Inter*., 25, 297-356, 1981.

Engebretson, D.C., A. Cox and R.G. Gordon, Relative motions between oceanic and continental plates in the Pacific basin, *GSA Spec. Pap*., 206, 1-59, 1986.

English, J. M, and S. T. Johnston, Laramide orogeny: what were the driving forces? *Inter. Geol. Rev., 46*, 833-838, 2004.

Faccenda, M., T.V. Gerya1 and L. Burlini, Deep slab hydration induced by bending-related variations in tectonic pressure, *Nature Geoscience*, 2, 790-793 2009.

Farrington, R., D.R. Stegman, L. Moresi, M. Sandiford and D.A. May. Interactions of 3D Mantle Flow and Continental Lithosphere near Passive Margins, *Tectonophys.*, 483, 20-28, 2010.

Flowers, R.M., B.P. Wernicke, and K.A. Farley, Unroofing, incision, and uplift history of the southwestern Colorado Plateau from apatite (U-Th)/He thermochronometry, *Geol. Soc. Am. Bull.*, 120, 571–587, 2008.

Fukao, Y., M. Obayashi, H. Inoue, M. Nenabi, Subducting slabs stagnant in the mantle transition zone, *J. Geophys. Res*., 97, 4809-4822, 1992.

George, P.G., and R.K. Dokka, Major Late Cretaceous cooling events in the eastern Peninsular Ranges, California, and their implications for Cordilleran tectonics, *Geol. Soc. Am. Bull.* 106, 903-914, 1994.

Glatzmaier, G. A., Numerical simulations of mantle convection: Time-dependent, three-dimensional, compressible, spherical shell, *Geophys. Astrophys. Fluid Dyn.*, 43, 223–264, 1988.

Goes, S., and S. van der Lee, Thermal structure of the North American uppermost mantle inferred from seismic tomography, *J. Geophys. Res*., 107(B3), 2050, 2002.

Gorczyk, W., Gerya, T.V., Connolly, J.A.D., Yuen, D.A., Growth and mixing dynamics of mantle wedge plumes, *Geology*, 35, 587-590, 2007.

Grand S.P. and D.V. Helmberger, Upper mantle shear structure of North America, *Geophys. J. R. astr. Soc.*, 76, 399-438, 1984.

Grand, S. P., R. D. van der Hilst, and S. Widiyantoro, Global seismic tomography: a snapshot of convection in the earth, *GSA Today*, 7, 1-7, 1997.

Grand, S. P., Mantle shear-wave tomography and the fate of subducted slabs, *Philos. Trans. R. Soc. London, Ser. A*, 360, 2475–2491, 2002.

Gurnis, M., Continental flooding and mantle-lithosphere dynamics, *in Glacial Isostasy, Sea-Level, and Mantle Rheology (edited by R. Sabadini, K. Lambeck, and E. Boschi) Kluwer Academic Publishers, Dordrect*, 445-492, 1991.

Gurnis, M., Phanerozoic marine inundation of continents driven by dynamic topography above subducting slabs, *Nature, 364*, 589-593, 1993.

Gurnis, M., R. D. Müller, and L. Moresi, Dynamics of Cretaceous vertical motion of Australia and the Australian-Antarctic discordance, *Science, 279*, 1499-1504, 1998.

Gurnis, M., J. X. Mitrovica, J. Ritsema, and H.-J. van Heijst, Constraining mantle density structure using geological evidence of surface uplift rates: The case of the African Superplume, *Geochem. Geophys. Geosyst., 1(7)*, 1020, 2000.

Gurnis, M., et al., Global plate reconstructions with continuously closing plate, *to be submitted to this issue, Geochm., Geophys., Geosyst.*, in review.

Guscher, M-A, J.-L.Olivet, D. Aslanianb, J.-P. Eissen, R. Mauryd, The "lost Inca Plateau": cause of flat subduction beneath Peru? *Earth Planet. Sci. Lett.* 171, 335-341, 1999a.

Hager, B.H., Subducted slabs and the geoid: Constaintraints on mantle rheology and flow, *J. Geophys. Res. 89, B7*, 6003-6015, 1984.

Hager, B., Subducted slabs and the geoid: constraints on mantle rheology and flow, *J. Geophys. Res., 89*, B7, 6003-6015, 1984.

Hager, B., and R. Clayton, Constraints on the structure of mantle convection using seismic observations, flow models, and the geoid, in *Mantle Convection* (ed. by W. R. Peltier), Gordon and Breach, *New York*, 657–763, 1988.

Hansen, U., D. A. Yuen, S. E. Kroening and T. B. Larsen, Dynamical consequences of depth-dependent thermal expansivity and viscosity on mantle circulations and thermal structure, *Phys. Earth Planet. Inter*., 77, 205-223, 1993.

Haq, B. U. & Al-Qahtani, A. M. Phanerozoic cycles of sea-level change on the Arabian Platform. *GeoArabia* 10, 127-160, 2005.

Hebert, L.B. P. Antoshechkina, P. Asimow, and M. Gurnis, Emergence of a low-viscosity channel in subduction zones through the coupling of mantle flow and thermodynamics, *Earth Planet. Sci. Lett.*, 278, 243–256, 2009.

Henderson, L. J., R. G. Gordon, & D. C. Engebretson, Mesozoic aseismic ridges on the Farallon plate and southward migration of shallow subduction during the Laramide Orogeny, *Tectonics* 3, 121-132, 1984.

Hernlund, J.W., C. Thomas, and P.J. Tackley, A doubling of the post-perovskite phase boundary and structure of the Earth's lowermost mantle, *Nature*, 434, 882-886, 2005.

Hernlund, J.W., P.J. Tackley, and D.J. Stevenson, Buoyant melting instabilities beneath extending lithosphere: 1. Numerical models, *J. Geophys. Res.*, 113, B04405, 2008.

Hirose, K., Y. Fei, Y. Ma & H-K. Mao, The fate of subducted basaltic crust in the Earth's

lower mantle, *Nature* 397, 53-56, 1999.

Hoorn, C. Marine incursions and the influence of Andean tectonics on the Miocene depositional history of northwestern Amazonia: results of a palynostratigraphic study. *Palaeogeog., Palaeoclimat., Palaeoecol.* 105, 267-309, 1993.

Hoorn, C., Guerrero, J., Sarmiento, G. A. & Lorente, M. A. Andean tectonics as a cause for changing drainage patterns in Miocene northern South America. *Geology* 23, 237-240, 1995.

Hoorn, C. Miocene deposits in the Amazonian Foreland Basin (Technical comments). *Science* 273, 122, 1996.

Huntington, K.W., Wernicke, B.P., and Eiler, J.M., The influence of climate change and uplift on Colorado Plateau paleotemperatures from carbonate clumped isotope thermometry: *Tectonics*, 29, TC3005, 2010.

Humphreys, E., Hessler, E., Dueker, K., Farmer, C.L., Erslev, E., and Atwater, T., How Laramide-age hydration of North American lithosphere by the Farallon slab controlled subsequent activity in the western United States, *Inter. Geol. Rev.*, 45, 575–595, 2003.

Humphreys, E. D., and D. D. Coblentz, North American dynamics and western U.S. tectonics, *Rev. Geophys., 45*, RG3001, 2007.

Huang, J. and D. Zhao, High-resolution mantle tomography of China and surrounding regions, *J. Geophys. Res.*, 111, 2006.

Hughes, T. J. R., *The finite element method: Linear static and dynamic finite element analysis*, Dover publication, Mineola, N.Y., ISBN: 0-486-41181-8, 2000.

Ishii, M., and J. Tromp, Normal-mode and free-air gravity constraints on lateral variations in velocity and density of Earth's mantle, *Science, 285*, 1231-1236, 1999.

Ishii, M. and J. Tromp, Constraining large-scale mantle heterogeneity using mantle and inner-core sensitive normal modes, *Phys. Earth Planet. Inter.* 146, 113 (2004).

Ismail-Zadeh, A.T., C.J. Talbot, Y.A. Volozh, Dynamic restoration of profiles across diapiric salt structures: numerical approach and its applications. *Tectonophys., 337*, 21–36, 2001.

Ismail-Zadeh, A., G. Schubert, I. Tsepelev and A. Korotkii, Inverse problem of thermal convection: numerical approach and application to mantle plume restoration, *Phys. Earth Planet. Inter., 145*, 99-114, 2004.

Ito, G. and M. D. Behn, Magmatic and tectonic extension at mid-ocean ridges: 2. Origin of axial morphology, *Geochem. Geophys. Geosys.* 9, Q08O10, 2008.

Ji, S. and Zhao P., Layered rheological structure of subducting oceanic lithosphere, *Earth Planet. Sci. Lett.*, 124, 75–94, 1994.

Jordan, T. H., The continental tectosphere, *Rev. Geophys. Space Phys.*, 13, 1-12, 1975.

Karato, S. and B. B. Karki, Origin of lateral variation of seismic wave velocities and density in the deep mantle, *J. Geophys. Res.*, 106, B10, 21,771, 2001.

Karlstrom, K.E., and C.G. Daniel, Restoration of Laramide right-lateral strike slip in northern New Mexico by using Proterozoic piercing points: Tectonic implications from the Proterozoic to the Cenozoic, *Geology*, 21, 1139-1142, 1993.

Karlstrom, K.E., Crow, R., Crossey, L.J., Coblentz, D., and Van Wijk, J.W., Model for tectonically driven incision of the younger than 6 Ma Grand Canyon, *Geology*, 36, 835–838, 2008.

Katz, R. F., M. Spiegelman, and B. Holtzman, The dynamics of melt and shear localization in partially molten aggregates, *Nature*, 2006.

Katz, R. F., Magma dynamics with the Enthalpy Method: Benchmark Solutions and Magmatic Focusing at Mid-ocean Ridges. *J. Petro.*, 2008.

Kincaid , C. and P. S. Hall, Role of back arc spreading in circulation and melting at subduction zones, *J. Geophys. Res*., 108, 2240, 2003.

Lakshtanov, D. L. *et al*., The post-stishovite phase transition in hydrous alumina-bearing SiO2 in the lower mantle of the earth, *Proc. Nat. Acad. Sci.* 104, 13588-13590, 2007.

Leng, W. and S.J. Zhong, Controls on plume heat flux and plume excess temperature, *J. Geophys. Res.*, 113, B04408, 2008.

Li, X.D. and B. Romanowicz, Global mantle shear velocity model developed using nonlinear asymptotic coupling theory, *J. Geophys. Res*., 101. 22,245-22,273, 1996.

Li, C., R. D. van der Hilst, E. R. Engdahl & S. Burdick, A new global model for P wave speed variations in Earth's mantle, *Geochem. Geophys. Geosys.* 9, Q05018, 2008.

Lithgow-Bertelloni, C., and M. Gurnis, Cenozoic subsidence and uplift of continents from time-varying dynamic topography, *Geology, 25*, 735-738, 1997.

Lithgow-Bertelloni, C. and M. A. Richards, The dynamics of Cenozoic and Mesozoic plate motions, *Rev. Geophys., 36*, 27-78, 1998.

Lithgow-Bertelloni, C. and P.G. Silver, Dynamic topography, plate driving forces and the African Superswell, *Nature*, 395, 269-272, 1998.

Liu, S., D. Nummedal, P-G. Yin, and H-J. Luo, Linkage of Sevier thrusting episodes and Late Cretaceous foreland basin megasequences across southern Wyoming (USA), *Basin Res., 17,* 487-506, 2005.

Liu. L., and M. Gurnis, Simultaneous inversion of mantle properties and initial conditions using an adjoint of mantle convection, *J. Geophys. Res.* 113, B08405, 2008.

Liu, L., S. Spasojević and M. Gurnis, Reconstructing Farallon plate subduction beneath North America back to the Late Cretaceous, *Science, 322*, 934-938, 2008.

Liu, L., M. Gurnis, M. Seton, J. Saleeby, R.D. Müller & J. Jackson, The role of oceanic plateau subduction in the Laramide Orogeny, *Nature Geoscience*, 3, 353-357, 2010.

Liu, L. and M. Gurnis, Dynamic subsidence and uplift of the Colorado Plateau, *Geology*, 38, 663-666, 2010.

Liu, L. and M. Gurnis, Adjoint method and its application in mantle convection (in Chinese with English abstract), *Earth Sci. Front.* (INVITED), in press, 2010.

Liu, S., and D. Nummedal, Late Cretaceous subsidence in Wyoming: Quantifying the dynamic component, *Geology, 32,* 397-400, 2004.

Liu, S., D. Nummedal and L. Liu, Tracking the Farallon plate migration through the Late Cretaceous Western U.S. Interior Basins, *Geology*, in review.

Livaccari, R. F., R. F., Burke, K, & Sengor, A. M. C., Was the Laramide Orogeny related to subduction of an oceanic plateau? *Nature*, 289, 276-278, 1981.

Manea, V.and M. Gurnis, Subduction zone evolution and low viscosity wedges and channels, *Earth Planet. Sci. Lett. 264*, 22-45, 2007.

Marshall, L. G. & Lundberg, J. G. Miocene deposits in the Amazonian Foreland Basin (Technical comments). *Science* 273, 123, 1996.

Masters, G., G. Laske, H. Bolton, and A. Dziewonski, The relative behavior of shear velocity, bulk sound speed, and compressional velocity in the mantle: Implications for chemical and thermal structure, in *Earth's Deep Interior* (Karato, S. *et al*., editor), AGU, Washington, DC, 63-87, 2000.

McKenzie, D. P. and J. Morgan, The evolution of triple junctions, *Nature* 224, 125-133, 1969.

McMillan, M.E., P.L Heller, and S.L. Wing, History and causes of post-Laramide relief in the Rocky Mountain orogenic plateau, *GSA Bulletin, 108*, 393–405, 2006.

McNamara, A. K., and S.J. Zhong, Thermochemical structures beneath Africa and the Pacific Ocean, *Nature*, 437, 1136-1139, 2005

McQuarrie, N., and Chase, C.G., Raising the Colorado Plateau: *Geology*, 28, 91–94, 2000.

Milne, G. A., J. X. Mitrovica, H-G Scherneck, J. L. Davis, J. M. Johansson, H. Koivula, and M. Vermeer, Continuous GPS measurements of postglacial adjustment in Fennoscandia: 2. Modeling results, *J. Geophys. Res.* 109, B02412, 2004.

Miller, K.G., M. A. Kominz, J.V. Browning, J. D. Wright, G.S. Mountain, M.E. Katz, P.J. Sugarman, B.S. Cramer, N. Christie-Blick, and S.F. Pekar, The Phanerozoic Record of Global Sea-Level Change, *Science*, 310, 1293-1298, 2005.

Mitrovica, J. and A. Forte, Radial profile of mantle viscosity: Results from the joint inversion of convection and glacial rebound observables, *J. Geophys. Res.*, 102, 2751-2769, 1997.

Mitrovica, J. X., Beaumont, C. & Jarvis, G. T. Tilting of continental interiors by the dynamical effects of subduction. *Tectonics* 8, 1079–1094, 1989.

Mitrovica, J. X., and A. M. Forte, A new inference of mantle viscosity based upon joint inversion of convection and glacial isostatic adjustment data, *Earth Planet. Sci. Lett., 225*, 177– 189, 2004.

Molnar, P., & Tanya Atwater, Relative motion of hot spots in the mantle, *Nature* 246, 288-291, 1973.

Montelli, R., G. Nulet, F. Dahlen, G. Masters, E.R. Engdahl S-H. Hung, Finite-Frequency Tomography Reveals a Variety of Plumes in the Mantle, *Science*, 303, 338-343, 2004.

Moucha, R., A.M. Forte, J.X. Mitrovica, D.B. Rowley, S. Quéré, N.A. Simmons, and S.P. Grand, Dynamic Topography and Long-Term Sea-Level Variations: There Is No Such Thing as a Stable Continental Platform, *Earth Planet. Sci. Lett., 271*, 101-108, 2008.

Moucha, R., Forte, A.M., Rowley, D.B., Mitrovica, J.X., Simmons, N.A., and Grand, S.P., Deep mantle forces and the uplift of the Colorado Plateau: Geophysical Research Letters, 36, L19310, 2009.

Müller, R.D., M.Sdrolias, C. Gaina and W.R. Roest, Age, spreading rates and spreading asymmetry of the world's ocean crust, *Geochem., Geophys., Geosys.*, 9, Q04006, 2008a.

Muller, R.D., M. Sdrolias, C. Gaina, B. Steinberger, and C. Heine, Long-term sea-level fluctuations driven by ocean basin dynamics, *Science*, 319, 1357-1362, 2008b.

Nadin, E.S. and J. B. Saleeby, in *Ophiolites, Arcs, and Batholiths: Geol. Soc. Am. Spec. Pap.* (ed. Wright, J.E. and Shervais, J.W.), 438, 429-453, 2008.

Nakanishi, M., W. W. Sager & A. Klaus, Magnetic lineations within Shatsky Rise, northwest Pacific Ocean: Implications for hot spot-triple junction interaction and oceanic plateau formation *J. Geophy. Res.* 104, B4, 7539-7556, 1999.

Ni, S., E. Tan, M. Gurnis, and D. Helmberger, Sharp sides to the African superplume, *Science*, 296, 1850-1852, 2002.

Nolet, G., R. Allen, D. Zhao, Mantle plume tomography, *Chem. Geol.*, 241, 248-263, 2007.

O'Neill, C., R.D. Müller & B. Steinberger, On the uncertainties in hotspot reconstructions, and the significance of moving hotspot reference frames, *Geochem., Geophys., Geosys.* 6, 35, 2005.

Pang, M. and D. Nummedal, Flexural subsidence and basement tectonics of the Cretaceous Western Interior basin, United States, *Geology* 23, 173, 1995.

Parsons, T., Thompson, G.A., and Sleep, N.H., Mantle plume influence on Neogene uplift and extension of the U.S. western Cordillera? *Geology*, 22, 83–86,1994.

Pindell, J., L. Kennan, K. P. Stanek, W. V. Maresch, and G. Draper, Foundations of Gulf of Mexico and Caribbean evolution: Eight controversies resolved, *Geol. Acta*, 41, 303–341, 2006.

Ren, Y., E. Stutzmann, R.D. Van der Hilst, and J. Besse, Understanding seismic heterogeneities in the lower mantle beneath the Americas from seismic tomography and plate tectonic history, *J. Geophys. Res., 112*, B01302, 2007.

Rey, P.F. and R. D. Muller, Fragmentation of active continental plate margins owing to the buoyancy of the mantle wedge, *Nature Geoscience*, 3, 257-261, 2010.

Ringwood, A.E., and D.H. Green, An experimental investigation of the gabbro-eclogite transformation and some geophysical implications, *Tectonophys.* 3, 383-427, 1966.

Ritsema, J., H. J. van Heijst, and J. H. Woodhouse, Global transition zone tomography, *J. Geophys. Res.*, 109, 10.1029/2003JB002610, 2004.

Ritsema, J., A. K. McNamara, and A. Bull, Tomographic filtering of geodynamic models: implications for model interpretation and large-scale mantle structure, *J. Geophys. Res.*, 112, 10.1029/2006JB004566, 2007.

Richard, M. and B. Hager, Geoid anomalies in a dynamic earth, *J. Geophys. Res., 89*, 5987−6002, 1984.

Roddaz, M., Baby, P., Brusset, S., Hermoza, W. & Darrozes, J.M. Forebulge dynamics and environmental control in Western Amazonia: The case study of the Arch of Iquitos (Peru). *Tectonophys.* 399, 87-108, 2005.

Roddaz, M., Viers, J., Brusset, S., Baby, P. & Hérail, G. Sediment provenances and drainage evolution of the Neogene Amazonian foreland basin. *Earth Planet. Sci. Lett.* 239, 57-78, 2005.

Roth, J.B., M.J. Fouch, D.E. James, R.W. Carlson, Three-dimensional seismic velocity structure of the northwestern United States, *Geophys. Res. Lett.*, 35, L15304, 2008.

Rowlinson, N., and M. Sambridge, Seismic traveltime tomography of the crust and lithosphere, *Advan. Geophys.*, 46, 81-197, 2003.

Roy, M., Kelley, S., Pazzaglia, F., Cather, S., and House, M., Middle Tertiary buoyancy modification and its relationship to rock exhumation, cooling, and subsequent extension at the eastern margin of the Colorado Plateau, *Geology*, 32, 925–928, 2004.

Roy, M., Jordan, T. H. and Pederson, J., Colorado Plateau magmatism and uplift by warming of heterogeneous lithosphere, *Nature*, 459, 978-982, 2009.

Sager, W. W., D. W. HandschumacheTr,. W. C. Hilde, & D. R. Bracey, Tectonic evolution of the northern Pacific plate and Pacific-Farallon-Izanagi triple junction in the Late Jurassic and Early Cretaceous (M21-M10), *Tectonophys.* 155, 345-364, 1988.

Saleeby, J., Segmentation of the Laramide slab-evidence from the southern Sierra Nevada region: *Geol. Soc. Am Bull*, 115, 655-668, 2003.

Saleeby, J., Farley, K.A., Kistler, R.W., and Fleck, R.J., Thermal evolution and exhumation of deep-level batholithic exposures, southernmost Sierra Nevada, California, *in* Cloos, M., et al., eds., Convergent margin terranes and associated regions: A tribute to W.G. Ernst: Geological Society of America special paper 419, 39–66, 2007.

Sahagian, D., Proussevitch, A., and Carlson, W., Timing of Colorado Plateau uplift: Initial constraints from vesicular basalt-derived paleo elevations, *Geology*, 30, 807–810, 2002.

Sandiford, M., The tilting continent: a new constraint on the dynamic topographic field from Australia, *Earth Planet. Sci. Lett.*, 261, 152-163, 2007.

Shephard, G.E., R.D. Müller, L. Liu and M. Gurnis, Miocene Amazon River drainage reversal caused by plate-mantle dynamics, *Nature Geoscience*, in review.

Sidorin, I., M. Gurnis, and D.V. Helmberger, Dynamics of a phase change at the base of the mantle consistent with seismological observations, *J. Geophys. Res.*, 104, 15005-15023, 1999.

Sigloch, K., N. McQuarrie, and G. Nolet, Two-stage subduction history under North America inferred from multiple-frequency tomography, *Nature Geoscience, 1,* 458 – 462, 2008.

Sirkes, Z. and E. Tziperman, Finite difference of adjoint or adjoint of finite difference? *Am. Meteorol. Soc.*, 125, 3373-3378, 1997.

Smith, B., Jordan, M., Steinberger, B., Puskas, C., Farrell, J., Waite, G., Husen, S., O'Connell, R.J. & Klingele E., Geodynamics of the Yellowstone hotspot and mantle plume: Seismic and GPS imaging, kinematics and mantle flow, *J. Volcanol. Geoth. Res.*, 128, 26-56, 2009;

Spasojević, S., L. Liu, M. Gurnis, and R. D. Muller, The case for dynamic subsidence of the United States east coast since the Eocene, *Geophys. Res. Lett., 35,* L08305, 2008.

Spasojević, S., Liu, L., and Gurnis, M., Adjoint models of mantle convection with seismic, plate motion, and stratigraphic constraints: North America since the Late Cretaceous, *Geochem. Geophys. Geosys.*, 10, Q05W02, 2009.

Stadler, G., M. Gurnis, C. Burstedde, L.C. Wilcox, L. Alisic, O. Ghattas, The Dynamics of Plate Tectonics and Mantle Flow: From Local to Global Scales, *Science*, in review.

Stegman, D.R., R. Farrington, F.A. Capitanio, and W.P. Schellart. A regime diagram for subduction styles from 3-D numerical models of free subduction, *Tectonophys.*, 483, 29-45, 2010.

Steinberger, B. and R. O'Connell, Effects of mantle flow on hotspot motion, in *The History of Dynamics of Global Plate Motion,* Geophysical Monograph, *121,* 377-398, 2000.

Su, W., Woodward, R. L., Dziewonski, A. M., Degree 12 model of shear velocity heterogeneity in the mantle, *J. Geophys. Res.*, 99, 6945-6980, 1994.

Sun, J., D. W. Flicker, D. K. Lilly, Recovery of 3D wind and temperature fields from simulate single-Doppler radar data, *J. Atmos. Sci.*, 48, No.6, 1991.

Sun, D., D. Helmberger, S. Ni & D. Bower, Direct measures of lateral velocity variation in the deep Earth, *J. Geophy. Res.* 114, B05303, 2009.

Sun D. and D. Helmberger, Upper Mantle Structures Beneath USArray Derived from Waveform Complexity, submitted.

Tackley, P. J., Modellng compressible mantle convection with large viscosity contrasts in a three-dimensional spherical shell using the yin-yang grid, *Phys. Earth Planet. Inter*., 171 (1-4), 7-18, 2008.

Talagrand, O. and P. Courtier, Variational assimilation of meteorological observation with the adjoint vorticity equation, *Q. J. R. Meteorol. Soc.*, 113, 1211-1328, 1987.

Tan, E., E. Choi, P. Thoutireddy, M. Gurnis, and M. Aivazis, GeoFramework: Coupling multiple models of mantle convection within a computational framework, *Geochem., Geophys., Geosys.*, 7, Q06001, 2006.

Tan, E., *et al.*, CitcomS Users Guide Version 3.0.1, California Institute of Technology (http://www.geodynamics.org/cig/software/packages/mc/citcoms/)

Tarantola, A., Inverse problem theory and methods for model parameter estimation, ISBN 0-89871-572-5, 2005.

Tarduno, J. A., M. McWilliams, M. G. Debiche, W. V. Sliter & M. C. Blake Jr, Franciscan Complex Calera limestones: accreted remnants of Farallon Plate oceanic plateaus, *Nature* 317, 345-347, 1985.

Tarduno, J.A., R.A. Duncan, D.W. Scholl, R.D. Cottrell, B. Steinberger, T. Thordarson, B.C. Kerr, C.R. Neal, F.A. Frey, M. Torii & C. Carvallo, The Emperor Seamounts: Southward motion of the Hawaiian Hotspot plume in Earth's mantle, *Science* 301, 1064-1069, 2003.

Tarduno, J.A., H.-P. Bunge, N. Sleep & U. Hansen, The bent Hawaiian-Emperor hotspot track: Inheriting the mantle wind, *Science* 324, 50-53, 2009.

Tetzlaff, M., H. Schmeling, The influence of olivine metastability on deep subduction of oceanic lithosphere. *Phys. Earth Planet. Inter.* 120:29–38, 2000.

Tian, Y., K. Sigloch, G. Nolet, Multiple-frequency SH-wave tomography of the western US upper mantle, *Geophys. J. Int.*, 178 (3), 1384-1402, 2009.

Torsvik, T.H., Smethurst, M.A., Burke, K. & Steinberger, B., Long term stability in Deep Mantle structure: Evidence from the ca. 300 Ma Skagerrak-Centered Large Igneous Province (the SCLIP). *Earth Planet. Sci. Lett.* 267, 444-452, 2008.

Trampert, J., F. Deschamps, J. Resovsky, and D. Yuen, Probabilistic Tomography Maps Chemical Heterogeneities Throughout the Lower Mantle, *Science*, 306, 853-856, 2004.

Trampert, J., F. Deschamps, J. Resovsky, D. Yuen, *Science* 306, 853, 2004.

Van der Hilst, R.D, S. Widiyantoro, and E.R. Engdahl, Evidence of deep mantle circulation from global tomography, *Nature*, 386, 578-584, 1997.

Van der Meer, D.G., W. Spakman, D. J. J. van Hinsbergen, M. L. Amaru and T. H. Torsvik, Towards absolute plate motions constrained by lower-mantle slab remnants, *Nature Geoscience*, 3, 36-40, 2010.

Walcott, R., Structure of the earth from glacio-isostatic rebound, *Annu. Rev. Earth. Planet. Sci.*. 1, 15– 37, 1973.

Wessel, P., Y. Harada & L. W. Kroenke, Toward a self-consistent, high-resolution absolute plate motion model for the Pacific, *Geochem. Geophys. Geosys.* 7, Q03L12, 2006.

Wessel, P. & L. W. Kroenke, Pacific absolute plate motion since 145 Ma: An assessment of the fixed hot spot hypothesis, *J. Geophys. Res.* 113, B06101, 2008.

West, J.D., M.J. Fouch, J.B. Roth, L.T. Elkins-Tanton, Vertical mantle flow associated with a lithospheric drip beneath the Great Basin, *Nature Geoscience*, 2, 439-444, 2009.

Whittaker, J. M., R. D. Muller, G. Leitchenkov, H. Stagg, M. Sdrolias, C. Gaina, and A. Goncharov, Major Australian-Antarctic Plate Reorganization at Hawaiian-Emperor Bend Time, *Science*, 318, 83, 2007.

Wolfe, J.A., Forest, C.E., and Molnar, P., Paleobotanical evidence of Eocene and Oligocene paleoaltitudes in midlatitude western North America, *Geol. Soc. Am. Bull.*, 110, 664–678, 1998.

Zhao, D., X. Xu, D. A. Wiens, L. Dorman, J. Hildebrand, and W. Webb, Depth extent of the Lau back-arc spreading center and its relation to subduction processes, *Science*, 278, 254-257, 1997.

Zhao, D., Global tomographic images of mantle plumes and subducting slabs: insight into deep Earth dynamics, *Phys. Earth Planet. Inter.*, 146, 3-34, 2004.

Zhang, N., S.J. Zhong, W. Leng, and Z.X. Li, A model for the evolution of the Earth's mantle structure since the Early Paleozoic, *J. Geophys. Res.*, in press, 2010.

Zhong, S. and M. Gurnis, Mantle convection with plates and mobile, faulted plate margins, *Science* 267, 838, 1995.

Zhong, S., and Gurnis, M., Interaction of weak faults and non-Newtonian rheology produces plate tectonics in a 3D model of mantle flow, *Nature* 383, 245-247, 1996.

Zhong, S., M. T. Zuber, L. Moresi, and M. Gurnis, The role of temperature-dependent viscosity and surface plates in spherical shell models of mantle convection, *J. Geophys. Res.*, 105, 11,063-11,082, 2000.

Zhong, S., A.K. McNamara, E. Tan, L. Moresi, and M. Gurnis, A benchmark study on mantle convection in a 3-D spherical shell using CitcomS, *Geochem. Geophys. Geosys.* 9, Q10017, 2008.

Zhu, G., Gerya, T.V., Yuen, D.A., Honda, S., Yoshida, T., Connolly, J.A.D., 3-D Dynamics of hydrous thermalchemical plumes in oceanic subduction zones. *Geochem., Geophys., Geosyst.*, 10, Q11006, 2009.